2006-02-17

A Plastic-Based Thick-Film Li-Ion Microbattery for Autonomous Microsensors

Qian Lin
Brigham Young University - Provo

A PLASTIC-BASED THICK-FILM LI-ION MICROBATTERY FOR AUTONOMOUS MICROSENSORS

By

Qian Lin

A dissertation submitted to the faculty of

Brigham Young University

In partial fulfillment of the requirements for the degree of

Doctor of Philosophy

Department of Chemical Engineering

Brigham Young University

April 2006

BRIGHAM YOUNG UNIVERSITY

GRADUATE COMMITTEE APPROVAL

of a dissertation submitted by

Qian Lin

This dissertation has been read by each member of the following graduate committee and by a majority vote has been found satisfactory.

_____	_____
Date	John N. Harb, Chair
_____	_____
Date	William G. Pitt
_____	_____
Date	Thomas H. Fletcher
_____	_____
Date	Ronald E. Terry
_____	_____
Date	Richard L. Rowley

BRIGHAM YOUNG UNIVERSITY

As chair of the candidate's graduate committee, I have read the dissertation of Qian Lin is in its final form and have found that (1) its format, citations, and bibliographical style are consistent and acceptable and fulfill university requirements; (2) its illustrative materials including figures, tables, and charts are in place; and (3) the final manuscript is satisfactory to the graduate committee and is ready for submission to the university library.

_____ _____

Date

John N. Harb
Chair, Graduate Committee

Accepted for the Department

_____

William G. Pitt
Graduate Coordinator

Accepted for the College

_____

Alan R. Parkinson
Dean, Ira A. Fulton College of Engineering
and Technology

ABSTRACT

A PLASTIC-BASED THICK-FILM LI-ION MICROBATTERY

FOR AUTONOMOUS MICROSENSORS

Qian Lin

Department of Chemical Engineering

Doctor of Philosophy

This dissertation describes the development of a high-power, plastic-based, thick-film lithium-ion microbattery for use in a hybrid micropower system for autonomous microsensors. A composite porous electrode structure and a liquid state electrolyte were implemented in the microbatteries to achieve the high power capability and energy density. The use of single-walled carbon nanotubes (SWNTs) was found to significantly reduce the measured resistance of the cathodes that use $LiAl_{0.14}Mn_{1.86}O_4$ as active materials, increase active material accessibility, and improve the cycling and power performance without the need of compression. Optimized uncompressed macro cathodes were capable of delivering power densities greater than 50 mW/cm^2, adequate to meet the peak power needs of the targeted microsystems. The anodes used mesocarbon microbeads (MCMB) with multi-walled carbon nanotubes (MWNTs) and had significantly better power performance than the cathodes.

The thick-film microbattery was successfully fabricated using techniques compatible with microelectronic fabrication processes. A Cyclic Olefin Copolymer (COC)-film was used as both the substrate and primary sealing materials, and patterned metal foils were used as the current collectors. A liquid-state electrolyte and Celgard separator films were used in the microbatteries. These microbatteries had electrode areas of c.a. 2 mm x 2 mm, and nominal capacities of 0.025-0.04 mAh/cell (0.63-1.0 mAh/cm^2, corresponding to an energy density of ~6.3-10.1 J/cm^2). These COC-based batteries were able to deliver constant currents up to 20 mA/cm^2 (100% depth of discharge, corresponding to a power density of 56 mW/cm^2 at 2.8 V) and pulse currents up to 40 mA/cm^2 (corresponding to a power density of 110 mW/cm^2). The high power capability, small size, and high energy density of these batteries should make them suitable for the hybrid micropower systems; and the flexible plastic substrate is also likely to afford some unique integration possibilities for autonomous microsystems.

The mechanism by which the SWNTs improved the rate performance of composite cathodes was studied both experimentally and theoretically. It was concluded that the use of SWNT improved cathode performance by improving the electronic contacts to active material particles, which consequently improved the accessibility of these particles and improved the rate capability of the composite cathodes.

ACKNOWLEDGEMENTS

I would like to gratefully acknowledge the support and encouragement I have received from my advisor Professor John N. Harb. For the years of my stay at Brigham Young University, he has been directing my research, as well as being a friend. I would also like to acknowledge the support from my wife Xiaotian. Without her support, completion of this work would not be possible. I would like to thank Jamie Holladay, Paul Humble, Min Tan, Jikun Liu, and many others, for their advice and help in this work. I would also gratefully acknowledge the financial support for this work that has from the National Science Foundation (XYZ on a Chip, DMI-9980835) and NASA (NCC-1-02005).

TABLE OF CONTENTS

LIST OF FIGURES

LIST OF TABLES

LIST OF SYMBOLS AND NOMENCLATURE

CB	carbon black;
CB-cathode	a composite cathode that uses CB as conductive additives;
Celgard	a trade name for porous polypropylene separator films;
CNT	carbon nanotubes;
COC	Cyclic Olefin Copolymer;
C rate, C-rate	1 C rate corresponds to a current at which a fully charged cell will be completely discharged in 1 hour;
DOD	depth of discharge. A 100% DOD discharge refers to a complete discharge;
Duty cycle	a term to describe the unit of operation of microsensors, which is consisted of a low power stand-by and a high power active operation periods;
EPD	Electrophoretic deposition;
IC	integrated circuit;
ICL	irreversible capacity loss;
Intercalation	an incorporation process of Li^+ into the crystal lattice of electrode materials;
LIPON	lithium phosphorus oxynitride, a solid state electrolyte for thin-film batteries;
Lithiation	intercalation of lithium ions;
MCMB	mesocarbon microbead, a type of anode materials in Li-ion batteries;
MWNT	multi-walled carbon nanotubes;
OCP	open circuit potential (V);
PP	polypropylene;
PR	photoresist;
PSD	particle size distribution;
PVDF	polyvinylidenefluoride, a polymer binder used in this study;
SEI	solid electrolyte interface, a passivation film (ionic conducting but electrically insulating) on the electrode surface to stabilize the intercalation system;
SEM	scanning electron microscope;
SOC	state of charge, ratio of concentration of intercalated Li^+ to the equilibrium Li^+ concentration in solid phase;
SPE	solid polymer electrolyte;
SWCNT, SWNT	single walled carbon nanotubes;
SWNT-cathode	a composite cathode that uses SWNT as conductive fillers;
Taper-charge	a technique used to charge a cell to its full capacity, in which the cell voltage is held constant and charge current is gradually decreased;
Via	a hole structure used in microelectronics to make connection through a layer;

A	electrode area;
b	the Bruggeman exponent;
C	concentration of the salt (subscription t refer to maximum concentration, s refer to solid phase, B and E refer to the bulk and the electrode surface, respectively);

D_{eff}	diffusion coefficient;
F	the Faraday's constant;
i	current density;
j_n	pore wall flux of Li^+;
k	reaction rate constant;
R	the gas constant;
R_{film}	film resistance, a parameter used in the dualfoil model;
T	temperature;
U	open circuit potential;
y	state of charge;
α_a, α_c	transfer coefficients in the Bulter-Volmer equation;
δ	boundary layer thickness;
ε	porosity, which is also the volume fraction of the electrolyte in this study;
ε_s	volume fraction of the active material;
η	surface overpotential;
κ_{eff}	ionic conductivity of the salt in the electrolyte;
σ_s	electrical conductivity of the solid phase.

CHAPTER 1: INTRODUCTION

High-volume, low-unit-cost fabrication techniques are among the key factors that have led to the success of microelectronics for the past 30 years. These techniques and other microfabrication techniques have been used to build microscopic sensors in recent years. It is of great interest to combine microsensors and microelectronics as microscopic systems that can sense and/or interact with the physical world.

Of particular interest to this study are autonomous microsensors (also called wireless or remote microsensors), which do not have physical connections for either power or communication. These sensors rely on on-board power supplies for operation throughout their lifetime, and send and/or receive information via wireless connections. One attractive potential application of autonomous microsensors is a sensing array formed by distributing a large number of sensor units onto a field of interest (e.g. a battle field) where wiring is impractical or impossible.

While microsensors have existed for over 10 years, microscopic power supplies for these sensors are still being developed. Such developments have direct impact on the size and performance of the microsensing systems. As a part of a larger project targeting a micro power solution, an objective of this study was to develop a microbattery to provide energy and power for autonomous microsensors and other similar applications.

1.1 AUTONOMOUS MICROSENSORS

One example of an autonomous microsensor is "Smart Dust" (Fig. 1.1), being developed by K. Pister and coworkers (Warneke and Pister 2002, Zhou et al. 2003). These remote microsensors are targeted to be an autonomous sensing and communication platform on a millimeter-scale, intended for a massively distributed sensor network. Each smart dust module is designed to contain sensors, a power supply, computation circuits and active elements for bi-directional wireless communication. Presently, a smart dust module occupies a volume of 16 mm^3 and is expected to shrink down to 6.6 mm^3 (Warneke and Pister 2002). Note that only part of the power supply, a solar cell array, has been implemented on current modules. Such a power supply lacks the capability to provide the required high power, as will be discussed shortly.

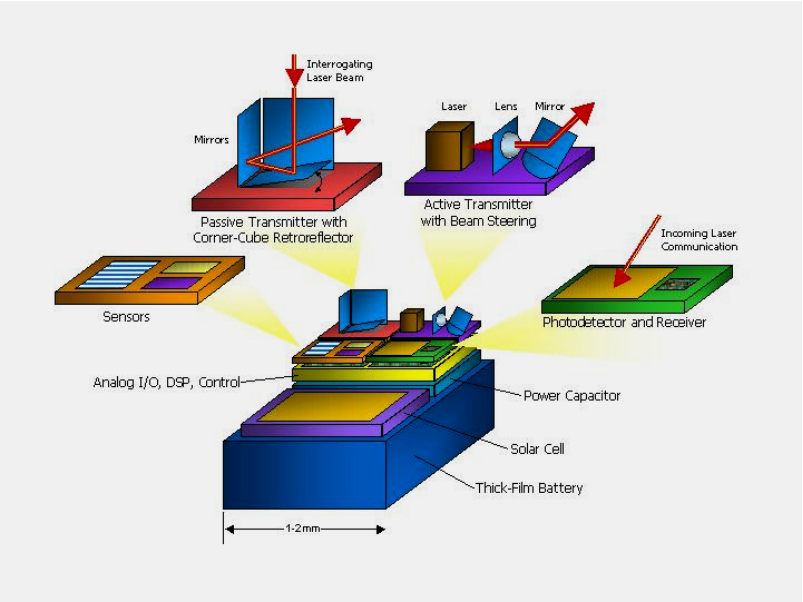

Figure 1.1 A conceptual diagram of a smart dust (Warneke and Pister 2002)

To ensure the full functionality of the miniature sensor devices, the power supply not only needs to provide sufficient energy, but also needs to deliver the required power. Obviously the size of the power supply needs to be smaller than or comparable to that of the microsensor in

order to take full advantage of the small sensor. The size of the power supply can be reduced by reducing the energy and power requirements of the device. Power management strategies and circuits have also been implemented to enable more efficient use of the available power (Wise 2000).

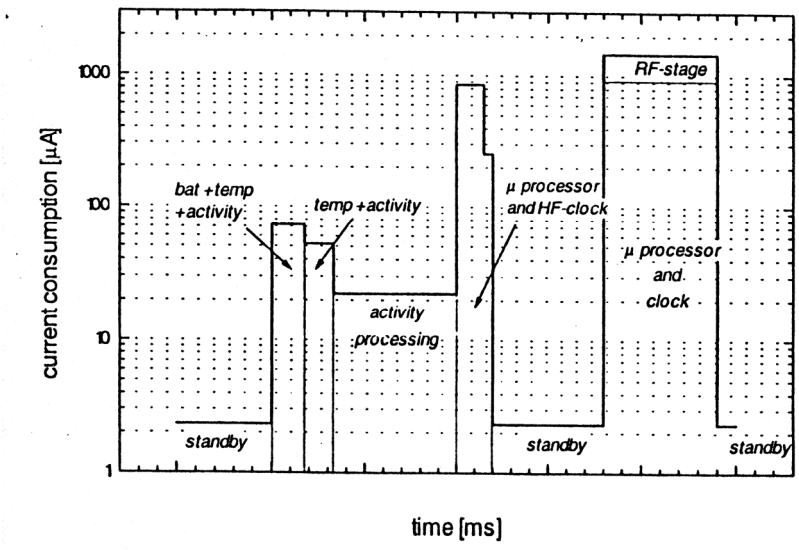

Figure 1.2 A current profile of typical microsensors (Puers and Routers 1997)

It should be noted that the power consumption rate of most autonomous microsensors varies significantly during operation, as illustrated in Puers and Routers (1997, Fig. 1.2). The duty cycle of the microsensor consists of a long low power stand-by period (a few µW) with intermittent short high power bursts (up to 6 mW) when active operations (e.g. data collecting, processing and/or transmitting) are performed. For a duty cycle that has a peak power of 5 mW lasting 10 ms, and a standby time of longer than 100 seconds at a power of 10 µW, the average power is essentially equivalent to the standby power. This estimation should be valid for a wide variety of sensor systems (Harb et al., 2002). Based on this average power requirement, a device needs about 6 J to operate for one week. With a desirable area of ~0.1 cm^2 (Harb et al. 2002), the

power supply needs to have a power capability of about 50 mW/cm^2 and an energy density of 60 J/cm^2 to meet the peak power and energy requirements of a microsensing system.

1.2 HYBRID MICROPOWER SUPPLIES

Two power options have been proposed for microsensors, energy conversion devices and energy storage devices. Both options have limitations in microsystems (Harb et al. 2002). Examples of energy conversion devices include solar cells (Warneke and Pister 2002), piezoelectric generators (Meninger, et al. 2001) and nuclear generators (Lal and Blanchard 2004). These devices have excellent energy densities but lack in power capabilities. Therefore, if an energy conversion device were used alone, it would need to be greatly oversized to meet the power requirements of the system. For example, Harb et al. (2002) showed that the average power and energy requirements can be easily met by a solar cell with an area less than 1 mm^2; however, an area of about 4.3 cm^2 is required to provide the peak power.

On the other hand, the size of a power system consisting of an energy storage device (i.e. a battery) alone is most likely limited by the energy requirement. Assuming an energy density of 2.5 J/cm^2 for microfabricated batteries (Harb et al. 2002), the area of the battery needs to be 2.4 cm^2 to supply the required energy (6 J as illustrated above) for an operational life of a week. The peak power requirement can be easily met with a battery of this area, as power densities of 30 mW/cm^2 (Neudecker et al. 2000) and 140 mW/cm^2 (Humble and Harb 2003) have been demonstrated.

Hybrid power schemes (e. g. Koeneman et al. 1997, Harb et al. 2002) appear to have the greatest promise of fulfilling the energy and power requirements for microsensors with a minimal size. Hybrid power supplies combine two or more power supplies, typically one being an energy conversion device and the other being an energy storage device. For example, the

hybrid micropower system proposed by Harb et al. (2002) consisted of solar cells and rechargeable microbatteries (Fig. 1.3). The solar cells were sized to meet the average power requirement, and the microbatteries were sized to provide the peak power and reserve capacity for the periods when energy scavenging is not available. As energy can be continually harvested from the environment, the life of the hybrid system is virtually limited by the cycle life of the battery (Harb et al. 2002). The size for that system was about 0.36 cm^2 (the maximum depth of discharge of the batteries was limited to 50 %, Harb et al. 2002), limited by the reserve capacity of the battery. Such an area is much smaller than that of a power supply with either solar cells or batteries alone.

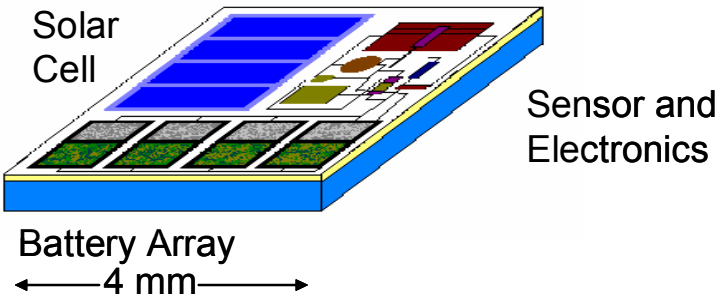

Figure 1.3 A microsensor with integrated hybrid power system (Humble et al. 2001)

1.3 DESIRABLE MICROBATTERY CHARACTERISTICS

As one key component in a hybrid micropower system, the battery will provide peak power and reserve energy for microsensors. It is obvious that the size of the microbattery should be comparable with that of other components in the system. Specifically, the desirable size of the battery is about 0.1 cm^2 in area and less than 1 mm in thickness. It is desirable to use microfabrication techniques to build these miniature batteries. Conventional techniques, such as those used for coin or button cells, are impractical for making batteries in the sub-millimeter

scale, as the energy density of button cells decreases exponentially with decreasing volume (Ruetschi 1980). Coin cells as small as 4.8 mm in diameter and 1.4 mm in height (ML414S coin cell, Panasonic) are available commercially.

Providing the peak power to the microsystem is the primary function of the battery; therefore, the microbattery should meet the power requirements of the system. For a cell area of about 0.1 cm^2, a battery with a power capability of ~50 mW/cm^2 is desirable for the micropower system. This was set as a primary target characteristic for battery development in this study.

It is desirable that the battery has a high energy density, especially for a system that depends on the reserve capacity of the battery to operate continually when energy scavenging is not available. For such a case the size of the hybrid power system is most likely limited by the reserve capacity of the battery and can be reduced if the energy density of the battery is improved. For example, a simple calculation shows that the size the battery can be reduced from 0.36 to 0.10 cm^2 (assuming same depth of discharge) by improving the energy density of the battery from 2.5 to 8.5 J/cm^2. With the area of solar cells and control circuit of 1 mm^2 (Harb et al. 2002), the size of the power supply will be reduced to about 0.11 cm^2. Therefore, an energy density of ~8.5 J/cm^2 is desirable for a 0.1 cm^2 battery to use in a continually operating microsensor. As a microsensing system could be turned off when energy scavenging is not available, the high energy density requirement was not set as a primary target in this study.

It is also desirable that the battery is rechargeable in order to store the energy from the conversion device and have sufficient life expectancy, as the operational life of the hybrid power system is limited by that of the battery (Harb et al. 2002). The actual life requirement will depend on the application; for example, a cycle life of 1000 cycles is required for a lifetime of one week if a cycle lasts 10 minutes (Harb et al. 2002).

There are other desirable characteristics of the battery. For example, the battery must work in the environment that the microsensor is to be placed. These parameters, including temperature, are not discussed here.

1.4 CHOICE OF MICROBATTERIES

Microbatteries of various chemistries and structures have been developed or are under investigation. Table 1.1 lists some microbatteries and their performance. It can be seen that most of them are solid-state lithium systems (e.g. Neudecker et al. 2000, West et al. 2002). With a working voltage up to 4 V per cell, this type of battery utilizes an intercalation compound as the cathode, a metallic lithium anode, and a solid-state electrolyte. The best reported performance of thin-film lithium microbatteries was a power capability[1] of 30 mW/cm^2, with a low rate energy density of 2.16 J/cm^2 (Neudecker et al. 2000). It is also noted that a thick-film lithium-ion microbattery demonstrated the highest area specific capacity (3.6 C or 1.0 mAh per cm^2, Wathena et al. 2004), corresponding to an energy density greater than 10 J/cm^2.

The highest power density was demonstrated by a rechargeable Ni/Zn microbattery developed at BYU (Humble et al., 2001, Humble and Harb 2003). The microbattery consists of microfabricated NiOOH and Zn electrodes on a Si wafer with an aqueous KOH electrolyte saturated with ZnO. With an area of 3.6 mm^2/cell and a working voltage of about 1.5 V, these rechargeable batteries have an energy density of 1.63 J/cm^2 and a power capability of ~140 mW/cm^2 (based on total cell area).

[1] Since area is of more concern than thickness, most comparisons are made on area basis.

Table 1.1 Summary of selected previous microbattery works

Battery Chemistry	Potential (volts)	Capacity (C/cm^2)	Power	Note and Reference
Ag/Pt or I_2	~0.6		Low	Impractical due to high cost, Julien and Nazri (1994)
Li/TiS_2	1.8-2.5	0.36	Low, ~4 mW/cm^2	Solid electrolyte, Jones and Akridge (1995)
Li/$Li_x(Mn_y Ni_{1-y})_{2-x}O_2$	2.5-4.2	~0.4	Low	Solid LiPON electrolyte, Neudecker et al. (1998)
Li/$LiCoO_2$	3.0-4.2	0. 7	Moderate, ~30 mW/cm^2	Solid LiPON electrolyte, "lithium free", Deudecker et al. (2000)
Li/$LiCoO_2$	2.5-4.1	~0.04	Low, ~4 mW/cm^2	Solid LiPON electrolyte, West et al. (2002)
Li/$Li_{0.33}MnO_2$	2.0-3.5	~2	Low, ~4 mW/cm^2	Solid Polymer electrolyte, Wang et al. (2003)
Ni-Zn	1.2-1.5	1.17	High, 140 mW/cm^2	Aqueous liquid electrolyte, Humble and Harb (2003)
C/$LiCoO_2$	3.0-4.2	~3.6	Low, 2.4 mW/cm^2	Direct laser writing, thick-film, Wathena et al. (2004)

The comparisons between these two types of battery chemistries indicate that lithium batteries have a higher cell voltage (up to 4 V) than the Ni/Zn batteries (~1.5 V). This will be an advantage for lithium batteries in cases where a voltage higher than 1.5 V is required, since fewer lithium cells than Ni/Zn batteries are needed to connect in series to provide a particular voltage. More importantly, the practical energy density achieved with commercial lithium type cells (400 Wh/L or 1440 J/cm^3) is more than 3 times higher than that of Ni/Zn cells (80-120 Wh/L or 288-432 J/cm^3, Linden and Reddy 2001). Assuming the ratio remains about the same for microfabricated cells, the energy of a lithium microbattery will be more than 3 times than a Ni/Zn microbattery of the same size. When the battery size is limited by its reserve capacity, the size can be more than 3 times smaller for a lithium microbattery than a Ni/Zn microbattery.

Lithium batteries have other advantages over Ni/Zn batteries. For example, lithium batteries have an higher charge efficiency (99 % vs. 85 % on capacity basis), a better capacity retention than Ni/Zn batteries (2 % vs. 20 % loss per month at ambient temperature) and a longer

cycle life (1000 cycles vs. 500 cycles, Linden and Reddy 2001). Therefore, a micropower system using lithium batteries can store energy more efficiently and have a potential longer cycle life than a system using Ni/Zn batteries.

Based on these comparisons, a lithium battery was selected as the subject of this study. More specifically, a lithium-ion battery, which is a type of lithium battery that uses an intercalation anode, was the subject of this study. It is noted that solid-state lithium batteries have rather poor power performance, which does not meet the target 50 mW/cm^2. Several factors account for the poor power performance, which include poor conductivity of the solid electrolyte, high resistivity of the electrode material and limited electrode film thickness. On the other hand, lithium-ion cells that use a porous electrode structure with a liquid-state organic electrolyte do not have the above limitations. Therefore, this study adopted a porous electrode structure combined with a liquid-state organic electrolyte to improve the power capability of the microbattery, as will be illustrated in the following chapters. It was believed that such a lithium-ion microbattery could be implemented with microfabrication techniques.

1.5 SUMMARY

Suitable micropower systems are needed to make the autonomous microsensors a reality. A hybrid micropower system, which consists of an energy conversion device and a microbattery, appears to be a promising solution to meet the power and energy requirements with a minimal size. A microbattery will be used to provide the peak power and reserve energy for operation of microsensors.

The purpose of this study was to develop and demonstrate a Li-ion microbattery with performance suitable for use in a hybrid micropower system. Li-ion was the battery chemistry of

choice because of its high working voltage, higher energy density and potentially long cycle life. An increased fundamental understanding of the factors that limit microbattery performance was critical to the success of this study. Finally, the development of a fabrication procedure for the desired batteries represented a key part of the present work.

CHAPTER 2: BACKGROUND

It is desirable to develop a high power lithium-ion microbattery to enable the microscopic autonomous sensing devices. While solid-state thin-film lithium batteries have received a lot of attention, their poor power performance makes them unsuitable for hybrid micro power systems. Therefore, it is important to examine the limiting factors in the power performance of batteries, compare the existing lithium battery structures in that context, and develop a strategy to implement a microbattery that can meet the requirements of a range of microsensing systems.

2.1 LIMITING FACTORS IN POWER PERFORMANCE

Batteries[2] are electrochemical devices which convert chemical energy into electrical energy by electrochemical reduction and oxidation reactions. The reduction and oxidation reactions take place on the cathode and anode, respectively, during discharge.

The maximum capacity of a battery, also noted as theoretical capacity, is the amount of charge that can be transferred between the two electrodes at a very low current. At this current level, the potential loss inside the battery is negligible and voltage of the battery is virtually the open circuit potential (OCP). The capacity is denoted in coulombs or Ampere-hours (1 mol equivalent electrons is 96487 coulombs, 1 Ampere-hour = 3600 C or 1 mAh =3.6 C).

It is desirable to access all the charge that a battery stores; however, losses occur when a current of a significant level runs through the battery and the battery voltage is reduced, due to

[2] Battery and cell are used interchangeably in this dissertation, unless stated otherwise.

potential drops inside the battery. These losses include: (1) activation polarization, which drives the electrochemical reactions at the electrode surface; (2) concentration polarization, which arises from differences in the concentration of the reactants and products at the electrodes' surface and in the bulk as a result of mass transfer and (3) ohmic polarization, which is a voltage drop due to the internal resistance of the cell (therefore it is also referred to as "IR drop"). These polarization effects consume part of the energy, which is given off as waste heat, and reduce the useful capacity of the cell (Chapter 2, Linden and Reddy 2001).

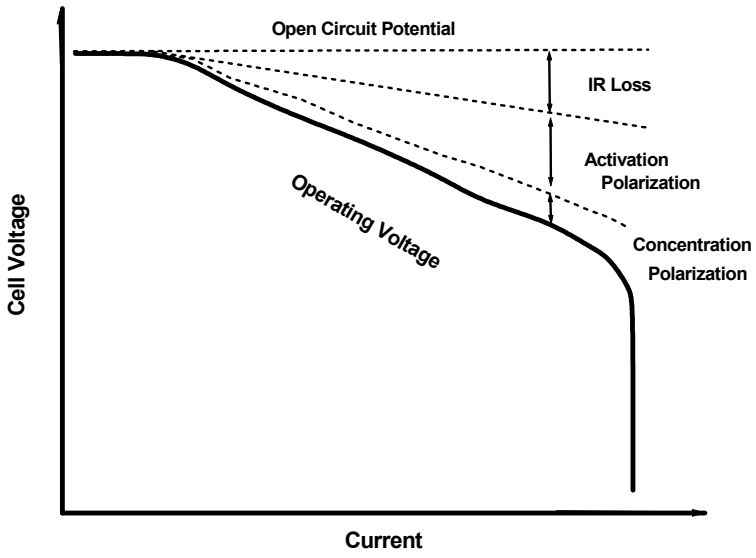

Figure 2.1 Effects of polarization on the battery voltage (redrawn from Linden and Reddy 2001)

It can be clearly seen from Fig. 2.1 that at a certain current level, the contributions of various polarizations to the overall potential loss are different. It can also be seen that the polarization effects become more severe as the current increases; therefore, the cell operating voltage decreases. As a result, at a higher current level (which usually corresponds to a higher power level), more energy is consumed by polarizations and less energy is delivered to the load. In

other words, less capacity of the cell can be accessed at a higher power level, if the cut-off voltage remains the same.

To improve the power performance of the cells, one or more of the polarization effects needs to be reduced. The approach should be specific for each polarization since the polarizations arise from different mechanisms. Activation polarization is determined by the electrochemical reactions of the electrode materials. For a certain electrode material, the activation polarization can be reduced by increasing the surface area accessible to the reactions. The concentration polarization is determined by ionic transport in the battery and can be reduced by improving mass transfer. The ohmic drop is caused by the internal resistance, or internal impedance, which consists of the ionic resistance of the electrolyte in the separator and electrodes, the electronic resistances of the electrode layers and the current collectors, and the contact resistance between the electrodes and the current collectors (Chapter 2, Linden and Reddy 2001). These resistances usually do not change with current, leading to a linearly increasing ohmic overpotential with increasing current. Improving ionic transport and electronic conductance in the electrodes can effectively reduce the internal resistance and hence decrease the ohmic polarization.

For a specific battery, the dominating resistance limiting its power performance should first be identified, and should then be reduced with a corresponding approach. It should be noted that it may be impractical to minimize all polarizations in some cases. It should also be noted that in practice, a specific approach may simultaneously affect more than one type of resistance.

2.2 AN OVERVIEW OF LI-ION BATTERIES

2.2.1 PRINCIPLE OF OPERATION OF LITHIUM-ION BATTERIES

Most lithium (-ion) batteries operate via intercalation, which is an incorporation process of Li^+ ions into the crystal lattice of electrode materials. Generally the rocking chair concept is used to describe the intercalation and de-intercalation processes of Li^+ ions in the batteries. Figure 2.2 illustrates the charge and discharge processes of a lithium-ion battery using the electrode materials adopted in this study. During the discharge process, lithium ions de-intercalate from the crystal structure of the negative electrode, diffuse to and intercalate into the crystal structure of the positive electrode. The electrons are released from the negative electrode and move to the positive electrode through the external circuit. The reverse occurs during the charge process.

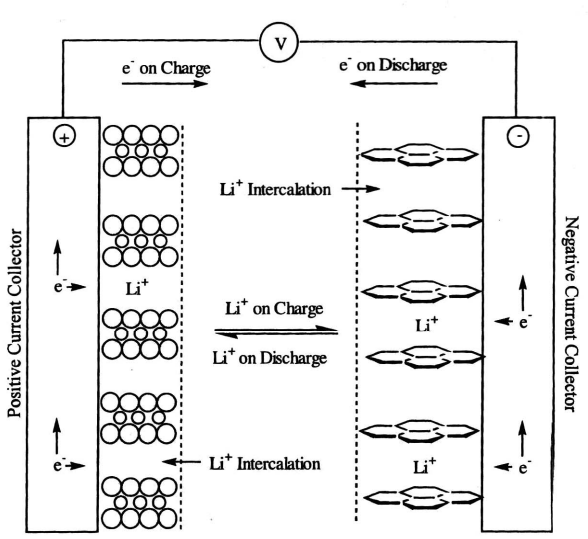

Figure 2.2 Operation of a lithium ion battery (Adapted from Chap. 35, Linden and Reddy 2001)

The electrode and overall reactions are shown in Eqs. (2.1) - (2.3), using the active materials adopted in this study ($0 < x < 1$). Note that the reactions show the stoichiometric balance of charge, and actual electrode material compositions will be determined by the state of charge (SOC).

Positive electrode: $$Li_{1-x}Al_{0.14}Mn_{1.86}O_4 + xLi^+ + xe^- \underset{Charge}{\overset{Discharge}{\rightleftharpoons}} LiAl_{0.14}Mn_{1.86}O_4 \qquad (2.1)$$

Negative electrode: $$LiC_6 \underset{Charge}{\overset{Discharge}{\rightleftharpoons}} Li_{1-x}C_6 + xLi^+ + xe^- \qquad (2.2)$$

Overall reaction: $$Li_{1-x}Al_{0.14}Mn_{1.86}O_4 + LiC_6 \underset{Charge}{\overset{Discharge}{\rightleftharpoons}} LiAl_{0.14}Mn_{1.86}O_4 + Li_{1-x}C \qquad (2.3)$$

A lithium-ion battery is a dynamic system whose performance depends on its construction, the materials, the rates of charge and discharge, the state of charge (SOC), and the operation temperature (Wright et al. 2002). The electrode reactions are complex processes that can be divided into many elementary steps, including transportation of Li^+ through the bulk electrolyte solution, migration of Li^+ through the surface film (solid electrolyte interface, SEI) of the electrode, charge transfer at the film/electrode interface, solid diffusion of lithium in the bulk of the electrode material, and accumulation of lithium within crystallographic sites in the bulk electrode material (Markovsky et al. 1998). At the same time, electrons overcome the resistance between the current collector and electrode films, the resistance among the electrode particles, the resistance of the SEI layer, and reach the SEI/electrode interface where charge transfer occurs (Aurbach et al. 1999, Wright et al. 2002).

It should be noted that the battery reaction rate depends not only on the chemistry of the electrode materials, but also depends on the battery and electrode designs. As outlined in Section 2.1, the rate-determining step is associated with the largest polarization drop in the battery. Later

in Section 2.2.4 the performance of two electrode structures will be compared. Battery performance is improved by determination and mitigation of the factors that limit performance.

2.2.2 ELECTRODE MATERIALS

Rechargeable lithium-type batteries (discussions in this dissertation are limited to rechargeable batteries) generally use intercalation compounds for the positive electrodes (which are cathodes during discharge). Lithium (metal) batteries use lithium as the negative electrode material, while lithium-ion batteries use intercalation compounds. The active materials for the cathode are principally transition metal oxides such as $LiCoO_2$, $LiNiO_2$, or $LiMn_2O_4$. The active material for the anode is typically a form of carbon (such as coke, graphite, or synthetic mesocarbon microbeads, MCMB). The characteristics of several important electrode materials are summarized in Table 2.1.

Table 2.1 Some electrode materials and their characteristics

	Active material	Voltage vs. Li (V, midpoint or range, at 0.05 C)	Theor. capacity (mAh/g)	Electrical conductivity (S/cm)	Li^+ diffusion coefficients (cm^2/s)
Cathode	$LiCoO_2$	3.88	155	10^{-3} Note *1	$5x10^{-9}$
	$LiNiO_2$	3.55	200		$2x10^{-7}$
	$LiMn_2O_4$	4.00	120	$4.8x10^{-5}$	$10^{-12\sim-9}$
Anode	LiC_6 (MCMB)	0-0.1	300	$1.37x10^{-3}$ Note *2	
	$Li_{0.5}C_6$ (coke)	0-1.3	180		
	Graphite	0-0.5	360	$10^{1\sim5}$ Note *3	$10^{-10\sim-8}$ Note *4

Note: Data cited from Linden and Reddy (2001) unless otherwise stated.
*1: Me´ne´trier et al. (1999)
*2: Deab (1979)
*3: Shirahige and Deyama (2004)
*4: Aurbach et al. (1998)

$LiCoO_2$, $LiNiO_2$, and related materials have layered lattice structures. $LiCoO_2$ is the first commercialized (Nagaura and Tozawa 1990) and most commonly used positive electrode

material, with a good capacity (155 mAh/g) and a high working voltage (3.9 V vs. Li). However, the toxicity of cobalt is a drawback of this material. Furthermore, the elevated price of cobalt increases the cost of this material and precludes any practical use of this material in large batteries (e.g. electrical vehicles, Broussely et al. 1999).

Although with a much higher capacity (200 mAh/g), $LiNiO_2$ has very limited commercial use due to its instability and safety issues, which relate to the formation of NiO and oxygen (Linden and Reddy 2001). The synthesis of this material is more difficult than that of $LiCoO_2$, due to the formation of a nickel over-stoichiometric phase which leads to a lower extractable lithium and poorer electrochemical performance (Broussely et al. 1999).

$LiMn_2O_4$ offers the highest voltage (4.0 V vs. Li) with a low capacity (120 mAh/g), and is of increasing commercial interest because of its better rate capability, lower cost, less toxicity and excellent safety properties, as compared to $LiCoO_2$. However, pristine lithium manganese oxide suffers from higher rate of capacity fading during cycling or storing, especially at higher temperatures. The capacity fading has been attributed to the Jahn-Teller effect, structure instability at high potentials or manganese dissolution (Broussely et al. 1999). Substitution for manganese by other elements such as aluminum (Noddapaneni and Ingersoll 1996, Pistoia et al. 1997) and cobalt (Guohua et al. 1996) improves the fading at the cost of reducing capacity to 100-110 mAh/g.

Coke-based materials were used in the first commercial lithium-ion batteries by Sony in 1990, offering capacity of about 180 mAh/g (Linden and Reddy 2001). Since the mid-1990s most Li-ion cells have utilized graphitic spheres, e.g. MCMB, in anodes based on the higher specific capacity (about 300 mAh/g), lower irreversible capacity and good safety properties. More recently, natural graphite (lower cost and capacity of 350 mAh/g) and some hard carbons (over 1000 mAh/g) have been used in some cells (Linden and Reddy 2001).

It should be noted that most commercial Li-ion cells emphasize energy density instead of power density. The choice of an electrode material against other materials usually results from compromises among performance, electrode processing and cost. The physical properties of the particulate electrode materials are usually low surface area (on the order of a few m^2/g), diameter of 5-30 μm, and a high material loading (Broussely et al. 1999).

It is important to identify the limiting electrode in order to efficiently improve the power performance of the battery. From Table 2.1, it can be seen the diffusion coefficients of Li^+ in these positive and negative electrode materials fall in the same range; however, the intrinsic electrical conductivities of the positive electrode materials are significantly lower than those of the negative electrode materials. Since these two parameters determine the Li^+ solid diffusion and intrinsic electron conductance, it is expected that the positive electrode would be of inferior electronic conductance, and that the power performance of lithium-ion batteries would be limited by the positive electrode. This is supported by comparison data of AC impedances among graphite, $LiCoO_2$, $LiNiO_2$ and $LiMn_2O_4$ electrodes, which shows that the graphite material has a much smaller impedance than the other three materials (Aurbach et al. 1998). Therefore, it was determined that the positive electrode would be the focus of investigation of improving battery power performance in this study.

Many new electrode materials have been proposed and investigated in recent years, aiming at higher capacity or better electrode performance. Positive electrode materials include vanadium oxide, lithium iron phosphate and other compounds; the negative electrode materials include hard carbon, tin compounds, silicon compounds and others. This study focuses on improving the power performance by identifying and reducing dominating resistances and developing a microfabrication process, it is not designed to be an extensive electrode materials study. The approach to improve power performance should be general and applicable to other

electrode materials that have similarly limited power performance. Hence a review of these new electrode materials is not included here. Reviews of these materials can be found in Broussely et al. (1999) and Scrosati (2000), Linden and Reddy (2001), Tirado (2003) and Julien (2003).

2.2.3 ELECTROLYTES

Choice of an appropriate electrolyte is important to the proposed Li-ion battery in order to minimize concentration polarization and the ohmic drop due to ionic transport in order to achieve high power performance. Of course the electrolyte of choice should be compatible with the battery microfabrication process. The three categories of electrolytes used in lithium-type batteries (liquid electrolyte, polymer electrolyte and solid-state electrolyte) will be discussed in this section.

Liquid electrolyte has the highest ionic conductivity (10^{-3}~10^{-1} S/cm, Linden and Reddy 2001) of the three electrolytes. Liquid electrolytes are solutions of a lithium salt in organic solvents. The most commonly used salt is $LiPF_6$, based on its high ionic conductivity in solution (>10^{-3} S/cm), high Li^+ transference number (~0.35) and acceptable safety properties. Many other salts, including $LiBF_4$, $LiAsF_6$, $LiClO_4$, $LiN(SO_2C_2F_5)_2$ and LiBOB (Li bis (oxalato)borate), have also attracted R&D and industrial interests (Linden & Reddy 2001, Aurbach et al. 2004). The solvents are mostly carbonates, including ethylene carbonate (EC), diethyl carbonate (DEC), propylene carbonate (PC), ethyl methyl carbonate (EMC) and dimethyl carbonate (DMC). These carbonates offer excellent stability, compatibility with electrode materials and good safety properties. Generally a formulation of two to four solvents is used, in order to achieve higher ionic conductivity, and a broader operating temperature. For example, the 1.0 M $LiPF_6$ / (EC:DEC 1:1 wt) electrolyte has a conductivity of 7.0×10^{-3} S/cm at 20 °C and can operate in the range of -40 °C to 80 °C (Linden and Reddy 2001).

High ionic conductivity and an easily maintained interface between liquid electrolytes and electrodes are very attractive to the proposed microbattery. Using such an electrolyte will effectively minimize the concentration polarization in the electrolyte phase and improve the ionic transport, improving high power performance of the battery. It should be noted that one drawback of liquid electrolytes is safety concerns due to the leakage of solvents when packages of batteries are broken. It should also be noted that the performance of this type of electrolyte is very sensitive to moisture (Aurbach et al., 1999); hence it is usually handled in a controlled dry environment. With respect to microbattery fabrication, a controlled environment is required to use a liquid electrolyte; in addition, a special handling technique is required since generally only solid-state thin-film components exist in standard microelectronics. Both requirements may present some fabrication challenges.

The second type of electrolyte, polymer electrolyte, refers to a solid solution formed by dissolving a salt in a high molecular weight polymer (Linden and Reddy 2001). Strictly speaking, solid polymer electrolyte (SPE) contains no liquid components, such as volatile and flammable solvents; therefore, the safety properties are improved over the liquid electrolytes by eliminating leakage hazards. However, the ionic conductivity is usually lower than 10^{-4} S/cm due to the high viscosity.

Modifications to the dry SPE led to two polymer electrolytes that are more commonly used: gelled SPE and porous SPE. The former includes some physical or chemical cross-linking PAN, PMMA, P(VDF-HFP) and PEO polymer electrolytes; the latter includes some porous P(VDF-HFP) systems (Murata et al., 2000). Disregarding the difference, the gelled or porous SPEs are both hybrid electrolytes containing liquid electrolyte in the polymer phase; therefore they have the high ionic conductivities of the liquid electrolyte and the safety properties of the dry polymer electrolyte. Ionic conductivities as high as 10^{-3} S/cm at room temperature were reported in the

literature (Kim et al., 1999; Murata et al., 2000; Linden and Reddy 2001; Cheng et al. 2004; Sannier et al. 2005). It should be noted that a controlled dry environment is required for processing a gel-type or porous SPE, due to the involvement of liquid electrolytes.

The third type of electrolyte, solid-state electrolyte, is generally used in lithium thin-film batteries. One representative material is lithium phosphorus oxynitride (LIPON), developed by the Oak Ridge national laboratories (Bates et al. 1993). This material has long-term stability in contact with metallic lithium and can operate over a wide temperature range. Its ionic conductivity is very low (about 10^{-6} S/cm), hence the internal resistance of an electrolyte thicker than a few micrometers will be too large for practical uses; moreover, the stiffness of the glass-like electrolyte makes it difficult to maintain a satisfactory electrode/electrolyte interface (Julien and Nazri, 1994). Both of these factors limit the power capability of the solid state thin-film batteries to generally less than 1 mW/cm^2 (Bates and Lubben et al., 1995; Dudney et al., 1999; Baba et al., 1999). The highest power density demonstrated by a battery with LIPON electrolyte was 30 mW/cm^2 (Neudecker et al. 2000), which is still insufficient to meet the 50 mW/cm^2 goal of this study. As the batteries using this type of solid state electrolytes have other constraints limiting their power performance (as will be demonstrated later in this chapter), it seems unlikely that the solid state electrolyte will be a good choice for the proposed microbattery.

The solid electrolyte interface (SEI) is an important phenomenon related to the electrolytes and warrants some discussion here. The SEI is a passivation film on the electrode surface to stabilize the intercalation system (Linden and Reddy 2001). SEI forms on both electrodes; however, generally the anode shows the dominant SEI phenomenon. Generally the SEI film is formed during the first cycle, by reactions between lithium and solvents in the electrolyte; once a stable film is formed, it can prevent further consumption of lithium in this irreversible process and ensure the long operation of the cells (Aurbach et al. 1999).

It was shown that electrolytes containing alkyl carbonates, in particular EC, form the passivation film with a minimum amount of lithium. Esters such as EMC also form stable SEI films. Most other solvents do not form stable SEI films (Linden and Reddy 2001) and additives are required for the electrolytes that do not contain alkyl carbonates or ethers to obtain good cycling performance of the cells.

It should be noted that SEI is a phenomenon not only related to long-term stability, but also to the power performance. An unstable SEI film will continuously consume available lithium source and grow in thickness, leading to increased surface film resistance (Kim and Yoon 2004) and deteriorating the power performance of the cells. Therefore, the choice of proper solvents in liquid and polymer electrolytes is important to ensure long term cyclability and power capability of the cells.

In summary, based on power performance considerations, liquid electrolytes and gelled SPE are better candidates than solid state electrolytes for the proposed high power microbattery. Proper solvents should be chosen for these two types of electrolytes to attain stable SEI and achieve long term cyclability and high power performance of the cells.

2.2.4 ELECTRODE STRUCTURES

Lithium-ion cells can be divided into two groups according to the electrode structure: thin-film and composite cells. Figure 2.3 shows a schematic comparison of these two groups. Distinct differences exist in the morphology, composition, electrolytes, and the thickness of the electrodes between these two types of cells.

A thin-film battery consists of solid state thin films of electrodes and electrolyte. Each layer is a dense film of a few micrometers in thickness, generally deposited by sputtering or other IC techniques. TiS_2, $LiMn_2O_4$ and $LiCoO_2$ had been used in the thin-film batteries as cathode

materials, and lithium had been the general choice for anode material. Examples of electrolytes include lithium-ion conducting glass xB_2O_3-yLi_2O-Li_2SO_4 (Jones and Akridge 1995) and solid-state lithium phosphorus oxynitride (LIPON) (Bates et al. 1993, Neudecker et al. 1998).

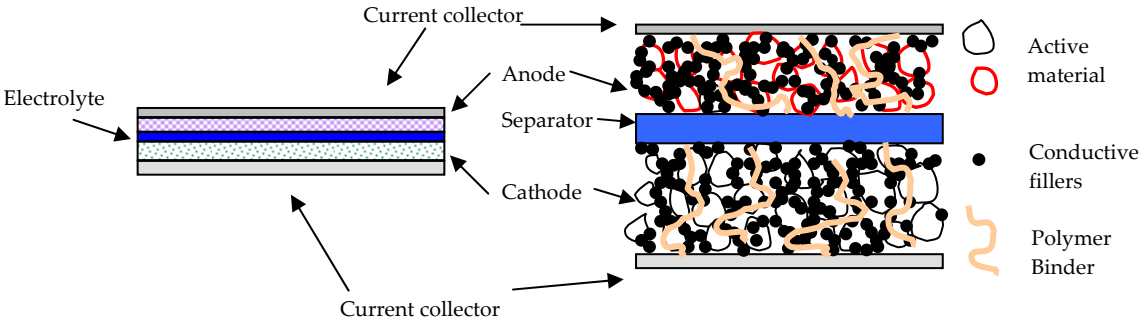

Figure 2.3 Diagrams of thin-film and composite Li-ion batteries (not to scale)

This type of all-solid–state thin-film battery has been adopted by most microbatteries studies (e.g. Brousse et al., 1997, Baba et al., 1999, Neudecker et al., 1999). It should be noted that, although its solid state morphology seemed to be compatible with the standard IC process techniques, significant technical challenges exist including the controlled environment needed for the fabrication of lithium anodes. After more than 15 years of development the limited applications of thin-film lithium batteries have not included remote microsensors.

The power performance of the thin-film batteries is limited by several factors. Generally the poor intrinsic ionic transport properties and electronic conductivities of the electrolyte and cathode materials are among those factors, as they are used in the pure forms (i.e. without additives). For example, LiPON electrolyte has an ionic conductivity of ~10^{-6} S/cm, $LiMn_2O_4$ has a solid lithium diffusion coefficient of ~10^{-9} cm^2/s) and an electronic conductivity of ~10^{-5} S/cm. Therefore, thin-film solid state batteries generally are only capable of low to medium discharge rates. For example, a cell using TiS_2 cathode was able to deliver continuous current at 0.30 mA/cm^2 and a pulse current at 2.0 mA/cm^2 (Jones and Akridge 1995).

Furthermore, the large resistance due to the poor transport properties and electrical conductivities, with the mechanical stability and the adhesion of the thin-films, limit the electrode film thickness to less than about 1-5 μm (Neudecker et al. 2000). Therefore, although these batteries are often credited with high volumetric energy densities, their area specific capacity is quite limited due to the small electrode film thickness. Typical values are in the range of 0.035-0.20 mAh/cm^2 (0.126-0.72 C/cm^2) with a total cell thickness of 8-12 μm (Neudecker et al. 2000, Sukumar et al. 2004).

The best power performance of any thin-film cell in the literature was demonstrated by a "lithium-free" thin-film battery developed at the Oak Ridge National Laboratories (Neudecker et al., 2000). It is worthy to mention that this cell was fabricated in the discharged state, without any metallic lithium. It also allowed the cell to withstand normal solder processes during which the temperature was higher than the melting point of lithium metal. During the charge step of the first cycle, the metallic lithium was plated on a copper current collector and the cell functioned as a lithium battery thereafter. These "lithium-free" cells operated between 4.2 and 3.0 volts and had capacities up to 0.20 mAh/cm^2 (0.72 C/cm^2) at a current density less than 0.1 mA/cm^2. A current density of 10 mA/cm^2 was demonstrated with about 30% of the theoretical capacity. The power density at such a current level was about 30 mW/cm^2 and may be useful for some microsystems, although it is still insufficient for the targeted power density of 50 mW/cm^2. Note it was demonstrated with only one good cell and others had higher resistances (Bates 2000). It should be noted that the volume change of the in-situ plated lithium anode caused stress and damage to the sealing layer and limited the cell life (Neudecker et al. 2000). The "lithium free" strategy is not currently used.

Composite electrodes have been generally used in large-sized batteries. The electrode films are particulate mixtures of active material, conductive additives, and a polymer binder, which are

mixed into a paste (slurry) with a solvent agent (e.g. *n*-methyl pyrrolidone solvent, NMP) and laminated onto metallic current collectors. One example of a cathode recipe is (11wt%) binder (polyvinylidenefluoride, PVDF) : (72 wt%) $LiMn_2O_4$: (17 wt%) conductive additive (carbon black, CB), with corresponding volume ratios of (10.4%) PVDF : (28.4%) $LiMn_2O_4$: (14.5%) CB : (46.7%) pore volume (Lazarraga et al. 2003). Generally an organic liquid electrolyte or gel-polymer electrolyte is used with composite batteries, which fills the porous structures in the electrode films.

Several factors contribute to performance of the composite batteries, including the conductive additives, small active material particle size, porous structure and the electrolyte. Generally a form of carbon, with the most common choice being carbon black (electronic conductivity of ca. 1 S/cm at room temperature, Lazarraga et al. 2003), is used in the composite cathodes to improve the electron conduction among the active material particles. The active materials are usually fine particles with diameters in the micrometer ranges, in order to minimize the effect of poor ionic transport in the solid phase. The liquid or polymer electrolyte in the pores of the electrode films greatly facilitates the ionic transport outside the active material particles, as compared to that in the solid state thin-film batteries.

The enhanced electron and ion transport in the composite electrodes, as compared to those of the pure active materials, reduces the resistances and allows the materials to be accessed at a greater film depth than the thin-film electrodes. Therefore, the composite electrodes are generally built much thicker (on the order of 100 μm) than the thin-film electrodes and have a much higher area-specific material loading. For example, a $LiMn_2O_4$ composite cathode had a capacity of 1.9 mAh/cm^2 (6.8 C/cm^2) (see the experimental data in Doyle and Newman et al. 1996), and a batch of $LiCoO_2$ cathodes had capacities of about 3.0 mAh/cm^2 (10.8 C/cm^2) (Ahn 1998).

These capacities were at least 10 times higher than those of thin-film batteries (e.g. Neudecker et al., 2000).

Since the area-specific active material loadings in composite electrodes are much higher than that of thin-film electrodes, and since the ionic and electronic conductivities are superior to those in the thin-film batteries, it was expected that the high-power performance of composite batteries should be superior to that of the thin-film batteries. However, since most commercial batteries have been built emphasizing energy densities, the power data were seldom reported. The experimental data reported in Doyle and Newman et al. (1996) showed that a composite battery consisting of 128 μm thick Li_xC_6 anode and 190 μm thick $LiMn_2O_4$ cathode delivered ~2.3 mAh/cm^2 (8.3 C/cm^2) at 0.42mA/cm^2, ~1.7 mAh/cm^2 (6.1 C/cm^2) at 4.2mA/cm^2, 0.55 mAh/cm^2 (2.0 C/cm^2) at 14.6 mA/cm^2.

From the above comparative illustration of thin-film and composite batteries, it can be seen that composite electrodes (batteries) exceed the capabilities of thin-film electrodes (batteries) in aspects of area-specific capacity and power densities. The experimental data in Doyle and Newman et al. (1996) indicated that a slightly higher current (about 17 mA/cm^2) should be achievable with the reported composite battery configuration; if the cut-off voltage is set at 3.0 V, a power level of 50 mW/cm^2 can be achieved (which meets the power requirement of the autonomous microsensors). Therefore, it seems that using porous composite electrode structures in the proposed microbattery has the promise to meet the performances (especially the power) requirements. The questions remaining are how to maintain the performance of large cells at a 0.1 cm^2 scale, and how to build this micro-sized composite battery using IC-compatible techniques.

2.3 PERFORMANCE ISSUES OF MICRO COMPOSITE BATTERIES

As battery size decreases, performance does not necessarily scale down. This is an issue in the case of our targeted microbattery as the thickness is in the sub-millimeter range and the area is in the sub cm^2 range. This issue can be discussed in two parts. The first part limits the choices of electrode structure and affects the volume efficiency, and is related to the fabrication method of the micro-sized cells and will be discussed in Section 2.4. The second part of the issue, which is related to some factors that are present in the large cells but not in the micro cells, will be discussed in this section.

2.3.1 CARBON BLACK AND COMPRESSION

As illustrated previously, a composite $LiMn_2O_4$ cathode generally consists of $LiMn_2O_4$ particles, carbon black (CB) additives and PVDF binders. It is understood that generally the CB content determines the electronic conductivity of the composite film and is critical to the electrode performance. For example, Mandal et al. (2001) showed that both the electronic conductivity and the discharge capacity of cold-pressed composite $LiMn_2O_4$ cathodes depended on the carbon black content in the same manner. Later they showed a similar result for laminated composite $LiMn_2O_4$ cathodes (Lazarraga et al. 2003). In these studies, it was demonstrated that below a certain fraction of CB (about 3 vol%), the electronic conductivity of the composite is dominated by the active material, and the composite electrode doesn't show significant electrochemical capacity. The electronic conductivity and capacity of composite electrodes increase sharply for a CB fraction close to 3 vol%. After the CB fraction is greater than 10-15 vol%, the conductivity and low-rate discharge capacity become almost constant regard to the change of the CB volume content.

The above studies identified that for low discharge rates, a CB volume fraction of >10-15% is required to ensure high accessibility of the active materials in the composite cathodes. At higher discharge rates (which will be the operating mode of the proposed microbattery to provide high power), a higher CB volume fraction may be needed. This will produce a lower theoretical capacity since less electrode volume is available to active material. Therefore, there seems to be a CB volume fraction at which the accessible electrode capacity at high discharge rates will reach a maximum. In other words, the conductive filler content needs to be studied to balance the cell for optimal high power performance.

It should be noted that composite electrodes need to be compressed to attain good performance, as indicated in Ahn (1998), Gustafson et al. (2002), Hamano et al. (2002), Striebel et al. (2003), and Cheng et al. (2005), etc. Without compression the electrode performance is compromised. Holladay (2000) showed that the capacity fade rate of uncompressed $LiAl_{0.14}Mn_{1.86}O_4$ composite cathodes (about 0.18 %/cycle) was significantly higher than that of the compressed ones (about 0.1 %/cycle). It should also be noted that the effect of compression on the MCMB composite anodes is less significant (Holladay 2000), possibly due to the higher intrinsic electronic conductivity of the MCMB materials relative to that of lithium manganese oxide.

The influence of compression on the performance of these CB containing composite cathodes is not fully understood, but is believed to relate, at least in part, to the integrity of a conductive network formed by CB particles (Jarman 2001). In the composite electrodes, CB powders (or other graphite particles) form particulate conducting paths by point-to-point contacts among the particles, facilitated by compression (Lin and Harb 2004). Obviously, the compression tends to decrease the gap and increase contact areas among the CB particles, leading to reduced contact resistances along the conducting paths. It is also easy to understand that the

effect of compression on the quality of the conduction network will depend on the morphology and the volume fraction of the conductive particles.

A number of different mechanisms are used to provide compression to composite electrodes. In commercial cells, the composite electrodes are compressed during a calendering (compressing) step, and the pressure is maintained by winding the electrode films and separators into rolls and inserting them into a tightly fitting container. In the laboratory, flat cells are usually tested under pressure.

In these large commercial batteries, compression does not increase fabrication complexity, as it is achieved simultaneously as the electrode films are calendered to increase the material loading (Linden and Reddy 2001). However, as large batteries are energy oriented while the proposed microbattery is power oriented, it was expected that calendering or similar techniques would not apply to the microbattery. Furthermore, compressing and maintaining pressure on micro-sized electrodes/batteries is considerably more challenging and might constrain both battery configuration and fabrication. Therefore, a microbattery that does not require compression to attain and maintain its optimal performance is highly desirable.

2.3.2 FIBROUS CONDUCTIVE NETWORK

Therefore, it became an important issue in microbatteries to build an improved conductive network in the composite cathodes that is less dependent on compression. Clearly, the ability of CB particles to form a continuous conductive network across the electrode thickness increases with the volume fraction of CB. Alternatively, replacing CB particles with some conductive materials of higher aspect ratios (length to diameter) may significantly improve the conduction network without increasing the volume fraction of the conductive additives (Wang et al. 2003).

Such an improvement in the composite film conductivity may reduce or even eliminate the battery performance dependence on the compression.

High-aspect-ratio conductive materials, particularly fibers, are very attractive candidates to improve the composite film conductivity even with a much lower volume fraction than the particulates (e.g. Cheng et al. 2001, Wang et al. 2003). Stochastic simulation studies showed that a small increase in the aspect ratio of the conductive filler significantly reduces the percolation threshold (the lowest volume fraction of conductive fillers above which at least one spanning cluster or path exists) and improves the conductivity of the network; for fibers with aspect ratio > 100, percolation (a state in which at least one spanning path exists) can be achieved with a fiber content less than 5 vol% (Wang et al. 2003). They also pointed out that alignment of fibers in a particular direction generally enhances the conductivity in that direction.

The above conclusions have been experimentally verified. Ahn (1998) showed that use of 4 wt% stainless steel fibers (2 μm in diameter, ca. 0.1 - 2 mm in length) in composite $LiCoO_2$ cathodes maximized the active material utilization at a C/40 rate, which was generally achieved with ~15 vol% of carbon black. The volume fraction of these steel fibers in the above cathodes was estimated to be ~2 vol% based on the densities of materials. Electrode performance at higher discharge rates was not reported in the above study.

Fibrous conductive materials appear to be a promising solution to improve the electronic conductivity of composite electrodes. It should be noted that the fibrous materials need to be chemically and electrochemically stable in the battery system; otherwise, long-term stability of the battery cannot be achieved. The stainless steel fibers used in the above study had some corrosion problems in the cathodes (Ahn 1998) and will not be adopted in this study.

In this context, carbon nanotubes (CNT's) seem to be an excellent choice as conductive fillers in microbatteries. Similarly to CB, CNTs are a form of carbon and are expected to be stable in

these composite electrodes. The diameter and length of the nanotubes are generally a few nanometers and a few micrometers, respectively, corresponding to aspect ratios over 1000. The electronic conductivity of metallic single walled carbon nanotubes (SWCNT or SWNT) was reported to be about ~10^4 S/cm (Thess et al. 1996), which is 4 orders of magnitudes higher than that of CB (~1 S/cm, Lazarraga et al. 2003). Although the current growth methods always produce a mixture of semiconducting and metallic nanotubes, it is expected the SWNTs are much better electron conductors than CB since the semiconducting SWNTs exhibit ballistic electron transport (Fuhrer et al. 2001).

Sakamoto and Dunn (2002) demonstrated that the use of SWNTs in a V_2O_5 cathode improved its power performance. The electrodes with CNT as conductive fillers exhibited at least 4 times higher electrical conductivity than those with same weight fraction of carbon black. The effective resistance of V_2O_5 aerogel sample is 600 kΩ/cm; with 9 wt% CNT it drops to 4.2 kΩ/cm, which is equivalent to that with 17 wt% carbon black. More interestingly, it seems that using CNT as conductive fillers brings beneficial effects besides improving the electrical conductivity. Their data show that cathodes containing 5 wt% CNT (effective electrical resistance of 15.5 kΩ/cm) delivered 210 mAh/(g V_2O_5) at a current level of 2800 mA/(g V_2O_5), while cathodes containing 17 wt% carbon black (effective electrical resistance of 3.4 kΩ/cm) only delivered 155 mAh/(g V_2O_5) at the same current level. They interpreted this phenomenon as the result of the excellent electrical contact established by nanotubes without impeding electrolyte access to the mesoporous aerogel architecture (Sakamoto and Dunn 2002).

Note that in the above study a very high normalized current density was tested (2800 mA/(g V_2O_5)). However, the material loading was only 1 to 2 mg V_2O_5/cm^2 (Sakamoto and Dunn 2002), which resulted in a power density of about 8.4 mW/cm^2 (cut off voltage at 1.5 V). Such a power density is far from sufficient for the proposed microbattery in this study.

In summary, the electronic conductivity of the composite $LiMn_2O_4$ cathodes is critical to its power performance. CB particles have been used to improve the electrode electronic conductivity, and compression is needed to achieve optimal performance of these CB containing electrodes. Such a compression was expected to be difficult to implement in micro-scale batteries; hence it was desired to reduce or eliminate the need of compression. Fibrous conductive additives, especially SWNTs, have been demonstrated to improve the conductive network and the power performance of composite electrodes. It is expected that such an improved conductive network could reduce the need of electrode compression, which would facilitate the fabrication of the proposed microbattery.

2.4 FABRICATION ISSUES OF MICRO-COMPOSITE BATTERIES

As discussed in the *Introduction* chapter, conventional battery fabrication techniques cannot be applied in the fabrication of the proposed microbattery, since such techniques do not scale down to the desired microbattery size with sufficient efficiency relative to cell volume. Therefore, microfabrication techniques similar to those being used in the microelectronics processes need to be used. This section reviews some high-volume fabrication techniques that could be applied potentially to the proposed high-power composite microbattery. The listing is not meant to be complete, but rather a collection of the techniques that may be possibly applied to the proposed microbattery.

2.4.1 THIN-FILM DEPOSITION TECHNIQUES

Thin-film electrodes have been fabricated by sputtering, pulsed laser deposition, spin-coating and other microfabrication techniques. Most of these techniques are generally used in the integrated circuits industry to form thin films in the processes of producing microelectronics.

2.4.1.1 Sputtering

Sputtering is a physical coating technique to deposit very thin films on substrates for a wide variety of commercial and scientific purposes. It is performed by applying a high voltage across a low-pressure gas to create a "plasma," which consists of electrons and gas ions in a high-energy state; the energized plasma ions strike a "target," composed of the desired coating material, and cause atoms from that target to be ejected with enough energy to travel to, and bond with, the substrate (Wolf and Tauber 2000).

Sputtering has been used to build solid-state electrodes and electrolytes, including those shown in “lithium-free” batteries (Neudecker et al. 2000 and West et al. 2002). The components in a battery developed by West et al. (2002) were prepared in a RF magnetron sputter at a pressure of less than $2x10^{-6}$ Torr. The $LiCoO_2$ sputter target was prepared by uniaxially pressing $LiCoO_2$ powder mixed with 5 wt% ethylene–propylene–diene monomer binder and sintering at 800 °C for 1 h. The Li_3PO_4 target was prepared by uniaxially pressing calcined Li_3PO_4 powder without binder and sintering at 850 °C for 1 h. The sputtered films had a thickness of 500-2000 nm.

2.4.1.2 Pulsed Laser Deposition

Pulsed laser deposition uses a pulsed laser beam to carry out a process of ablation in order to deposit materials as thin films. Generally, a high vacuum is necessary for operation. Pulses of focused laser light transform the target material directly from solid to plasma; the resulting plume of plasma is thrown perpendicularly away from the surface by thermal expansion. As expansion cools the plume, it will revert to a gas, but sufficiently high vacuum will allow momentum to carry this gas to the substrate, where it condenses to a solid state (Cheung 1994).

This technique has been adopted to make microscopic electrodes for lithium batteries (e.g. Striebel et al. 1996, Perkins et al. 2001, Song et al. 2004). Striebel et al. (1996) documented the preparation of thin films of $LiMn_2O_4$ and $LiCoO_2$ with pulsed laser deposition onto stainless steel substrates. Film deposition was carried out in the presence of 100 mTorr O_2 with 400 mJ pulses at 5 Hz for 15 to 60 min. These films have thicknesses from 0.2 to 1.5 μm and are crystalline without postdeposition annealing. Film capacity densities as high as 56 and 62 $\mu Ah/cm^2$-μm were measured for $LiMn_2O_4$ and $LiCoO_2$, respectively. Some of the films were cycled electrochemically for up to 300 cycles against lithium metal in 1 M $LiC1O_4$/ PC electrolyte, with the highest demonstrated power being 330 $\mu W/cm^2$ (Striebel et al. 1996).

2.4.1.3 Spin Coating

In a spin coating process, the materials to be coated are in the forms of a viscous solution. In the coating process, a small amount of the solution is dispensed onto the center of the substrate; then the substrate spins at a desired speed, at the same time the solution spreads over and uniformly coats the surface of the substrate.

Spin coating has been adopted to prepare thin-film electrodes (e.g. Fonseca and Neves 2004, Lei et al. 2005). Fonseca and Neves (2004) showed a spin coating process to prepare a composite

thin-film cathode. The solution they used was 95 wt% $LiMn_2O_4$ powder with 5 wt% PVDF in *N*,*N*-dimethyl acetamide. The solution was spin coated at 5000 rpm for 5 seconds on glass plates coated with a thin film indium-tin oxide. The obtained capacity of 10 $\mu A/cm^2$ and a cut-off voltage of 2.8 V was 138 mAh/g (Fonseca and Neves 2004). The corresponding power was 28 $\mu W/cm^2$.

2.4.2 COMPOSITE FILM COATINGS

The coating methods adopted in battery industries for composite electrode are generally film lamination using roll coating techniques; in laboratory studies, usually doctor-blade casting is used to produce composite films. Several other techniques, including screen printing and electrophoretic deposition, have been shown in published studies to produce composite electrodes of smaller areas.

2.4.2.1 Lamination

Industrial fabrication emphasizes continuous production; therefore, roll coating lamination is well suited for this purpose. This process features a continuous process of dispensing composite pastes onto moving current collector foil (driven by rollers), and a blade is used to control the film thickness (e.g. Xing and Smith 2002). Generally, double roller calenders located downstream of the blade compresses the electrode film after it has dried.

Doctor blade casting has been used in laboratories to make composite electrodes for research (e.g. Zaghib et al. 2004, Holladay 2000, Jarman 2000, Lin and Harb 2004). In this process, composite slurries are applied and spread onto a substrate, then a doctor blade is manually moved over the slurries multiple times to produce a uniform film of desired thickness. This

process is well suited for electrode productions where small quantities are typical. Composite electrodes of various chemistries and compositions were built using this technique (e.g. Zaghib et al. 2004, Holladay 2000, Jarman 2000).

The lamination processes appears to be suitable for producing unpatterned large composite electrodes (above 1 cm^2). The doctor blade casting will be suitable to studies of investigating electrode chemistries and compositions using cm^2 scale batteries; however, since the electrode area of the proposed microbattery will be about 0.1 cm^2 and will most likely require patterning, this technique is not suitable for micro-sized electrode fabrication.

2.4.2.2 Screen Printing

Screen printing, also called silk screening, is a technique that coats and patterns simultaneously and is used to create thick-films of non-photo definable slurry materials. In this process, a mask with openings is used, which contacts the substrate during printing. One way of silk screening is to use a squeegee to push the slurry materials into the openings. When the mask leaves the substrate, patterned slurry is left on the substrate, which is then hardened by a drying or sintering process.

The minimum feature size in screen printing is about 100 μm (Madou 1997), which is adequate for the proposed microbattery (electrode size is on the order of millimeters). Furthermore, the composite slurries in composite electrode preparations appear to be of similar viscosity of those used in screen printing, making them potentially suitable for screen printing.

This printing technology greatly facilitates changes in shape, size, and thickness of the electrodes and has been extensively used in hybrid electronics (Ghiurcan et al. 2003). Although its use has not been reported in preparations for composite electrodes for lithium batteries, it has been explored in fabrication of thick-film Zinc-alkaline microbatteries (Ghiurcan et al. 2003). In

that study, screen printed silver ink (dry thickness of 11-15 μm) on alumina substrates served as current collectors. Both electrodes were printed using a 50 μm thick stainless steel stencil in a pattern of 1 x 1 cm^2. The thickness of the printed electrode layers varied between 100 and 200 μm depending on ink preparation and number of repeated printings. The thick-film inks consisted of the required active material, binder and solvent, forming a homogeneous mixture with printable properties. Zinc-manganese dioxide cells were prepared with this process and demonstrated cycle life of about 50 cycles at 1 mA/cm^2 (Ghiurcan et al. 2003). This study pointed out that the preparation of printable inks was a key issue in this silk printing process. A deficiency of these batteries was that a proper package was lacking, which led to problems of electrolyte leakage.

2.4.2.3 Laser Direct Writing

It was recently reported that the Naval Research Laboratory developed a unique process for thick-film Li-ion microbattery fabrication (Stux et al. 2004, Wartena et al. 2004). It was called "laser direct writing", which uses a laser source to accomplish the tasks of patterning and depositing electrode materials. The key features of this technique are coating a ribbon from an ink comprising active materials, carbon additives, binder and an organic liquid onto a UV-transparent plate and then laser-forward transferring the electrode materials from the ribbon to the current collector in a succession of droplets (Wartena et al. 2004).

Electrodes of 40–60 μm thick with 4 mm x 4 mm footprints were fabricated using laser direct writing and the battery containing a liquid electrolyte was packaged in a glass material (Wathena et al. 2004). Both half cells and packaged microbatteries demonstrated capacities of approximately 155 μAh (1.67 J) or 100 mAh/(g $LiCoO_2$). The study represents a viable microfabrication method for lithium-ion batteries, with the electrodes of similar footprints to our proposed microbattery; however, the demonstrated power density of batteries fabricated by this

method was only 2.4 mW/ cm^2 (corresponding to 0.8 mA/cm^2 with a cut-off voltage of 3.0 V, see Wathena et al. 2004), which was too low to meet the power requirements of this study.

2.4.2.4 Electrophoretic Deposition

Electrophoretic deposition (EPD) is a technique to deposit particles onto a substrate. The EPD proceeds via three processes, which are particle charging, particle transport in an electric field, and deposition of particles with neutralization (Kanamura et al. 2000).

EPD processes can be used to deposit particulate mixtures (Kanamura et al. 2000, Lee et al. 2005). Kanamura et al. (2000) described an EPD process to deposit $LiCoO_2$ or $LiMn_2O_4$ composite electrodes. The solution was a suspension of active material particles, ketjen black and polytetrafluoroethylene in acetone. A small amount of iodine was used as a charge producer. A high DC voltage was applied to the suspension solution to create an electric field (100 V/cm for $LiCoO_2$ and 400 V/cm for $LiMn_2O_4$), which caused the charged particles to move and deposit onto substrates. The active material loadings were controlled at 10 mg/cm^2. The published data showed 0.5 C-rate discharge capacities of the $LiCoO_2$ and $LiMn_2O_4$ as 140 and 110 mAh/g (Kanamura et al. 2000), respectively, which were comparable to the electrodes fabricated in laminated processes. The power capabilities of these electrodes were unclear from the above paper.

2.4.3 SEALING

Sealing liquid on silicon-based micro devices is problematic (Humble 2002). However, liquid electrolytes may be desired in the proposed microbattery to achieve high power

performance. Therefore, it is essential to implement liquid sealing with some techniques that will be compatible to the microbattery fabrication.

Polymer substrate seems to be a promising solution. In recent years polymer-based electronics have attracted much attention (Fix et al. 2002, Drury et al. 1998, Gelinck et al. 2000, Chen 2002). Based on their low cost, physical flexibility, solubility, sufficiently high dielectric constant, polymer materials have been investigated as the substrate and functional materials for low-cost and low-end IC devices.

These polymer-based electronics generally used standard IC techniques, with necessary modifications to address the properties of polymer materials. For example, in the all polymer ICs developed by Drury et al. 1998, the conducting pattern was created by deep ultraviolet radiation of doped polyaniline (PAN) conducting films. Upon exposure, the conducting polyaniline is reduced to the nonconducting leucoemeraldine form, with corresponding sheet resistance increases from 1 kΩ/square to more than 10^{14} Ω/square. As a result, conducting tracks are embedded in an otherwise insulating matrix. No chemical etching was involved and no planarization steps were required; hence the cost was greatly reduced. The conducting PAN Transistors with channel lengths down to 1 μm have been fabricated.

One unique process used in the polymer IC fabrication is ultrasonic bonding (welding) (Devine 2001). This process uses ultrasonic vibrational energy to cause the plastic at the joining interface of the plastic parts to soften and create a bond. It can be used to bond metal and thermoplastic materials, to join plastic parts, to degate plastic parts and to cut and seal films. Heating is confined to the interface area so the other parts of the plastic are not exposed to extensive heating. This feature makes ultrasonic bonding an attractive sealing technique for a microbattery containing liquid electrolyte and using thermoplastic as substrates.

In a summary, various techniques have been applied to fabricate thin-film and composite electrodes. Sputtering, pulsed laser deposition, spin coating and similar techniques are unlikely to produce films to the thickness desired in this study (~100 μm), and will not be adopted as electrode film fabrication method. In contrast, composite film coating techniques, especially screen printing, can produce the electrode film of the desired thickness. Furthermore, screen printing produces patterned films with composite slurry similar to those used in composite electrode laminations. These features of screen printing make it an attractive method to prepare the electrode films for the proposed microbattery. Polymer substrate and ultrasonic bonding seem to provide a feasible method to seal liquid electrolyte in microbatteries.

2.5 SUMMARY

Based on performance comparisons between the two types of electrode structures, the composite electrode is preferred as the electrode structure for the proposed high power microbattery. However, performance and fabrication issues remain as obstacles to the implementation of the composite microbattery.

Large size composite batteries use CB or similar graphite materials as conductive additives, and require compression to achieve optimal performance; composite electrodes using fibrous conductive additives show better performance than those using CB particles. It is thought that fibrous conductive materials will construct a better conductive network, which can reduce or eliminate the pressure dependence of the electrode performance.

A fabrication route is needed to build composite microbatteries. Screen printing appears to be a relatively simple technique that is capable of producing thick composite films for the

proposed microbattery. Polymer IC techniques seem to be a good candidate for sealing liquid electrolyte in the microbattery.

The primary objective of this study was to develop a high power lithium-ion microbattery suitable for use in a hybrid power system for remote sensor applications. Such a task should be achieved based on an understanding of factors that limit power in composite batteries, and the development of strategies to overcome those limitations and improve power performance. The development of this understanding and the corresponding strategies was the second objective of this study. The third objective was to develop a feasible fabrication route, using microfabrication techniques, to produce microbatteries with the desired performance characteristics. Achieving these objectives would create a high power lithium-ion composite microbattery needed for practical applications, contribute to the fundamental understanding of electrode processes, and develop a new method of microbattery fabrication.

CHAPTER 3: EXPERIMENTAL APPARATUS AND PROCEDURE

The electrodes and batteries in this study can be divided into two groups according to their size. The "large" or "macro" electrodes refer to those with an effective area of c.a. 2 cm x 2 cm, and "micro" electrodes refer to those with sub-cm^2 area (the target area of micro electrodes being no greater than 0.1 cm^2). The latter was the immediate subject of this study, and the former was used to seek an optimal composition and structure of electrodes to achieve the power performance desired in micro-sized batteries.

Therefore, the first part of this chapter describes the experimental equipment and procedures used to fabricate large composite electrodes and batteries. The second part describes applicable integrated circuit (IC) microfabrication equipment and procedures; microbattery fabrication will be detailed in the Results chapter as it represents a part of the experimental results of this study. The last part of this chapter describes the electrochemical and other testing equipment used in this study.

3.1 LARGE ELECTRODE AND BATTERY FABRICATION

Large electrodes were fabricated at room temperature and pressure (22 °C and 640 mmHg, respectively), unless otherwise specified. Most large composite electrodes in this study contain active material, polymer binder, and conductive fillers. The cathodes were named after the amount and the type of conductive fillers in the electrodes, as these were two important variables of interest. For example, the cathodes containing 12 wt% CB were labeled as 12 wt% CB-cathodes

and the cathodes containing 7 wt% single-walled carbon nanotubes were labeled as 7 wt% CNT-cathodes. Both the type and the amount of electrode materials used in this study are listed in Table 3.1:

Table 3.1 Electrode materials and contents

Component	Cathode		Anode	
	Material	wt%	Material	wt%
Active Material	$LiAl_{0.14}Mn_{1.86}O_4$	70-97.4	MCMB	90
Polymer Binder	PVDF	2.6-15	PVDF	5
Conductive filler	CB	0-15	Super P	5
	SWNT	0-15		

Sources:

$LiAl_{0.14}Mn_{1.86}O_4$: Noddapaneni and Ingersoll (1996)
PVDF: poly (vinylidene fluoride) 741 Kynar Corp.
CB: XC-72R carbon black, Cabot Corp
SWNT: single-walled carbon nanotubes, Carbolex AP-grade.
MCMB: synthetic graphite, grade 628, Osaka Gas Chemical Co., Japan
Super P carbon black: MMM N. V., Belgium

3.1.1 COMPOSITE ELECTRODE FABRICATION

Active material for composite cathodes, Al-doped lithium manganese oxide ($LiAl_{0.14}Mn_{1.86}O_4$), was dried at 300 °C under vacuum for 8 hours and then manually sieved using a 400 mesh sieve (38 μm opening) to remove the particles larger than 38 μm in diameter that might promote shorting. Other materials were used as received.

A coulter counter particle size analyzer (Beckman Coulter, California) was used to determine the particle size distribution (PSD) of the cathode active materials. Two different batches of active materials were received and used before and since January 2002, and a significant difference existed between the two PSD's as shown in Fig 3.1. The first batch had two prominent peaks in the PSD curve at about 2.22 μm and 12.4 μm, respectively; the second batch had only one prominent peak in its PSD curve at about 3.07 μm.

The electrode fabrication began by first dissolving PVDF powder in *n*-methyl pyrrolidone solvent (NMP, 99+ % ACS, Aldrich) at 60 °C to make a polymer binder solution. The conductive filler and active material were mixed by a spatula manually, and then poured into the binder solution. This mixture was stirred vigorously with a spatula and then by an ultrasonic probe (4710 series, Ultrasonics Homogenizer, Cole Palmer Instrument Co., Chicago, IL) to form a uniform composite slurry. The composite slurry was then spread onto a smooth current collector (aluminum foil for cathodes and Cu foil for anodes; both from Alfa Aesar, 25 μm thick, 99.45 % and 99.8 %, metal basis, respectively). A casting blade (BYK-Gardner USA, Columbia, MD) was used to control thickness of the composite film. It was drawn multiple times across the slurry until a uniform film had formed at a designated film thickness (Fig. 3.2). The composite film was dried overnight in a vacuum oven (Napco 5851) at 100 °C to remove the solvent.

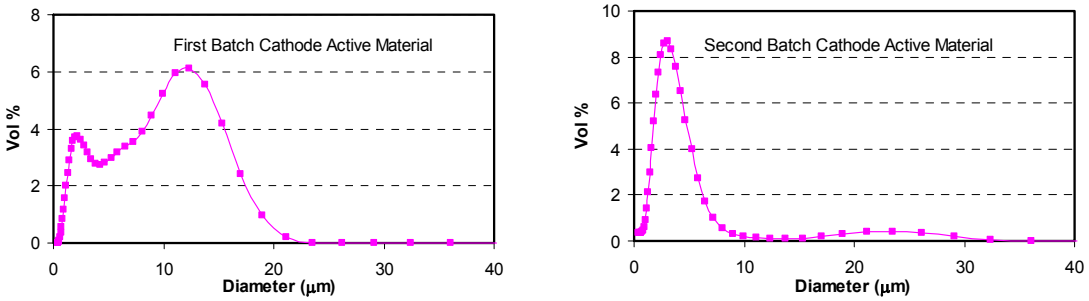

Figure 3.1 Particle size distributions for the cathode active material

After drying, individual cathodes were cut from the dried film using a template. The template for composite electrodes is shown in Fig. 3.3, which is a c.a. 2.0 cm x 2.0 cm square (the effective electrode area) with a stem of 0.5 cm x 3.0 cm (for electrical connections). The individual electrodes cut from the composite film were completely covered with composite material on the square area; in this process, the stems were partially covered with the composite, which was

carefully removed with a razor blade. Photographs of a composite cathode and a composite anode are shown in Fig. 3.4.

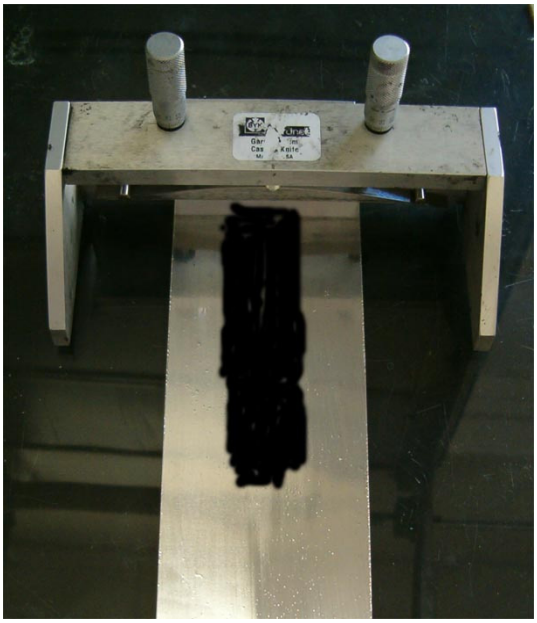

Figure 3.2 Composite film making with a casting blade

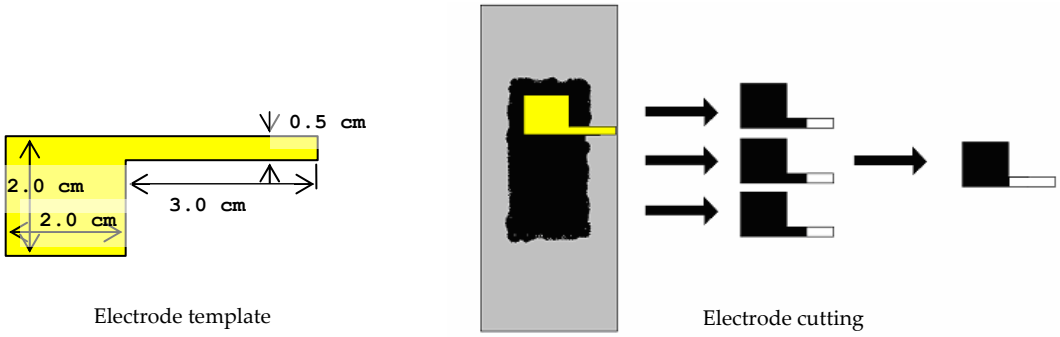

Figure 3.3 Electrode template and individual electrodes cut from the dried composite film

After drying, individual cathodes were cut from the dried film using a template. The template for composite electrodes is shown in Fig. 3.3, which is a c.a. 2.0 cm x 2.0 cm square (the effective electrode area) with a stem of 0.5 cm x 3.0 cm (for electrical connections). The individual

electrodes cut from the composite film were completely covered with composite material on the square area; in this process, the stems were partially covered with the composite, which was carefully removed with a razor blade. Photographs of a composite cathode and a composite anode are shown in Fig. 3.4.

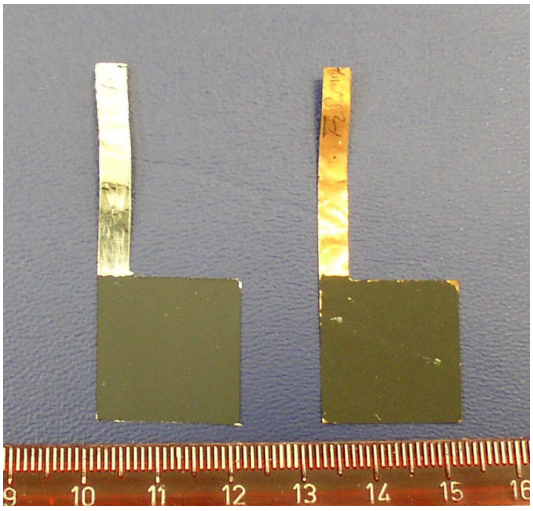

Figure 3.4 Individual large composite electrodes (cathode: left; anode: right)

3.1.2 LITHIUM METAL ELECTRODES

Lithium metal electrodes were used as counter electrodes in half-cell tests of composite electrodes to investigate the performance of the composite electrodes. The lithium was stored and used in an argon filled glovebox (H_2O < 1 ppm, O_2 < 1 ppm; He-243-2 or OMNI-LAB, Vacuum Atmospheres Corp., CA) to prevent degradation due to exposure to moisture and oxygen.

The current collector for the lithium electrode was Cu foil, cut into shapes similar to the composite electrodes, except that the size of the squares was c.a. 2.2 cm x 2.2 cm (slightly larger than that of composite electrodes). These current collectors were cut outside the glovebox for convenience. Lithium ribbon (99.8% metal basis, 0.38 mm thick x 2.5 cm wide, Johnson Matthey

Co.) was cut into squares of 2.2 cm x 2.2 cm. A piece of lithium square was stacked on top of a piece of current collector, and the stack was then placed between two steel plates and pressed with a hydraulic jack (B008NC, Prolift). Note that polypropylene films were used to separate the lithium electrode stack from the steel plates to prevent metallic contamination of the electrodes (Fig. 3.5).

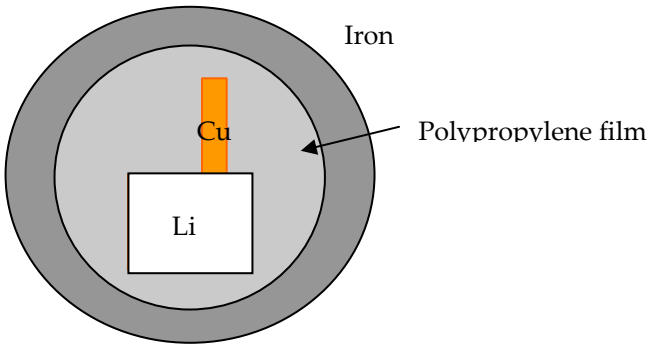

Figure 3.5 Making a lithium electrode

3.1.3 CELL ASSEMBLY

All the cells in this study were assembled in the glovebox. The composite electrodes were prepared following the procedure outlined in Section 3.1.1 and measurements were taken on their thickness and mass. Porous polypropylene separator films (Celgard® 2400 or 2325, Celgard LLC., North Carolina) were cut into c.a. 2.5 cm x 2.5 cm squares. Heat sealable polymer films (Class PPD Shield Pack Inc., CA) were cut into 10 cm x 6 cm rectangular shapes. All of these preparations took place outside the glovebox and the materials were transferred into the glovebox for assembly.

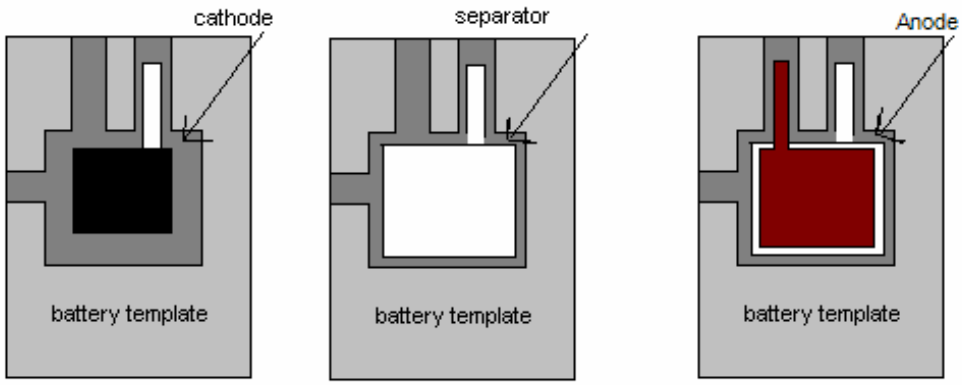

Figure 3.6 Assembling a cell (a lithium-ion cell shown)

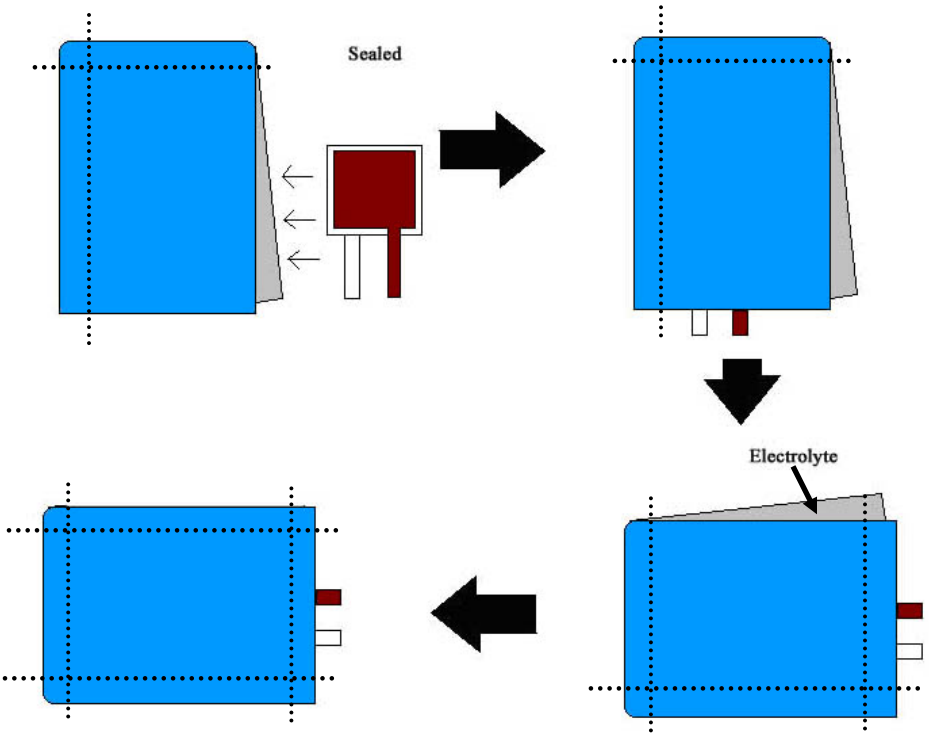

Figure 3.7 Sealing a cell

A template was used in the assembly procedure to align the electrodes and separator paper (Fig. 3.6). The first electrode was placed in the template, with the composite film facing up; pre-cut separator films were placed in the template, covering the first electrode; then the second electrode was placed on the separator, with the electrode side facing toward the first electrode (Fig. 3.6). The cell sandwich was placed into a rectangular pouch (Fig. 3.7), which consisted of

two pieces of heat sealable polymer films with two adjacent sides were already sealed with an electric heat sealer (Impulse Sealer Tish 200, Electronic Heating Equipment Co.). Both electrode stems extended from the same side of the package, which was then sealed with the heat sealer. About 1.0 ml of 1.0 M $LiPF_6$ /(EC:DEC) electrolyte (LithDyne Elyte, LithChem International, California) was added into the pouch, and then the last side of the pouch was sealed. By this point the cell was completely sealed and was taken out of the glovebox for electrochemical tests.

3.2 MICROFABRICATION EQUIPMENT AND PROCEDURES

Microfabrication was selected for fabrication of thick-film microbatteries, based on its potential advantage over traditional techniques to improve cell volume usage and energy density, and allow better integration with micropower systems. High volume and low unit cost of microfabrication were among other considerations as well. A variety of equipment and processes are available at the Integrated Microfabrication Lab (IML) at BYU. The equipment used and established procedures are described in this section; the procedures developed in this study will be described in the Results chapter.

3.2.1 EVAPORATION FILM COATING

An Electron-Beam evaporator and a thermal evaporator (Fig. 3.8) were used in this study to coat Al or Cu thin films on substrates as electrode current collectors for the microbattery. In both evaporators the materials to be coated are heated with E-beam or thermal energy in order to evaporate and coat on the target substrates.

Before coating, the chambers of these evaporators are evacuated to a pressure in a range of 10^{-5} to 10^{-8} Torr to ensure the mean free paths of the evaporated atoms are greater than the

distance between the source material and the target substrates. In both evaporators the source materials can be switched without opening the chamber; therefore, one to three layers of different materials can be deposited sequentially on the substrates in a single run. Both evaporators are equipped with a quartz crystal monitor for the measurement of the film thickness and deposition rate. The typical deposition rate was ~1 nm/s, and the thickness of the Al and Cu films was about 500 nm. Detailed operating procedures can be found on the IML website (http://www.ece.byu.edu/cleanroom).

Figure 3.8 The E-beam evaporator (left) and thermal evaporator (right)

3.2.2 SPIN COATING

A Solitec spinner was used in this study to coat a layer of photoresist (PR) onto substrates; then the PR layer will be processed in photolithography to create desired patterns. This spin coater supports substrates of up to 9" in diameter, with rotation speed up to 6000 rpm. The following procedure was used to perform the spin coating process:

a) Mount the substrate on the chuck of the spinner;

b) Apply a puddle (~5 mm in diameter) of resist to the center of the substrate;

c) Turn the speed knob quickly to a desired speed and let the substrate spin for about 1 minute, or until a uniform film is formed;

d) Turn down the speed knob to stop the spinning;

e) Unload the substrate.

3.2.3 PHOTOLITHOGRAPHY

Photolithography was used in this study to transfer the desired patterns from a mask to the substrates. A complete photolithography process included spin-coating PR, exposure, developing and etching. The spin-coating process was described in the previous section, and the other three processes are described in this section.

The positive photoresists used in this study included Shipley 1.8M (Shipley L.L.C., MA), AZ 3312 and AZ 3330 (Clariant Corporation, NJ). These photoresists were used as temporary layers for transferring patterns and did not remain in the electrodes or batteries. Both photoresists were spun as 1-2 μm thick layers on the substrate, and were capable of a line width at least as small as 1 μm.

The negative PR used in this study was the SU-8 25 photosensitive epoxy (MicroChem Inc., Newton, MA). The SU-8 PR was generally spin-coated with a thickness of 25-50 μm. Since it has good chemical resistance after being cured, the SU-8 PR layer was generally used as a permanent structure in microelectronics.

A parallel light mask aligner (PLA-501F, Canon. See Fig. 3.9) was used to expose the PR in this study. This machine allows for the use of 4-5 inch photomasks and can handle 2-5 inch wafers. It is equipped with an auto feeder, allowing hands-off loading and unloading of the

wafer. Both automatic loading and manual loading were used, and the operating procedure can be found on the IML website (http://www.ee.byu.edu/cleanroom). Note that the Canon aligner is equipped with a time counter, which can automatically control the exposure time in the range of 0.1 – 59 seconds. When a longer exposure time was needed (for example, some SU-8 PR films needed an exposure time of 2 mins), a manual exposure mode was used and the exposure duration was monitored with a watch.

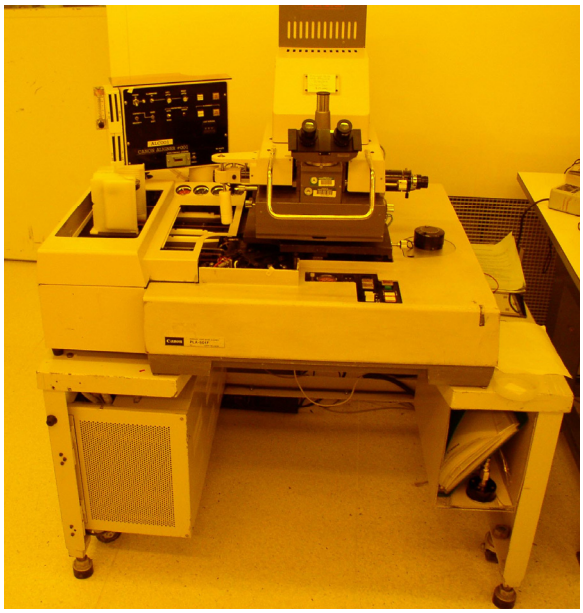

Figure 3.9 Canon aligner

Following the exposure, the substrates went through necessary treatments (for example, post-bake for SU-8 PR) and the PR films were developed in proper solutions. The Shipley resist and AZ resists use Shipley MF-26A and AZ300MIF developer solutions, respectively. The developer for the SU-8 PR was MicroChem's SU-8 developer solution.

After being developed, the positive PR coated substrates were etched to transfer the patterns from the PR to the underneath film, and then the PR layers were removed from the

substrates. The developed SU-8 film, on the other hand, was baked and cured as a structure on the substrate. Detailed information on developing and etching can be found on the IML website.

3.2.4 REACTIVE ION ETCHER

The reactive ion etcher in the IML, Anelva RIE (DEM-451Anelva Corporation), is a parallel plate, 13.56 MHz system used for etching with tetrafluoromethane (CF_4) (Fig. 3.10). The system was used in this study primarily for etching of Si_3N_4 and polymer films. The system generally produces anisotropic etch profiles (straight sidewalls). The specifications and operating procedures can be found on the IML website (http://www.ee.byu.edu/cleanroom).

Figure 3.10 Reactive ion etcher

3.2.5 SCREEN PRINTING

Screen printing was used in this study to coat composite films for micro-sized electrodes. In this process, a mask was first placed on the substrate and a composite paste (made following the procedure outlined in Section 3.1.1) was dispensed on the surface of a mask, close to the

openings. A blade was then drawn across the mask, forcing the paste into the opening (Figure 3.11). Finally, the blade and the mask were removed, leaving the patterned paste on the substrate. The paste was then allowed to settle for about one hour before being dried in a vacuum oven.

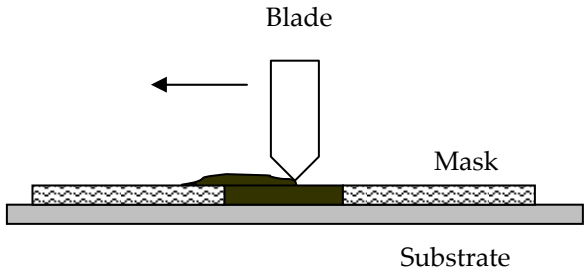

Figure 3.11 A blade drawn across the mask during screen printing (redrawn from Madou 1997)

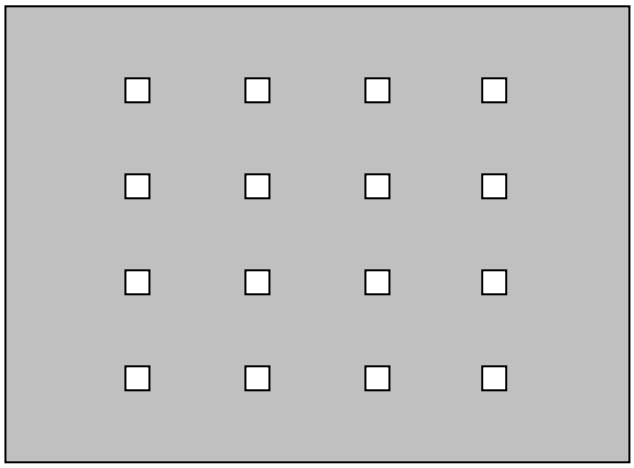

Figure 3.12 A screen printing mask (the dimension of the openings is c.a. 2 x 2 mm^2)

The thickness of the mask was an important factor to the thickness of the dry composite film. Masks of various thicknesses were used in this study. For example, a 200 μm thick mask

was used to create a composite film of about 80 μm thick. A mask with 2 x 2 mm^2 openings is shown in Fig. 3.12.

3.3 TESTING EQUIPMENT AND PROCEDURES

The thickness of dried composite films on the current collectors was measured using an electronic digital micrometer (Chicago Brand Industrial Inc., Fremont, CA). The mass of each composite electrode was measured by an electronic balance (Sartorius GMBH Gottingen, Germany), and the mass of the composite material was obtained by subtracting the mass of the current collector. The theoretical capacity of the electrode was then estimated based on the amount of active material and its capacity.

The large cells were generally tested outside the glovebox since packaging polymer films can provide adequate protection against moisture and oxygen. Cells not sealed or not sufficiently sealed, including most microbatteries, were tested inside the glovebox. For the large cells tested with compression, aluminum holders were used to provide uniform pressure, with bolts torqued to 20 inch-lb (Fig. 3.13).

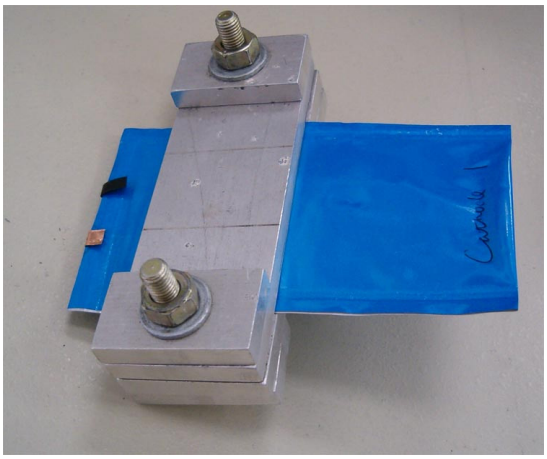

Figure 3.13 A large cell compressed in an aluminum holder

All cells were tested using an Arbin BT2043 battery cycler controlled with Mits'97 software (Arbin, College Station, Texas). The battery tester has an input impedance of 10 GΩ for -12 to 12 V, an accuracy of 0.1 % of full range, a repeatability of 0.02 % of full range, a resolution of 0.0015 % of full range, and a maximum pulse frequency of 400 Hz. The tester has eight independent channels, grouped into odd number channels and even number channels. The odd number channels (channel 1, 3, 5 and 7) are dedicated high current channels, with low current range of (-5 mA, 5 mA), mid current range of (-500 mA, 500 mA) and high current range of (-5 A, 5 A). The even number channels (channel 2, 4, 6 and 8) are dedicated low current channels, with low current range of (-20 μA, 20 μA), mid current range of (-200 μA, 200 μA) and high current range of (-10 mA, 10 mA). The primary testing voltage range of all channels is (-5 V, 10 V).

This study uses "C rate" or "C-rate" to define the amount of current. This a commonly adopted way to normalizing currents among cells of different capacities. 1 C rate corresponds to a current at which a fully charged cell will be completely discharged in 1 hour. An example of Mits'97 test schedule file is included in Appendix A. The general testing procedure for cells is listed as follows, with the voltage limits listed in Table 3.2:

1) Charge at a 0.5 C rate to a preset voltage limit V_1;
2) Taper-charge at V_1 until current reduces to a 0.2 C rate;
3) Let the cell rest for 5 seconds;
4) Discharge at 0.1 C rate for 20 seconds, then perform 5 pulse discharge cycles to determine the overall internal resistance;
5) Discharge at a designated C rate until the voltage reaches a preset limit of V_2;
6) Repeat from step 1 to step 5 for additional cycles.

Note that in the above procedure a taper charging technique was used to charge a cell to its maximum capacity at a designated constant voltage. In the taper charging process, the tester

applies a current to the cell, and measures its voltage response; the magnitude of the current is then adjusted to maintain the cell voltage at the designated value; this adjusting process is continued until the current reduces to a preset lower limit.

Table 3.2 Voltage limits of different cell testing

	V_1 (Vol)	V_2 (Vol)
Cathode	4.3	3.3
Anode	0.05	1.5
Composite	4.1	2.8

Step 4 in the above procedure used a pulse discharge technique to determine the internal resistance of the cell. For the macro-sized cells the current was set at 10 μA for 100 ms and then at 20 μA for 10 ms; the cell voltages were measured at both current densities and the internal resistance was estimated as $\Delta V/\Delta I$. For cells with smaller electrodes lower current densities were used.

CHAPTER 4: DEVELOPMENT OF A HIGH POWER THICK-FILM CATHODE

As discussed in Chapter 2, this study focused on improving the performance of composite cathodes to achieve a high power lithium-ion microbattery. Large size electrodes were used to develop a high power composite cathode, and the results are presented in this chapter. First, the power performance of CB-cathodes was examined, which did not meet the requirements for the proposed microbattery. Then SWNT was investigated as the conductive additive in uncompressed cathodes. The SWNT-cathodes showed significant improvement in the desired performance aspects, and the optimized cathodes showed a power capability exceeding the microbatteries requirement.

4.1 CB-CATHODES

Mandal et al. (2001) and Lazarraga et al. (2003) showed that the low-rate discharge capacity of $LiMn_2O_4$ cathodes depended strongly on the carbon black content, and a CB volume fraction greater than 10-15% was required to ensure the delivery of a high percentage of theoretical capacity. Note that those tests were carried out on compressed cathodes, and the results reflected the effect of compression. It should be also noted that high rate discharge tests were not performed in these studies.

In this study, the composite cathodes were fabricated following the procedures listed in Chapter 3, and contained 90 wt% $LiAl_{0.14}Mn_{1.86}O_4$, 2.5 wt% PVdF, and 7.5 wt% CB. The electrodes

had an area of c.a. 4 cm^2, a film thickness of 40-50 μm (before being compressed) and theoretical capacity of 0.4-0.5 mAh/cm^2. These CB-cathodes were tested against Li metal anodes.

The compressed CB-cathodes showed good cycling performance. As shown in Fig. 4.1, a compressed 7 wt% CB-cathode had a capacity fade rate of only 0.07 %/cycle, which was higher but still comparable to the fade rate of 0.04 %/cycle reported in Linden and Reddy (2001) (cycled at 23 °C at the C/2 rate between 4.3 and 3.5 V). The symbols and line in the plot represent charge and discharge capacities, respectively. Similar legend usage is followed in cycling plots in this dissertation, unless otherwise stated.

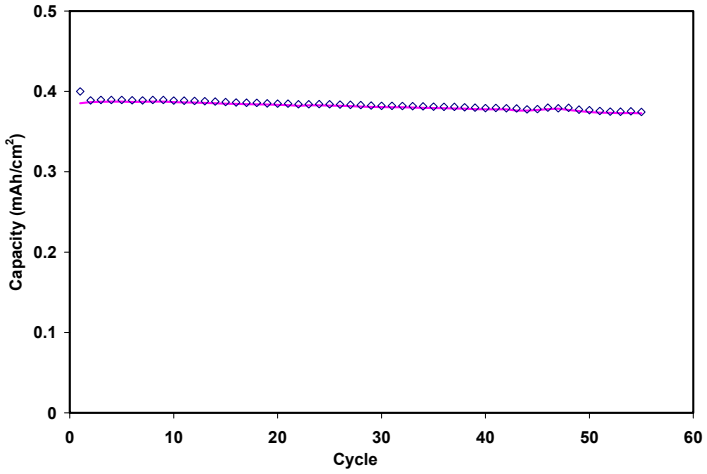

Figure 4.1 0.5 C rate cycling performance of a compressed 7 wt% CB-cathode (symbols: charge capacity; line: discharge capacity)

The power performance of a compressed CB-cathode is shown in Fig. 4.2. This cathode delivered significant fractions of its theoretical capacity (which was about 0.50 mAh/cm^2 as indicated by the 0.1 C discharge capacity) at 0.5 C and 3.0 C rates; the fraction dropped to about 13 % at a 10 C rate. As the data indicated, these compressed CB-cathodes could not provide sufficient power to the proposed microbattery. For example, the 10 C rate in Fig. 4.2

corresponded to a power density of ~16.5 mW/cm² (with capacity of only 0.065 mAh/cm² delivered), which was only about 30 % of that required by the proposed microbattery.

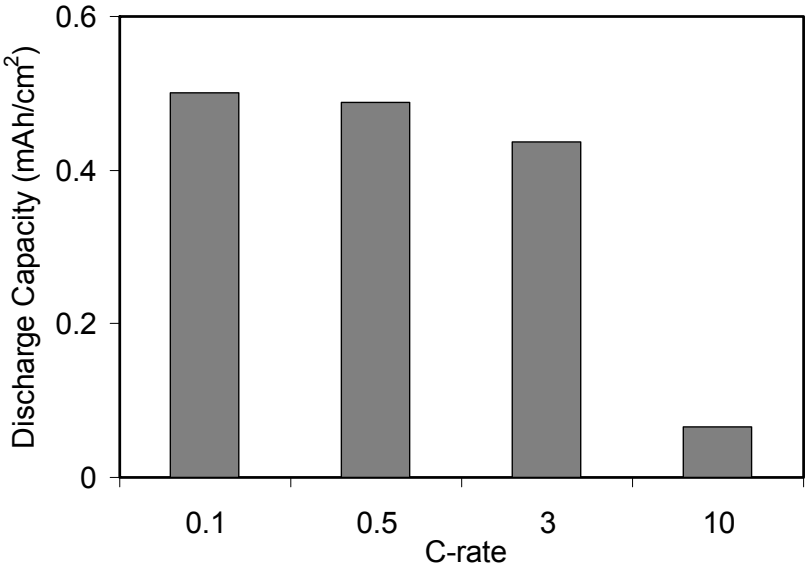

Figure 4.2 Discharge capacities of a compressed 7 wt% CB-cathode at different rates

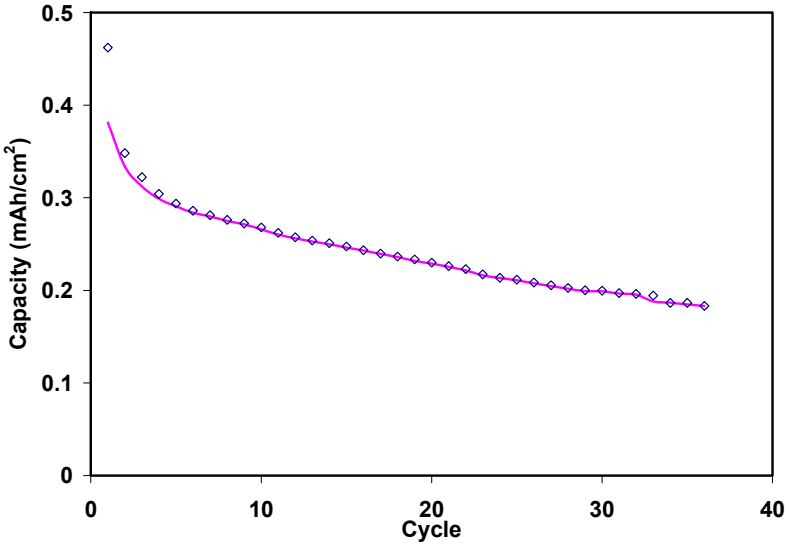

Figure 4.3 0.5 C rate cycling performance of an uncompressed 7 wt% CB-cathode (symbols: charge capacity; line: discharge capacity)

As discussed previously, it was desired to avoid compression for the proposed high power microbattery in this study. Therefore, the cycling and power performance of the uncompressed CB-cathodes was investigated. The cycling performance of an uncompressed CB-cathode at a 0.5 C-rate is shown in Fig. 4.3. It can be clearly seen that the uncompressed CB-cathode had a high capacity fade rate, with less than 50 % of the starting capacity delivered at cycle 35. Obviously such a cycling performance would not be acceptable for the proposed microbattery.

Higher rate discharge tests were also performed on these uncompressed CB-cathodes, as shown in Fig. 4.4. It was found that this cathode delivered about 0.50 mAh/cm^2 at a 0.1 C rate, and only ~0.02 mAh/cm^2 at a 1.5 C rate (which corresponded to a power density less than 2.5 mW/cm^2). Such a poor power performance was obviously far from sufficient for the proposed microbattery.

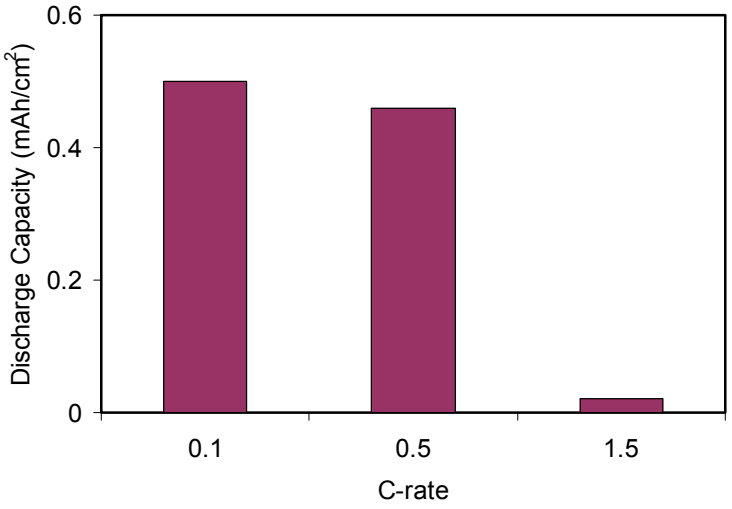

Figure 4.4 Discharge capacities of an uncompressed 7 wt% CB-cathode at different rates

Internal resistance is a sum of resistances in a cell that inhibits the electron and ion transport and causes potential drop. In this study, the internal resistance was measured with a pulse discharge technique as described in Chapter 3. The result in Fig. 4.5 shows a strong impact of

compression to the internal resistance of the CB-cathodes. The internal resistance of the compressed cathodes was significantly lower than that of the uncompressed counterparts, with the difference frequently being an order of magnitude or higher. From the differences in performance due to compression, it was concluded that e compression reduced the internal resistance and improved the cycling and power performance of the CB-cathodes. Figure 4.5 also shows the impact of CB content to the internal resistance. It can be seen that without the CB additive the cathodes had a very high internal resistance; with additional carbon black, the internal resistance of the composite cathodes decreased 1-3 orders of magnitude depending on CB content.

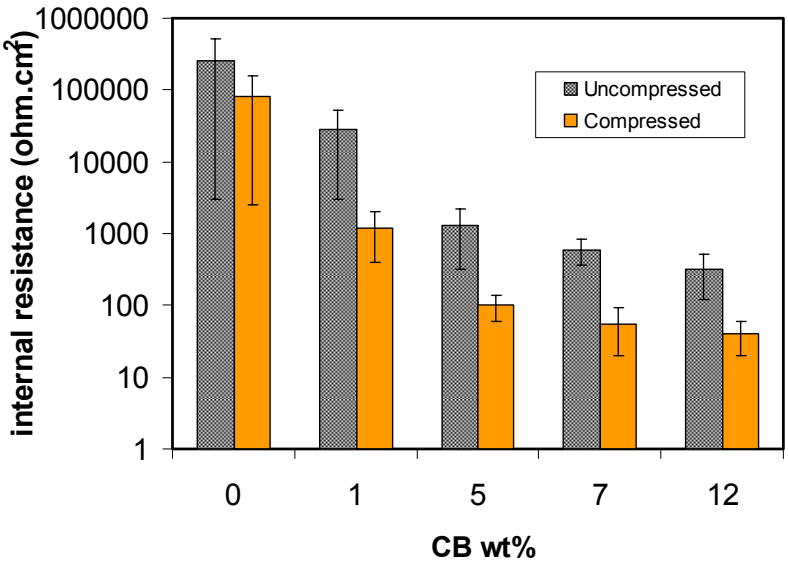

Figure 4.5 The internal resistances of CB-cathodes (~40 μm thick) for various CB loadings

The electrical resistance was measured between the current collector and Al foil attached on the composite films (which was applied before the films were dried). The film resistivities were calculated by normalizing the measured resistance with contact area and film thickness. Fig. 4.6 shows that the film electrical resistivity decreased with increasing CB content, which is consistent

with the observation of electrical resistivities made by Lazarragaa et al. (2003). Without the CB additive the electrical resistance of cathodes is dominated by the highly resistive active material. As the electrical conductivity of carbon black is about 5 orders of magnitude higher than that of the active material, the electrical resistance of the cathodes with carbon black would be generally determined by the conductivity and content of carbon black. Fig. 4.6 shows that the change in the film electrical resistivity relative to CB content was very similar to that of the internal resistance shown in Fig. 4.5. This observation indicated that the resistance of these CB-cathodes was dominated by electrical resistance. As a similar impact of compression is seen on both film electrical resistivity and internal resistance, it was concluded that compression reduced the internal resistance by decreasing the electrical resistance in the CB-cathode.

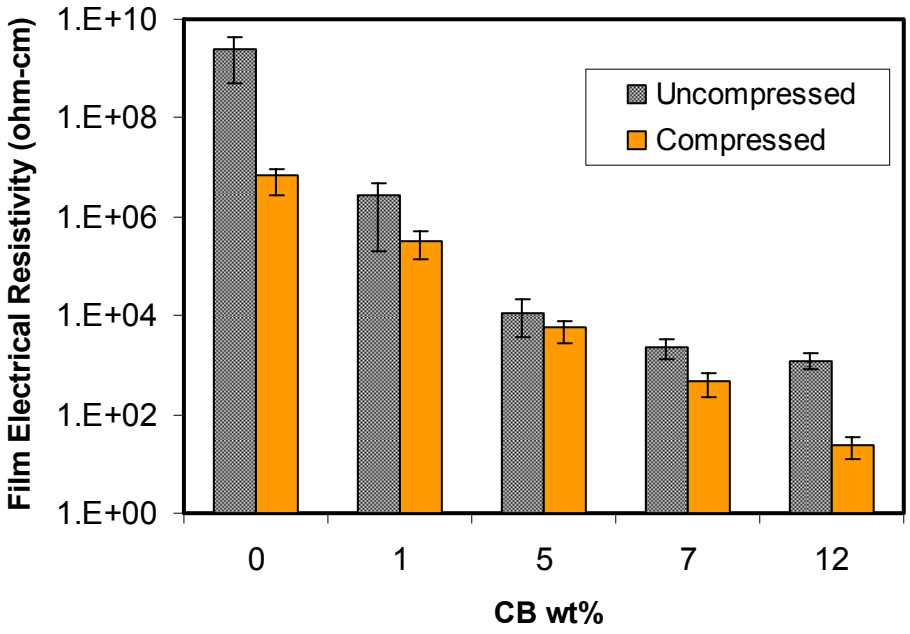

Figure 4.6 The film electrical resistivity of CB-cathodes

The above experiments verified that the compression plays a significant role in the CB-cathodes, without which the performance of these cathodes is highly compromised. Since applying compression to the microbattery significantly complicates the fabrication, CB-cathodes are not the ideal choice for the proposed microbattery, particularly because the uncompressed CB-cathodes would not meet the cycling and power requirements of the proposed microbattery. Therefore, a cathode with better cycling and power performance was sought.

4.2 CNT-CATHODES

Carbon nanotubes (CNTs) were discovered in 1991 by S. Iijima (1991). There are two types of CNTs, single walled carbon nanotubes (SWNTs or SWCNTs) and multi-walled carbon nanotubes (MWNTs), which can be viewed as a carbon sheet of a hexagonal lattice rolled into a hollow cylinder and concentric graphite cylinders, respectively. The unique morphology and electrical conductivity of SWNTs are of special interest to this study. SWNTs have average diameter of 1.2-1.4 nm (Spires and Brown 1996), with typical length of a few μms. As grown SWNTs are mixtures of metallic and semiconductive tubes, and the conductivity of a naturally grouped bundle of SWNTs was measured to be ~10^4 S/cm (Thess et al. 1996).

The ultra-high aspect ratio and the outstanding electrical conductivity of SWNTs should make the electron conduction along a carbon nanotube superior to that along an equivalent path of CB particles, which consists of numerous contacts between different particles. The improved electron conduction of SWNTs should not depend on electrode compression as much as CB particles, and should have a significant impact on the power performance of the composite cathode. The latter point was supported by Sakamoto and Dunn (2002), who showed that using SWNTs instead of CB particles increased the active material accessibility at high rates. Therefore,

SWNTs appeared to be a good candidate for a conductive additive to obtain a high-power cathode that would be suitable for the proposed microbattery.

In this chapter CNT-cathode performance, including cycling tests and power tests, are reported. Fabrication parameters, including the CNT mass fraction and the electrode thickness, were optimized to maximize the power performance of the CNT-cathodes. The performance of the CNT-cathodes was evaluated for the proposed microbattery and found to exceed the requirements.

4.2.1 MORPHOLOGY AND MICROSTRUCTURE

The SWNTs tested in the composite cathodes were "as prepared" grade SWNTs from Carbox Inc. (Broomall, PA). According to the manufacturer's data, these SWNTs have an average diameter of 1.4 nm and length of 2-3 μm, are generally found in "ropes" of about 50 tubes which are typically ~20 nm in diameter and 2-5 microns in length. The volume fraction of SWNTs was about 50-70 %. Impurities include approximately 35 wt% residual catalyst (Ni, Y) which is usually encapsulated in carbon shells. Some amorphous carbon may be present on the outer surfaces of the ropes.

The composite $LiAl_{0.14}Mn_{1.86}O_4$ cathodes using SWNTs as the conductive additive were fabricated following the procedure listed in Chapter 3. They were then assembled with Li counter electrodes and tested. These CNT-cathodes visually appeared the same as CB-cathodes to the naked eye. However, surface SEM (scanning electron microscope) images revealed a distinct difference between the microstructures of these two types of composite cathodes. As shown in Fig. 4.7, the image of the CNT cathode showed needle-like structures associated with the SWNTs, which are the "ropes" of SWNT bundles that were not present in the CB cathode.

These structures are believed to contribute to the establishment of electrical contact through the electrode.

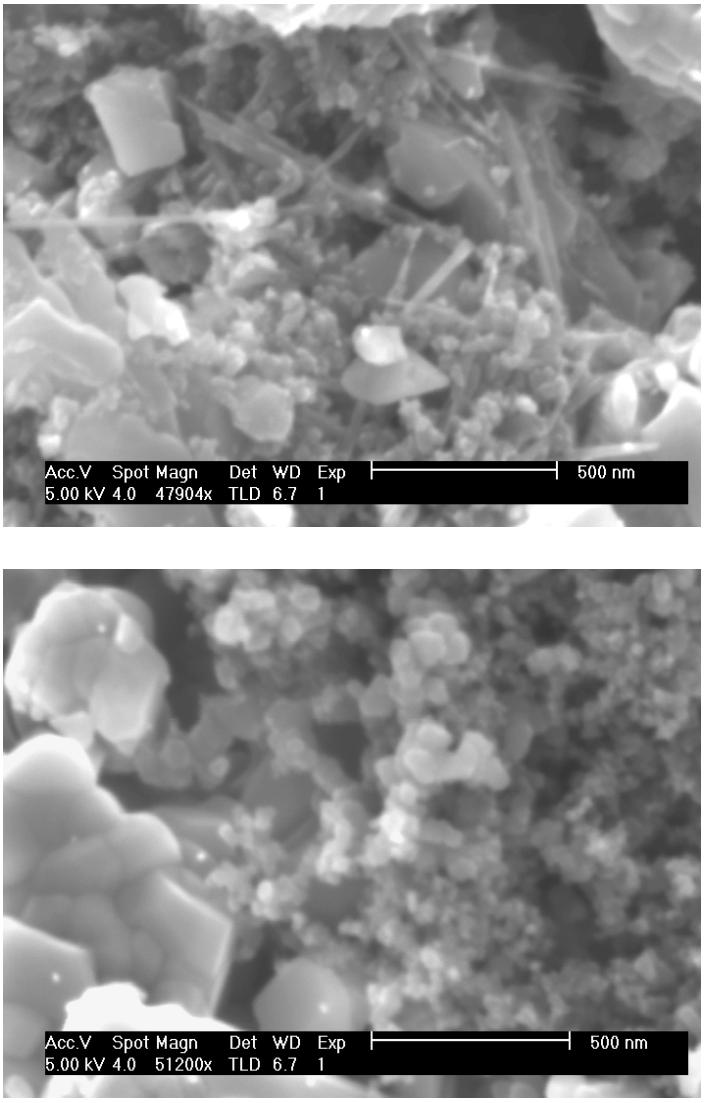

Figure 4.7 SEM images of a CNT-cathode (top) and a CB-cathode (bottom)

An experiment was performed to examine the contribution of CNTs and any impurities associated with the nanotubes to the electrochemical capacity of the CNT-cathodes. The electrodes were fabricated with SWNT, polymer binder, and no active material, and tested against Li electrode in the same voltage range as the CNT-cathodes containing active materials.

The capacity was found to be less than 1.5 % of the capacity of a CNT-cathode containing active materials. For comparison, the CB contributed to about 1.1 % of the capacity of a CB-cathode. Therefore, it was concluded that the involvement of CNTs in the electrochemical reaction was negligible. The primary function CNTs in the cathodes was most likely increasing electronic access to the active material.

The internal resistances of CNT- and CB-cathodes are shown in Fig. 4.8, which is a summary of data from cathodes with 7 wt% conductive additive. It is once again evident that compression dramatically reduced the internal resistance in CB-cathodes, which was expected as the compression enhanced the contacts between CB particles. It is also evident that uncompressed CNT-cathodes had a significantly lower internal resistance than the compressed CB-cathodes. CNT-cathodes containing the same weight fraction of conductive filler had an internal resistance that was approximately one-sixth of that of the compressed CB-cathodes with the same carbon weight fraction. The lower resistance of the CNT-cathodes is expected to improve the cathode performance, especially at high discharge rates.

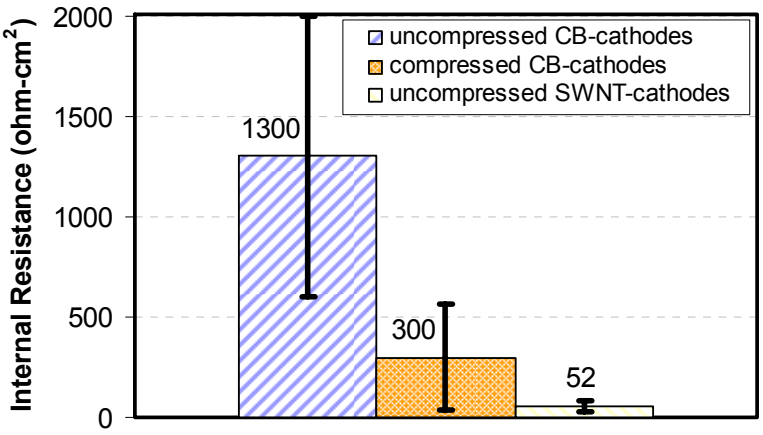

Figure 4.8 Comparison of the measured internal resistances of CB-cathodes and CNT-cathodes

In order to understand the source of the large difference between the measured resistances of the CNT and CB cathodes, it is useful to examine the differences in the conduction paths formed by CB particles and SWNTs additives. To be useful, a conductive additive must provide a conduction path from the current collector to the active material through the thickness of the electrode. For illustration purposes, let us assume an electrode thickness of 25 μm. Carbon black CB particles are nearly spherical and have an average diameter of ~30 nm. Many hundreds of CB particles would be required to create a conductive path that would span the electrode thickness. The principal resistance in such a system is likely to be the many particle-to-particle contacts. In contrast, the carbon nanotubes used in the present study had an average length of ~3 μm. The number of nanotubes required to span the electrode would be one to two orders of magnitude fewer than CB particles, with correspondingly fewer particle-to-particle contacts. Thus, the electronic resistance of electrodes containing CNTs is expected to be much lower.

4.2.2 PERFORMANCE OF CNT-CATHODES

4.2.2.1 Long-Term Cycling Performance

Figure 4.9 compares the cycling performance of CNT-cathodes and CB-cathodes at 0.5 C rates. The ordinate represents the fraction of theoretical capacity that was observed. As explained in Section 4.1, electrode compression had a significant impact on the performance of CB cathodes. In particular, uncompressed CB cathodes performed very poorly, dropping to ~35 % of the expected capacity after only 40 cycles. The capacity of compressed CB cathodes remained relatively constant with cycling at ~85 % of the expected capacity. In contrast, the observed cycling behavior of the uncompressed CNT-cathode was very similar to that of the

compressed CB-cathode, indicating the capacity retaining capability of uncompressed CNT-cathodes was comparable to that of the compressed CB-cathodes.

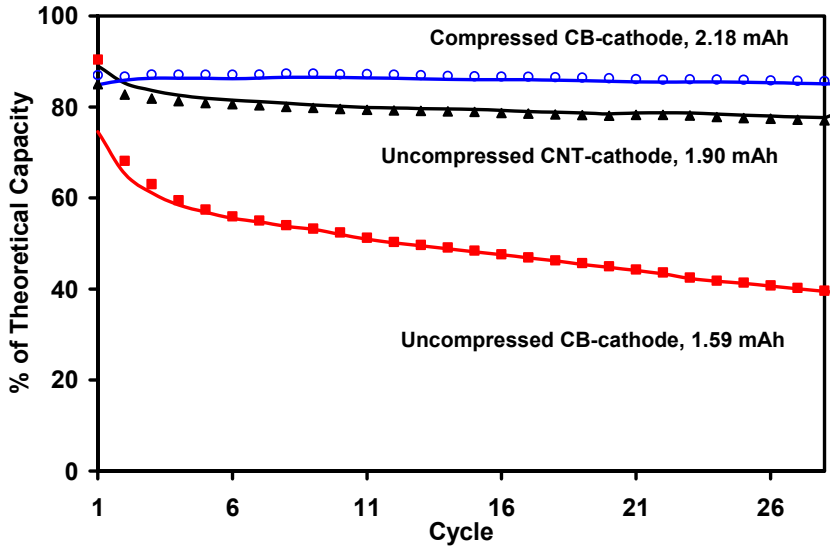

Figure 4.9 0.5 C-rate cycling performance of cathodes containing 7 wt% carbon (~40 μm thick, symbols: charge capacity; line: discharge capacity)

Charge/discharge curves for the above cathodes are shown in Fig. 4.10. The dramatic difference due to compression in CB cathodes is evident from these curves. The voltage profile curves of the uncompressed CNT cathode were similar to those of the compressed CB-cathode, except the observed capacity (normalized) was slightly lower.

The most significant result shown in Fig. 4.9 and 4.10 is that the cycling behavior of an uncompressed CNT cathode was similar to that of a compressed CB cathode. In other words, compression does not seem to be required to improve the performance of CNT-cathodes. In fact, it was experimentally verified that compression did not improve the power performance of CNT-cathodes (see Fig. 4.11). Consequently, use of carbon nanotubes eliminates the need to compress thick-film microelectrodes, greatly simplifying the fabrication procedure.

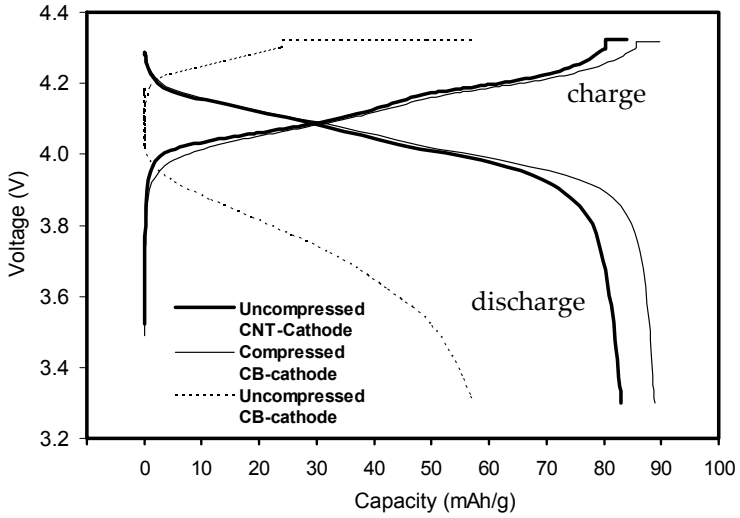

Figure 4.10 Charge/discharge voltage profiles (0.5 C rate, Cycle 6) for electrodes shown in Fig. 4.8

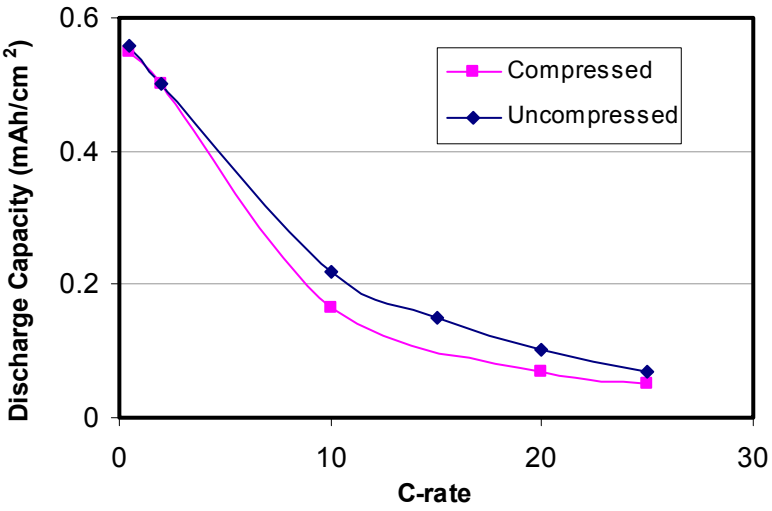

Figure 4.11 Power performance comparison of a CNT-cathode (15 wt% SWNT, 85 μm thick) tested under pressure or without pressure

Figure 4.12 shows cycling data for CNT cathodes without compression. The 12 wt% CNT cathode shown Fig. 4.12(a) demonstrated over 350 cycles at accelerated cycling (2 C charge/ 5 C discharge). The fluctuations observed in Fig. 4.12 were associated with a combination of abbreviated cell conditioning and high rate cycling. Cells with standard conditioning cycles did

not show such fluctuations. Unfortunately, the cells that were more properly conditioned were not cycled for as long as the cell shown in Fig. 4.12. The cathode shown retained over 80 % of its starting capacity at cycle 350 with this 5 C rate cycling.

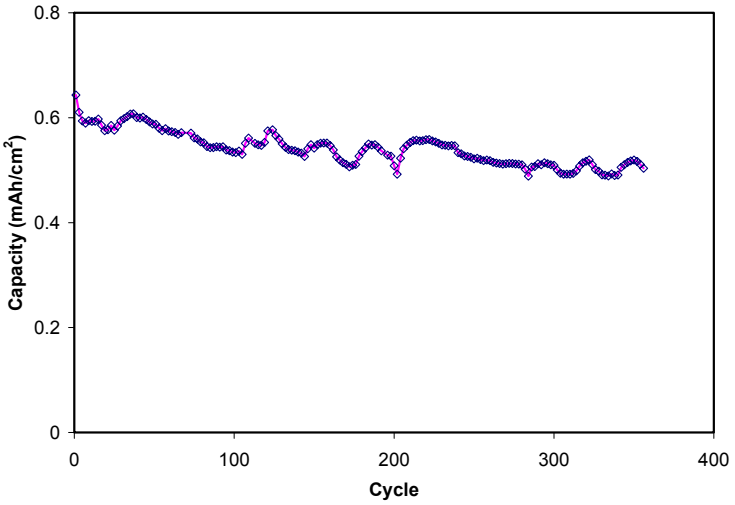

(a)

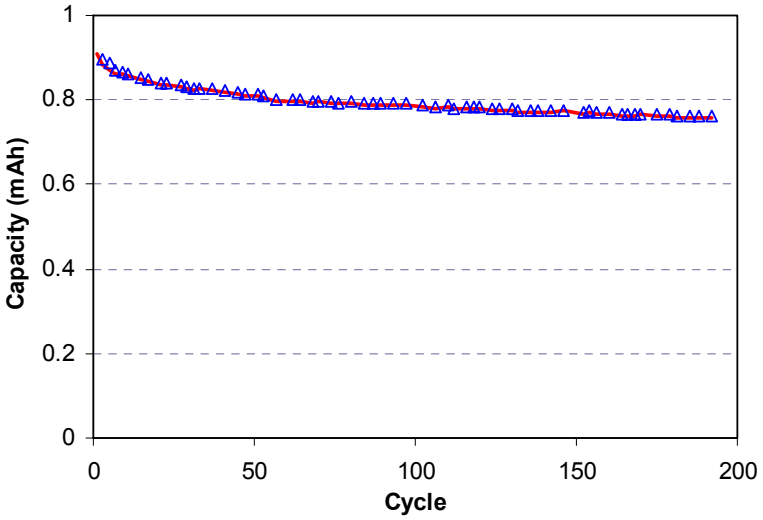

(b)

Figure 4.12 Cycling performance of CNT-cathodes (a: 12 wt% SWNT, 95 μm thick, 2 C charge/ 5 C discharge; b: 15 wt% SWNT, 66 μm thick, 0.5 C charge/0.5 C discharge; symbols: charge capacity; line: discharge capacity)

The 15 wt% CNT cathode in shown in Fig. 4.12(b) demonstrated a stable 0.5 C rate cycling performance and retained about 84 % of its theoretical capacity after about 200 cycles; the average

capacity fade rate was about 0.084 %/cycle. These observations indicated that the uncompressed CNT-cathodes would have sufficient cycle life expectance for the proposed microbattery.

4.2.2.2 Power Performance

Figure 4.13 shows the power performance of an uncompressed 7 wt% CNT-cathode at various C-rates. Compared with that of an uncompressed CB-cathode (similar electrode thickness and active material loading) shown in Fig. 4.4, the power performance of uncompressed CNT-cathode was substantially better. The uncompressed CB-cathodes performed poorly at the 1.5 C rate; even the compressed CB-cathode (shown in Fig. 4.2) only delivered about 13 % of its theoretical capacity at the 10 C rate. However, the uncompressed CNT-cathode delivered over 50 % of its theoretical capacity at a 10 C rate, and delivered ~18 % of its theoretical capacity at a 20 C rate. Note that the 20 C rate corresponded to a current density of 9.5 mA/cm^2 (31.3 mW/cm^2), which was over 60 % of the required power capability and demonstrated the potential of meeting the requirement with CNT-cathodes.

From these comparisons between CNT and CB-cathodes, it was concluded that the power performance of the uncompressed CNT-cathodes was superior to that of CB-cathodes (compressed or uncompressed). Therefore, compression is not needed in CNT-cathodes to achieve the same or better levels of power performance than the compressed CB-cathodes. In other words, the need for compression has been eliminated in composite cathodes by using CNTs to replace CB as the conductive additive. This will greatly facilitate the fabrication of the proposed microbattery.

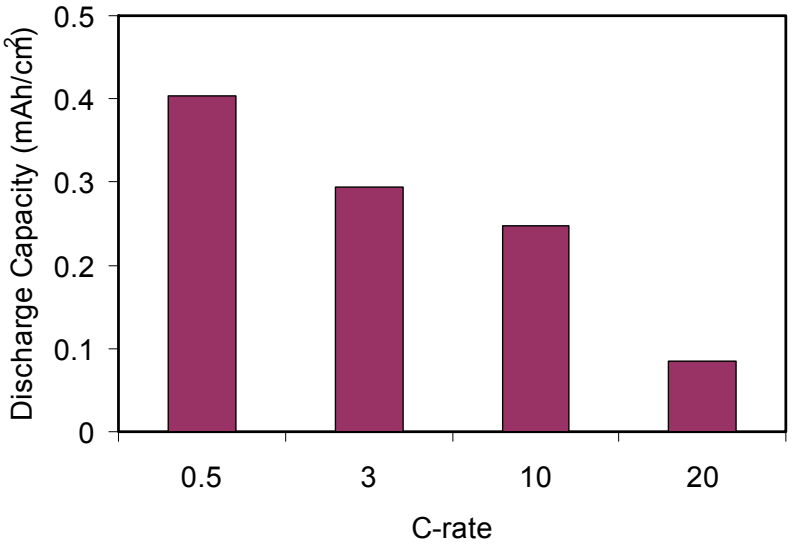

Figure 4.13 Power performance of a 7 wt% CNT cathode (45 μm, 1.90 mAh)

Based on the above observations on the cycling and power performance of the uncompressed CNT-cathodes, it was expected that CNT-cathodes could potentially meet the requirements of the proposed microbattery. Therefore, efforts were made to optimize the performance of the CNT-cathodes; results are reported in the next section.

4.2.3 OPTIMIZATION OF CNT-CATHODES

It is necessary to maximize both power and capacity per area in order to decrease the battery area needed to meet a given duty cycle. The power and capacity are influenced by both the amount of active material present and the relative accessibility of that material. Important experimental variables that affect the amount and accessibility of the material include the electrode thickness, the weight fraction of conductive filler in the electrode and the weight fraction of polymer binder. The influence of these variables is examined in the sections that follow.

4.2.3.1 Cathode Thickness

Tests on the cathodes of different thicknesses were carried out at various discharge rates. Figure 4.14 shows the comparison of discharge capacity of two cathodes, 46 μm and 85 μm in thickness, at a low and a high discharge rate (0.15 and 10 mA/cm^2, respectively). In Fig. 4.14(a) the results are compared on the basis of the mass of active material. It can be seen that at the low rates nearly all active material in both cathodes was accessed. However, at the higher discharge rate, a significantly smaller fraction of active material in both cathodes was utilized, especially for the thicker cathode. This observation is consistent with the expectation that it would be more difficult to access the active material when the electrode thickness is increased due to increased ionic transport and electronic resistance. Figure 4.14 (b) compares the results on the basis of electrode area, which is more meaningful from a practical point of view. The thicker cathode (85 μm) delivered much more capacity per electrode area at both the low and high discharge rates, although the incremental improvement of capacity per electrode area decreased with increasing current density.

Note that the capacity improvement observed at the low rate (0.15 mA/cm^2) in Fig. 4.14(b) for the thicker electrode was greater than that expected from just the change in thickness. This effect (Table 4.2) is believed to be the result of the casting procedure which tends to decrease the concentration of active particles near the top of the composite electrode. The depleted region represents a smaller fraction of the total electrode thickness as the electrode thickness is increased, resulting in a higher average active particle concentration per volume for the thicker electrodes.

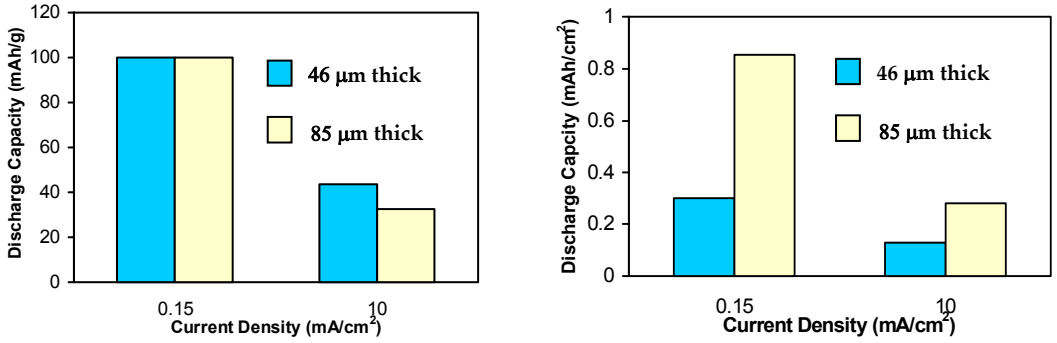

(a) per gram of active material (b) per electrode area.

Figure 4.14 Discharge capacity of cathodes containing 12 wt% CNT

Table 4.2 Relationship between thickness and capacity of 12 wt% CNT-cathodes

Thickness (μm)	24	46	85
Capacity (mAh/cm²)	0.13	0.30	0.87

The results in Fig. 4.14 (b) indicate that electrodes should be built thicker to provide improved capacity and power performance. Efforts were made to increase the thickness of cathodes of different compositions beyond the values reported in Fig. 4.14. It was found that electrode films thicker than 100 μm had a tendency to crack. Therefore, 100 μm was set as the maximum electrode thickness for structural stability in this study. There may be techniques to increase the composite film thickness beyond 100 μm; however, these techniques were not pursued in this study as the desired power level for the proposed microbattery was achieved with electrode thickness of about 100 μm.

4.2.3.2 CNT Content

Conductive material content is critical to the performance of CNT-cathodes. The addition of CNT facilitates electron conduction, improving the active material accessibility and benefiting high power performance. However, increasing the CNT content also reduces the volume fraction

of active material. If the enhancement of performance due to increased accessibility does not exceed the negative impact of the decreased amount of active material, an increase in the CNT content will result in the degradation of both capacity and power.

Experiments were carried out to assess the effect of changing CNT content on the internal resistance and power performance of the CNT electrodes. During these experiments, the total mass of the composite slurries and the weight fraction of the PVDF binder were kept constant. The weight fraction of the active material was decreased to compensate for increases in that of the CNT in order to keep the mass constant. Cathode thickness was controlled in the range of 85~100 μm.

Figure 4.15 shows the influence of CNT content on the internal resistance. When the CNT content was below 7 wt%, the internal resistance was sensitive to the change in CNT content. A small increase in CNT content resulted in a significant decrease in the internal resistance. Relatively little change in the internal resistance was observed for electrodes with a CNT content greater than ~10 wt%. No tests were carried out on cathodes containing more than 15 wt% CNT since an acceptable composite film could not be fabricated due to structural problems (film quality became unacceptable as the CNT content went beyond 15 wt%). As a result, it is recommended that the CNT content should be maintained in the range of 10~15 wt% for high power applications. Lower CNT levels may be acceptable for low rate applications.

Figure 4.16 shows the power performance of cathodes containing different amounts of CNT. In general, the discharge capacity at low rates decreased and that at high rates increased as the CNT content increased. The decrease in capacity at low current densities (left side of figure) was due to the lower weight fraction of active material present in the electrode as the weight fraction of CNT was increased. Note that the low rate capacity of the 7 wt% CNT-cathode was slightly lower than expected from the change of CNT content as its thickness (85 μm) was smaller than

others (90-95 μm). In contrast, additional CNTs increased the capacity at high current densities due to increased accessibility of the active material. Also, the results show that increasing the CNT content from 12 to 15 wt% did not produce a significant change in performance. Therefore, 12 wt% was considered to be the optimal CNT content in this study.

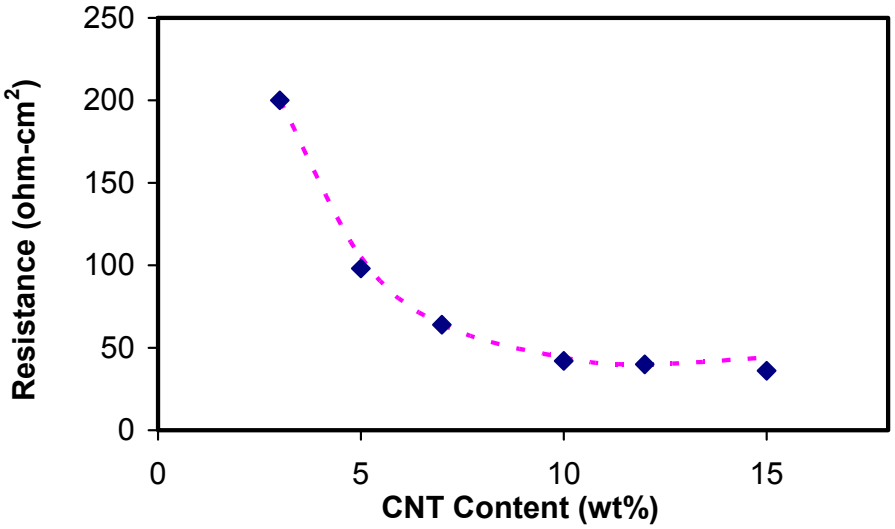

Figure 4.15 Internal resistance of CNT-cathodes (~85-100 μm thick)

Fig. 4.16 also shows that the 85 μm thick cathode containing 12 wt% CNT delivered ~0.17 mAh/cm^2 (energy density ~1.8 J/cm^2) at a current density of 17 mA/cm^2 (56 mW/cm^2). This power density exceeded the power density targeted for the proposed microbattery (50 mW/cm^2). A somewhat lower capacity of ~0.1 mAh/cm^2 (energy density ~1.0 J/cm^2) was observed at a current density of ~26 mA/cm^2 (~85 mW/cm^2). Finally, a 40 mA/cm^2 pulse lasting 0.5 s was achieved with a cutoff voltage of ~2.7 V. The power performance of these electrodes was considerably better than the best values reported for thin-film batteries (~30-35 mW/cm^2 with a capacity of ~0.037 mAh/cm^2) (Neudecker et al. 2000).

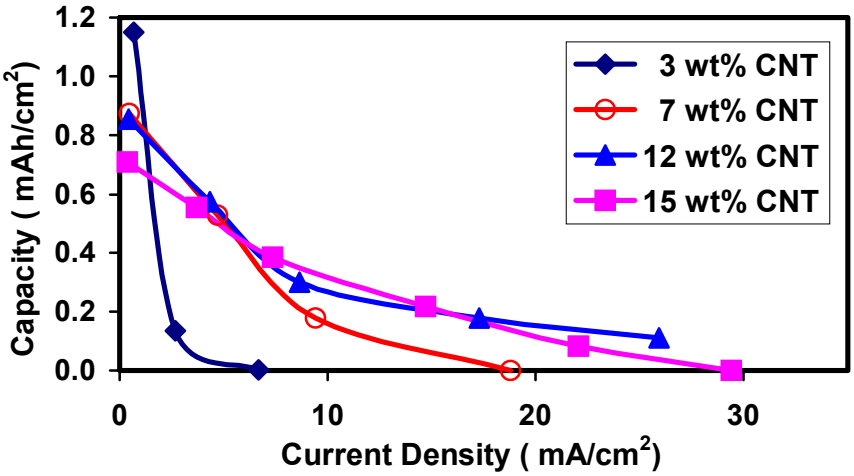

Figure 4.16 Influence of CNT content on the power performance of cathodes ~90 μm thick

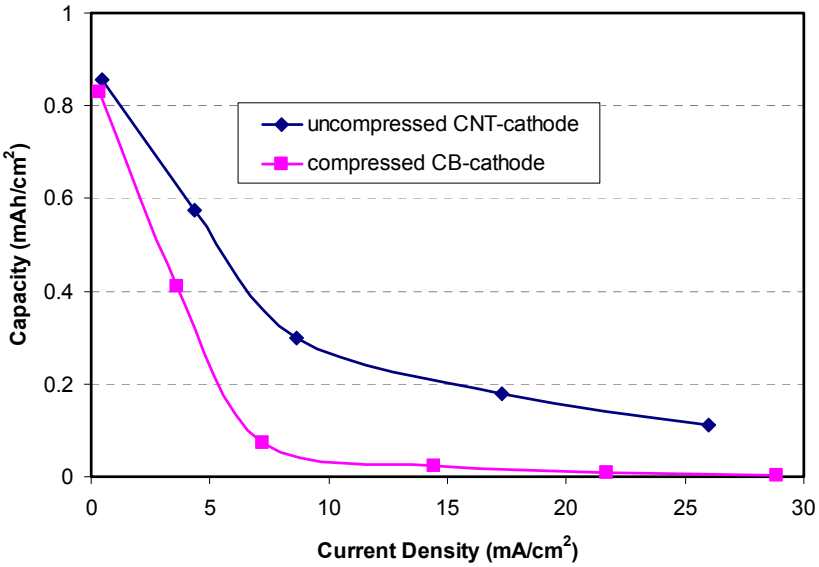

Figure 4.17 Comparison of power performance of 12 wt% composite cathodes (CNT-cathode: 85 μm thick; CB-cathode: 60 μm thick)

Figure 4.17 shows the comparison of the power performance of an uncompressed CNT-cathode and a compressed CB-cathode, each containing 12 wt% conductive additives. Both cathodes had approximately the same theoretical capacity, and showed about the same low rate discharge capacity (CNT cathode: 0.85 mAh/cm^2; CB cathode: 0.83 mAh/cm^2); however, as the current densities increased, the uncompressed CNT-cathode delivered significantly more

capacity than the compressed CB-cathode. It is very clear from this comparison that the uncompressed CNT-cathodes have superior power performance relative to the compressed CB-cathodes.

4.2.3.3 Other Types Of Nanotubes

In the previous sections it was shown that using SWNTs in composite cathodes significantly improved the performance of composite cathodes. As multi-walled carbon nanotubes (MWNT) were readily available in the lab, an experiment was carried out to investigate the effects of using different types of carbon nanotubes (CNT) on the performance of composite cathodes. The most obvious difference between the MWNTs and SWNTs was the size of the tubes. There may also have been differences in the electrical conductivity and level of impurities, but these differences were not addressed in this study.

The MWNTs are 10-40 nm in diameter, and can be thought of as Russian nesting dolls or as multiple SWNTs that fit one inside the other. The electrical properties of MWNTs are not yet fully understood because of the complexity of their structure. The current flows mainly on the outermost shell (probably because of the contact); the conduction showed both quantum (ballistic) and normal (diffusive) characteristics (Forró and Schönenberger 2001). The same article suggested that MWNTs might have lower contact resistances than the SWNTs because of their larger diameter leading to a larger contact area. If this were true in our composite cathodes, it may contribute to a lower internal resistance for the cathodes.

The MWNTs were obtained from two sources, NASA and FLOTU lab (Tsinghua University, Beijing, China). No physical property data for the NASA MWNT were available. The MWNTs from FLOTU lab had an average internal diameter of 7.3 nm, outside diameter of 8-10 nm, and a length >30 μm. The FLOTU MWNTs were fabricated by catalytic chemical vapor deposition of

acetylene on Fe/MgO catalysts at 950 ℃ (Wang et al. 2003). Both types of MWNTs were used as received.

Composite cathodes containing 12 wt% MWNTs from each source, with dry thicknesses ranging from 40-60 μm, were made and tested against Li electrodes. The performance of the MWNT-cathodes at different current densities was compared to that of SWNT-cathodes as shown in Fig. 4.18. It is evident that these uncompressed MWNT-cathodes performed poorly at high current levels; they delivered virtually no capacity at current levels greater than 5 mA/cm^2. In contrast, SWNT-cathodes were capable of being discharged at current densities up to about 18 mA/cm^2. Clearly, the performance of the MWNTs was inferior to that of SWNTs in composite cathodes.

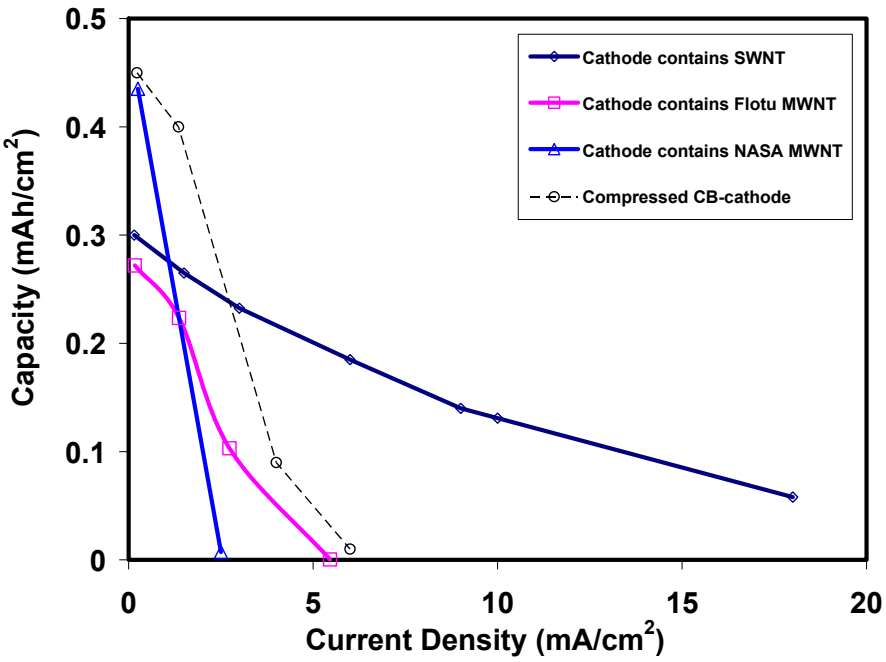

Figure 4.18 Comparison of power performance of cathodes containing 12 wt% different carbon nanotubes (SWNT cathode: 46 μm; Flotu MWNT cathode: 40 μm; NASA MWNT cathode: 61 μm), for comparison, the power performance of a compressed 12 wt% CB-cathode (50 μm) is shown

It was observed that these MWNT-cathodes had much larger internal resistances than the SWNT-cathodes, which explained the difference in their power performance. The internal resistances of MWNT-cathodes (FLOTU) and MWNT-cathodes (NASA) were in the range of 160-480 and 1200-2000 ohm-cm^2, respectively, whereas the SWNT-cathodes with similar nanotube content and thickness had internal resistance of only ~28 ohm-cm^2.

As revealed by Wang et al. (2003), the MWNTs existed in entangled agglomerates, which were 50-500 μm in length. Even the dispersed MWNTs were longer than 30 μm. The length of the MWNTs was at least 10 times larger than the average particle size of the active material used in cathodes in this study (~3.0 μm). The MWNTs were too long to mix intimately with the active material particles, leading to a high internal resistance and poor rate performance of MWNT-cathodes. In contrast, the SWNTs used in this study had an average length of ~3 μm, much smaller than that of the MWNTs and similar to the diameter of the active material particles. Therefore, the SWNTs and the active material particles would mix much better than the MWNTs and the active material particles. The mixing was believed to lead to improved contacts and a smaller internal resistance.

Therefore, of the SWNTs and two types of MWNTs tested in this study, the SWNTs are the best choice based on power performance. The MWNT-cathodes did not have a power capability to meet the requirements of the proposed microbattery. Therefore, the SWNTs were selected as the choice of conductive additive for the composite cathodes.

4.2.3.4 PVDF Content

The impact of PVDF binder content on the performance of the composite cathodes was evaluated qualitatively. The primary function of PVDF is to bind the discrete particulates into a composite film. Since the electrical resistance of PVDF (volume resistivity of ~1x10^{15} Ω-cm was

assumed in Wang et al. 2004) is much greater than the carbon additive in the cathodes, it is desired to use a minimum amount of PVDF that can maintain the structure stability of the electrodes to minimize its negative effect on the electrode conductivity.

The impact of binder content in the SWNT-cathodes was examined by comparing the performance of two batches of cathodes, containing 2.6 wt% and 6 wt% PVDF respectively. The SWNT content was 12 wt% in both batches, and the active material content was 85.4 wt% and 82 wt%, respectively. The electrode thickness was ~100 μm.

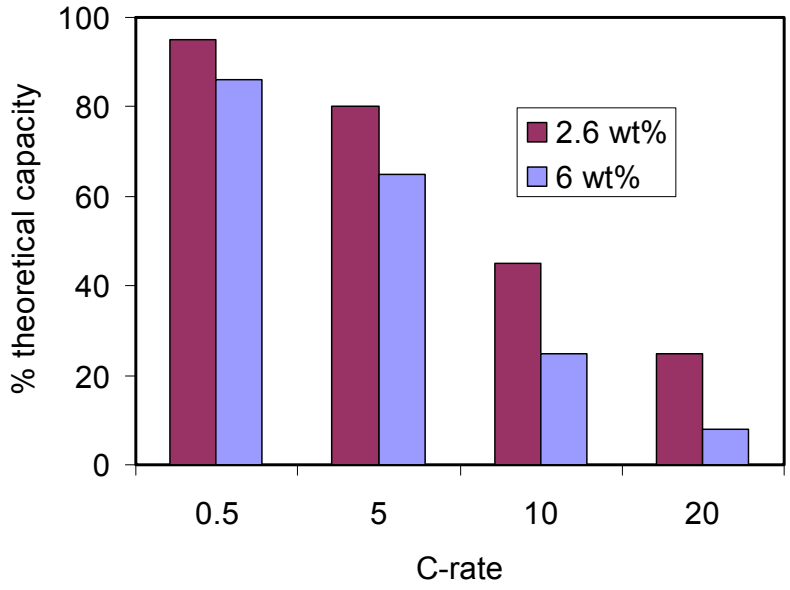

Figure 4.19 Comparison of power performance of 12 wt% SWNT-cathodes of different PVDF contents

It can be seen from Figure 4.19 that the cathode with 2.6 wt% PVDF showed much better power performance than the one with 6 wt% PVDF. The internal resistance of the cathode with 2.6 wt% PVDF was also smaller than the latter one (about 40 and 50 Ω-cm^2, respectively). It is most likely that increasing PVDF binder content increased electrical resistance of the composite films, leading to a higher internal resistance and poorer performance. Besides, the higher PVDF

content may also decrease the electrode porosity and decrease the ionic conductivity in the cathode. A calculation showed that increasing PVDF content from 2.6 wt% to 6 wt% would decrease the electrode porosity by about 2 vol%.

For 12 wt% CNT-cathodes about 100 μm thick, efforts were made to lower the PVDF content below 2.6 wt%. However, a good electrode film could not be obtained with less PVDF. Therefore, it was determined that 2.6 wt% was about the minimum practical PVDF content for these films.

4.3 SUMMARY

In this chapter the performance of uncompressed CB-cathodes was examined, and it was found that the power goal for microbatteries could not be met with such electrodes. It was confirmed that compression was critical to obtain good performance from these CB-cathodes. The composite cathodes using SWNTs as conductive additives were found to have acceptable cycling performance and superior power performance than even the compressed CB-cathodes. Hence the need for electrode compression was eliminated, which greatly facilitates the fabrication of the proposed microbattery.

The CNT-cathodes were optimized to achieve maximum power and capacity per area. The optimized cathodes contained 12 wt% SWNT and 2.6 wt% PVDF, with a thickness of about 100 μm. Continuous power and pulse power were demonstrated at ~85 mW/cm^2 and ~112 mW/cm^2, respectively, which greatly exceeded the power requirements of the proposed microbattery. Therefore, it is feasible to build a high-power cathode for the microbattery. The remaining tasks are to develop a high-power anode and a microbattery fabrication procedure. These tasks are reported in the following chapters.

CHAPTER 5: MECHANISM OF PERFORMANCE IMPROVEMENT IN COMPOSITE CATHODES WITH CARBON NANOTUBES

It was reported in Chapter 4 that the use of SWNTs instead of CB as the conductive filler in composite cathodes had a significant effect on the performance of the composite cathodes: of similar carbon content, the uncompressed SWNT-cathodes showed better discharge power capability than the compressed CB-cathodes of similar film thickness or material loading. The power capability of the optimized uncompressed SWNT-cathodes exceeded the target requirements of the proposed microbattery; therefore, the optimized uncompressed SWNT-cathodes have the potential for use in microbatteries.

As discussed in Chapter 2, the intention of using fibrous SWNTs in composite cathodes was to improve the electronic conductivity of the electrode, and consequently improve the power performance of the cathode. It was shown in Chapter 4 that the internal resistance of the uncompressed SWNT-cathodes was significantly lower, resulting in improved power performance. However, it remained unclear if the SWNTs improve the cathode performance by only improving the electrical conductivity across the composite films, or by also reducing other resistances in the electrodes, since the internal resistance is a sum of different resistances in the composite electrodes.

Therefore, it was necessary to determine the mechanism of how the addition of CNT improved the power performance of composite cathodes. The approach adopted in this study was to analyze the film electrical conductivity data and use a numerical model to determine the major contributions of SWNTs to the reduction of internal resistance. The insight gained from

this investigation will increase our understanding of the factors that limit the performance of composite cathodes, and provide a basis for improvement.

5.1 OVERVIEW

5.1.1 INTERCALATION PROCESS

For simplification, the charge/discharge process can be viewed as a process with two co-current fluxes in the electrodes (Markovsky et al. 1998): electron and lithium ion fluxes. The discharge process in a porous CNT-cathode is shown schematically in Fig. 5.1. The electrons flow from the current collector to the surface of the cathode material via the contacts between the current collector and the conductive network, the conductive network, and the contacts between the conductive network and the active material. The lithium ions transport through the electrolyte rather than the conductive network in order to reach the active material particles. Charge transfer occurs and lithium is inserted into the active cathodic material during discharge.

The rate performance of a lithium-ion battery/electrode depends on the factors that affect one or more steps in the above ionic and electronic processes. The ionic transport properties describe the mobility of lithium ions in composite electrodes. The electrical accessibility (resistance) of an active material particle should be defined as the sum of the conductive network resistance from the location of the particle to the current collector, and includes the electrical contact resistance between the particle and the network. The electrical conductivity of the composite film, directly measurable with various techniques, is determined by the network formed by the conductive filler percolating the film from the current collector to the surface. The significance of electrical contact resistance between the conductive network and the electrode material (also called interparticle contact) was pointed out by Thomas et al. (2002). However,

possibly due to the complex nature and the lack of proper characterization techniques, no values were reported and few models are available to predict the contact resistance.

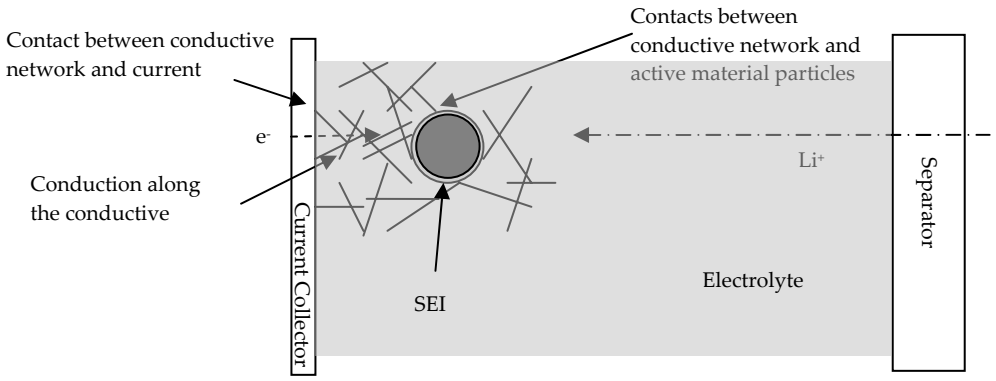

Figure 5.1 A schematic description of discharge (intercalation) process in CNT-cathodes (not to scale)

The difference in the power performance between uncompressed CNT-cathodes and compressed CB-cathodes must originate from the difference in electrode properties due to the different conductive additives. The microstructure differences should lead to differences in one or more steps in the electronic or ionic transport. These differences were divided into 3 groups, which must include the most important factor(s) that leads to the better power performance of the CNT-cathodes:

1) the conductivity of the network formed by the conductive filler;
2) the nature of the electrical contact between the conductive network and active material particles;
3) the pore structure of the electrode (ionic transport).

The first two relate to electronic transport and the third is associated with ionic transport. The following discussion will address the roles of electronic conductivity, ionic transport, and electronic contact resistance on the rate performance of these two types of cathodes. The

discussion will be based on both experimental data and simulation results, which were carried out with a mathematical model developed by J. Newman and coworkers (Doyle et al. 1993, Fuller et al. 1994, Doyle and Newman et al. 1996). Some background information about the model will be given in the next section.

5.1.2 1-D NUMERICAL MODEL

A numerical porous electrode model, developed by Newman and coworkers (Doyle et al. 1993, Fuller et al. 1994, Doyle and Newman et al. 1996), was adopted in this study to seek insight into the discharge process for the composite cathodes, and to examine the impact of porosity, electrode conductivity, and contact resistance on the power performance of the composite cathodes. This model is a powerful tool to examine the voltage profiles and the transient transport processes in composite electrodes, in order to understand the processes that limit electrode performance.

This 1-D "dualfoil" model is a continuum-scale model that incorporates concentrated solution theory, porous electrode theory, Ohm's law, Butler-Volmer kinetics, and the conservation of charge and mass (Doyle et al. 1993, Fuller et al. 1994) to simulate the charge and discharge behavior of lithium and lithium-ion cells consisting of various electrodes and electrolyte materials. Detailed theoretical development of the model can be found in the above literature. A few key points are mentioned here. In this model, the porous electrode is assumed to be a mixture of two superimposed continuous phases: the solid matrix and the electrolyte. The volume fraction of each component, including the active material, inert filler, and pore volume (filled with electrolyte), in each phase are accounted for. The transport properties are adjusted to account for tortuosity of the porous structure using the Bruggeman equation (Doyle et al. 1993).

For example, the diffusion coefficient (D_{eff}) and ionic conductivity (κ_{eff}) of the salt in the electrolyte are calculated by

$$D_{eff} = D \cdot \varepsilon^b \tag{5.1}$$

$$\kappa_{eff} = \kappa \cdot \varepsilon^b \tag{5.2}$$

where D and κ are the intrinsic diffusion coefficient and ionic conductivity of the salt in the electrolyte, ε is the volume fraction of the electrolyte, and b is the Bruggeman exponent.

The electrical conductivity (σ) of the solid phase is related to σ_s, a hypothesized electrical conductivity of the active material, using a similar relationship. Note that σ_s is not a real property of the active material, but a calculated parameter used in the program:

$$\sigma_s = \sigma \Big/ \varepsilon_s^b \tag{5.3}$$

where ε_s is the volume fraction of the active material.

An adjustable parameter, film resistance (R_{film}), is used in the model to better fit the voltage profiles to the experimental data (Doyle et al. 1996). The origin of this parameter was considered to be residual or contact resistance between the electrodes and current collectors, or the resistance on the electrode surface. When considered as the film resistance on the electrode surface, the kinetics of charge-transfer reaction is governed by a modified Butler-Volmer equation:

$$j_n = k \cdot c^{\alpha_a} \cdot (c_t - c_s)^{\alpha_a} \cdot c_s^{\alpha_a} \cdot \left\{ \exp\left(\frac{\alpha_a F}{RT} \left(\eta - U - F \cdot j_n \cdot R_{film} \right) \right) - \exp\left(\frac{-\alpha_c F}{RT} \left(\eta - U - F \cdot j_n \cdot R_{film} \right) \right) \right\} \tag{5.4}$$

where j_n is the pore wall flux of Li^+, k is reaction rate constant, c is concentration of the salt (subscription t refer to maximum concentration, s refer to solid phase), F is the Faraday's constant, R is the gas constant, T is the temperature, α_a and α_c are transfer coefficients, η is surface overpotential, U is open circuit potential, R_{film} is film resistance.

Several system-specific parameters needed to be supplied to the "dualfoil" model, including the open circuit potential (OCP) profile of the electrode material. The OCP profile of $LiAl_{0.14}Mn_{1.86}O_4$ was approximated by a C/40 discharge profile (Fig. 5.2), and the relationship between OCP (U) and state of charge (y, ratio of concentration of intercalated Li^+ to the equilibrium Li^+ concentration in solid phase) was fit with an equation similar to that used in Doyle and Newman et al. (1996):

$$U(y) = 4.90058 + 0.09609\tanh(-4.4639y + 2.57597) - 0.06014(1.91654 - y)^{-0.57751} - 0.78132e^{0.80506\,y^{32.44422}} + 0.05767e^{-50.74297\,y+10.056242} \quad (5.5)$$

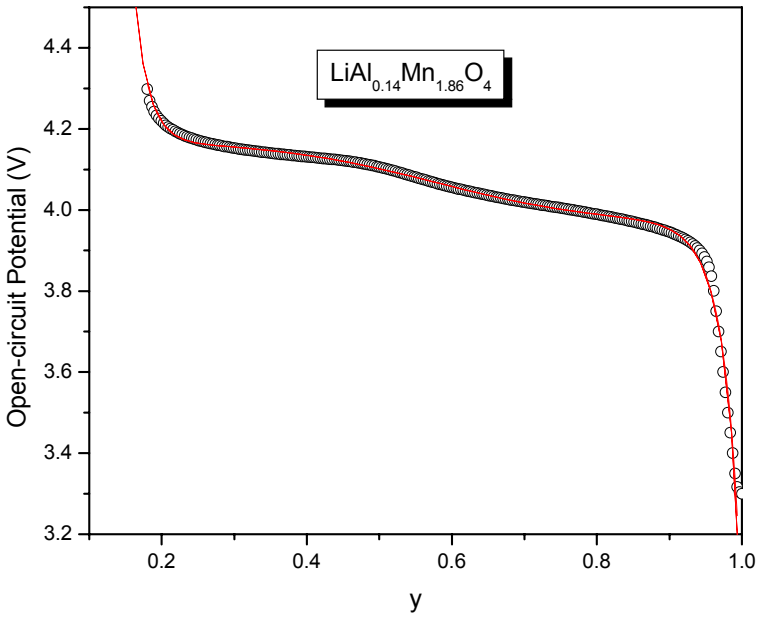

Figure 5.2 OCP profile of $LiAl_{0.14}Mn_{1.86}O_4$ (circles) and fitting with Eq. (5.5) (line)

Other non-adjustable system specific parameters used in the model are listed in Table 5.1. The Bruggeman exponents were 3.3 in the composite cathode (Doyle et al. 1996), 2.8 in the Celgard 2400 separator (Patel et al. 2003). Other variables of interest, including the electrode thickness, volume fractions, and conductivity, will be listed with the discussion of individual electrodes. An example of a full list of input parameters for the model is included in Appendix B.

Table 5.1 System specific parameters used in the model

Parameter	Lithium	$LiAl_{0.14}Mn_{1.86}O_4$
Diffusion coeff. in solid, D_s (cm^2/s)	NA	3.5×10^{-16}
Electrode reaction rate constant, rka(mol/m^2s)	1.14×10^{-5} Note*1	1×10^{-11}
Initial SOC, y_0	NA	0.180
Particle diameter (μm)	NA	3.07
Coulombic capacity of electrode material (mAh/g)	3862	120

Note *1: from Doyle et al. (1993)

5.2 ELECTRONIC CONDUCTIVITY

As shown in Chapter 4, the use of CNTs formed a conductive network that enabled good electrode performance without compression. This ability to create functioning electrodes without compression greatly facilitates microbattery fabrication. It was also observed in Chapter 4 that the high power performance of CNT cathodes was significantly better than that of compressed CB electrodes. The question addressed in this section is whether or not the improved power performance was due to increased electronic conductivity in the CNT electrodes.

The electrical resistance of the composite cathodes was measured to determine the impact of replacing CB with SWNTs on the film electrical conductivity. The resistance was measured between the current collector and Al foil attached on the composite films (which was applied before the films were dried), which represented the resistance along the thickness (Fig. 5.3). The film thickness was measured as described in Section 3.3. The film conductivities were calculated by normalizing the measured resistance with contact area and film thickness. Based on the estimated active material volume fraction (ε_s), the solid phase conductivity (σ_s) can be back-calculated from Eq. 5.3.

Note that a distinction should be made between the resistance mentioned here and the film resistance adopted in the dualfoil model. The measured resistance of composite film represents the electrical resistance of the conductive network of the dry film, which includes the contact

resistance between current collector and composite film, but does not include resistance due to the SEI. The film resistance adopted in the model has two possible meanings: the first is the resistance across the SEI, the second is the contact resistance between current collector and composite film, or between conductive network and the active material particles.

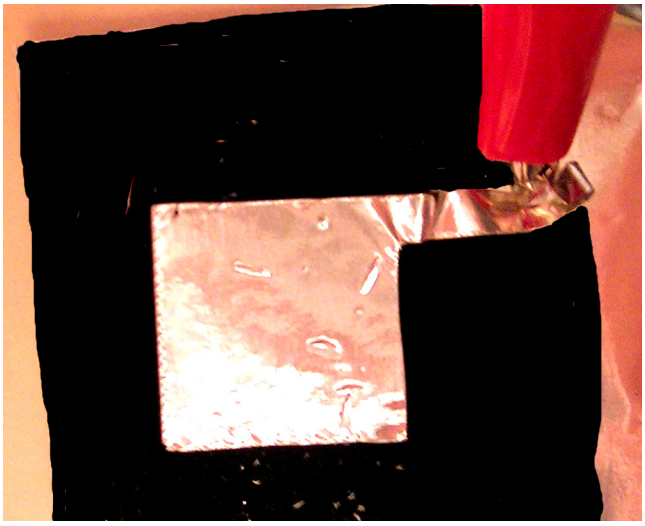

Figure 5.3 Measurement of the electrical resistance across the thickness of a cathode

The values of ε_s and σ_s for CB- and CNT-cathodes are listed in Table 5.2 and 5.3, respectively. The detailed calculation of ε_s can be found in Appendix C. The comparison of film conductivities between these two types of cathodes, uncompressed or compressed, is shown in Fig. 5.4. From the comparison between Table 5.2(a) and 5.2(b), it can be seen that compression improved the film conductivity of the CB-cathodes by ~5-50 times. This provided a good explanation for the observed improvement in the performance of compressed CB-cathodes as shown in Chapter 4.

Table 5.2(a) Measured electrical conductivity of uncompressed CB-cathodes

CB wt%		0	1	3	5	7	12
Vol. Fra.	Conductive	0.000	0.009	0.026	0.038	0.055	0.058
	PVDF	0.028	0.026	0.025	0.022	0.021	0.014
	Active material	0.440	0.412	0.375	0.328	0.307	0.190
	Porosity	0.532	0.553	0.575	0.612	0.616	0.738
Film σ (S/cm)		3.97E-10	3.69E-07	8.22E-06	8.56E-05	4.40E-04	8.19E-04
Estimated σ_s (S/cm)		1.36E-09	1.40E-06	3.58E-05	4.56E-04	2.58E-03	9.88E-03

Table 5.2(b) Measured electrical conductivity of compressed CB-cathodes

CB wt%		0	1	3	5	7	12
Vol. Fra.	Conductive	0.000	0.010	0.030	0.045	0.067	0.070
	PVDF	0.031	0.029	0.028	0.026	0.025	0.017
	Active material	0.484	0.457	0.431	0.389	0.370	0.231
	Porosity	0.485	0.503	0.511	0.540	0.537	0.682
Film σ (S/cm)		1.50E-07	3.00E-06	3.92E-05	1.73E-04	2.08E-03	4.15E-02
Estimated σ_s (S/cm)		4.45E-07	9.71E-06	1.38E-04	7.13E-04	9.23E-03	3.73E-01

Table 5.3 Measured electrical conductivity of uncompressed CNT-cathodes

CNT wt%		0	1	3	7	12
Vol. Fra.	Conductive	0.000	0.011	0.027	0.064	0.067
	PVDF	0.028	0.023	0.018	0.017	0.011
	Active material	0.440	0.355	0.282	0.251	0.157
	Porosity	0.532	0.611	0.672	0.667	0.765
Film σ (S/cm)		3.97E-10	2.87E-06	1.58E-05	1.48E-04	2.14E-04
Estimated σ_s (S/cm)		1.36E-09	1.35E-05	1.05E-04	1.18E-03	3.45E-03

However, Fig. 5.4 and the comparison between Table 5.2 and 5.3 show that the uncompressed SWNT-cathodes had lower measured film electrical conductivities than the compressed CB-cathodes. In other words, even though use of CNTs improved the conductivity relative to the uncompressed CB for carbon contents less than 7%, the conductivity achieved was still less than that measured for the compressed CB electrodes. When the conductive additive contents were in the range of 7 to 12 wt%, the film conductivities of the uncompressed CNT-cathodes were even lower than those of the uncompressed CB-cathodes. However, it was shown in Chapter 4 that the power performance of uncompressed SWNT-cathodes was significantly better than that of CB-cathodes (both uncompressed and compressed), and that the uncompressed SWNT-cathodes had much lower internal resistance than the compressed CB-

cathodes. Therefore, it seems that the film electrical conductivity of uncompressed CNT-cathodes was not the limiting factor for the internal resistance and the electrode rate performance.

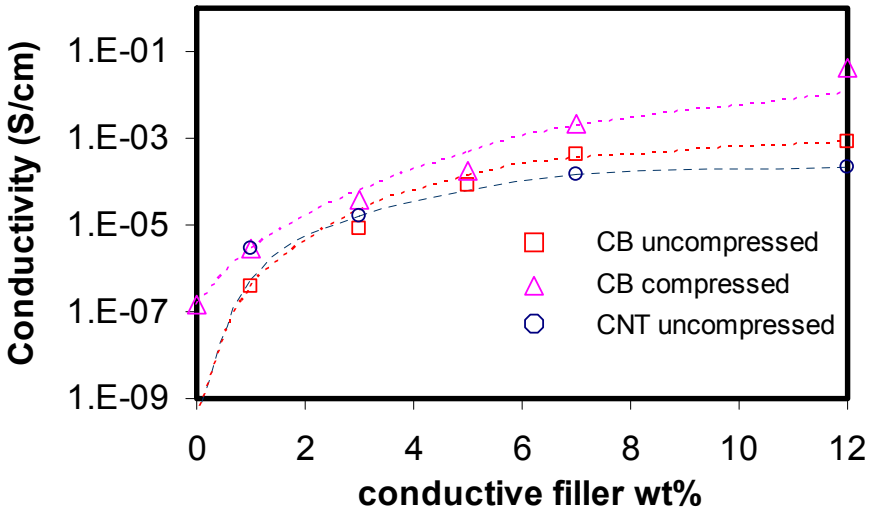

Figure 5.4 Comparison of measured film conductivity between CNT and CB-cathodes

A conclusion can be drawn based on the electrical conductivity data and rate performance data (Fig. 4.17): uncompressed SWNT-cathodes were less electronically conductive but had better rate capability than compressed CB-cathodes. The film electrical conductivity of uncompressed CNT-cathode films was not a limiting factor for the electrode rate performance.

The above conclusion was also supported by the simulations. The discharge voltage profiles of the cathodes (containing 12 wt% conductive additive) in Fig. 4.17 were fit with the dualfoil model. Figure 5.5 shows the simulation results for the uncompressed CNT-cathode. The best fit was achieved with a film resistance of 400 ohm-cm^2. It can be seen that at low discharge rates (0.43 and 1.26 mA/cm^2), the simulated results fit the experimental data quite well; however, at higher current densities, the discrepancies between simulations and measurements became

more pronounced. The discrepancies are mainly seen towards the end of discharge, at current densities of 4.33 and 8.65 mA/cm^2.

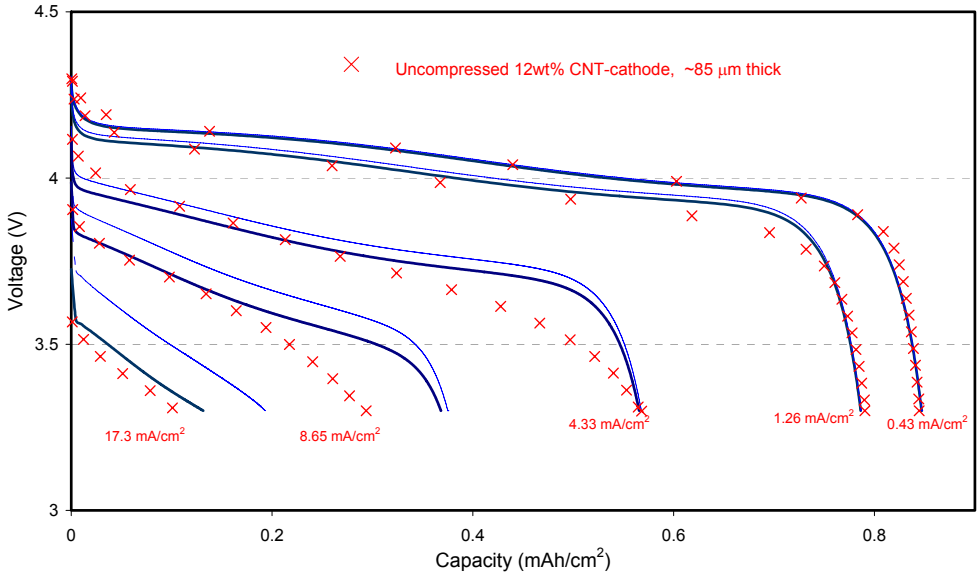

Figure 5.5 Simulation of discharge voltage profiles of an uncompressed CNT-cathode. Symbols: experimental data; thicker (darker) lines: R_{film}=400 ohm-cm^2, thin (blue) lines: no R_{film}.

The simulated results of the compressed CB-cathode are shown in Fig. 5.6. The best fit was achieved with a film resistance of 1200 ohm-cm^2. This value was comparable to those used in Doyle et al. (1996). The simulations fit the experimental data very closely at 0.36 and 2.2 mA/cm^2; however, the simulations overestimated the discharge capacity at 3.6 and 7.2 mA/cm^2.

Note that a significantly smaller value of "film resistance" was used to best fit the discharge curves of the uncompressed CNT-cathode than that for the compressed CB-cathode. Therefore, a substantial portion of this "film resistance" must be associated with resistances in the electrode that are a function of the type of conductive additive used.

The impact of the solid phase conductivity of the uncompressed CNT-cathode on its performance was examined by arbitrarily doubling its value from 0.345 to 0.69 S/m. Slightly higher cell voltages were observed with the higher σ_s (Fig. 5.7). The capacity was literally not

changed at current densities of 4.33 and 8.65 mA/cm², and increased from 0.12 mAh/cm² to 0.14 mAh/cm² at 17.3 mA/cm². This demonstrated that the film electrical conductivity of the uncompressed CNT-cathode only had a small impact on the discharge behavior and was not a limiting factor for the rate performance.

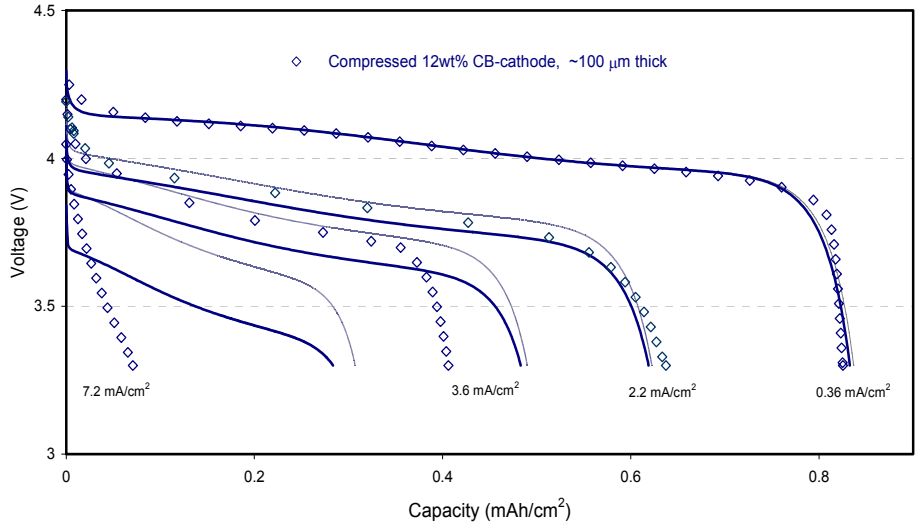

Figure 5.6 Simulation of discharge voltage profiles of a compressed CB-cathode. Symbols: experimental data; thicker (darker) lines: R_{film} = 1200 ohm-cm², thin lines: no R_{film}.

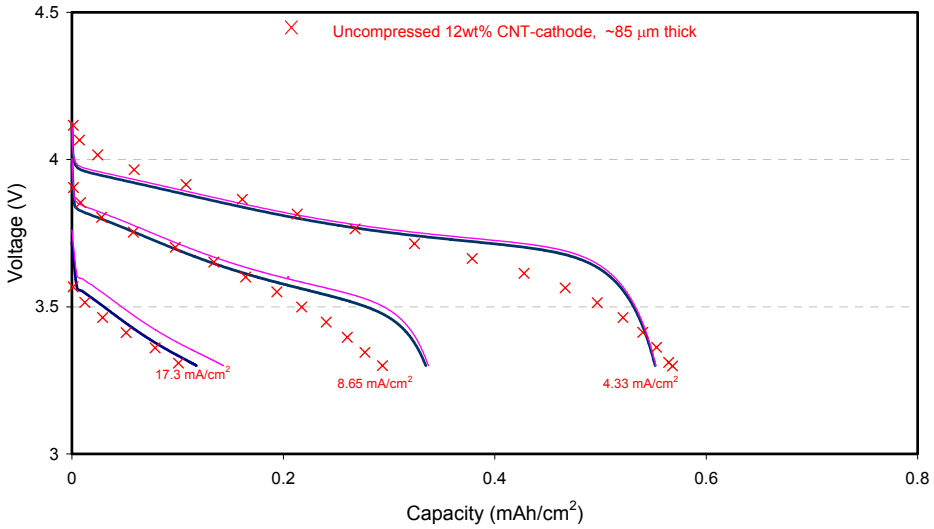

Figure 5.7 Impact of σ_s to the performance of the uncompressed CNT-cathode, with R_{film}= 400 ohm-cm². Dark blue lines (thicker): σ_s = 0.345 S/m ; pink (thin) lines: σ_s = 0.69 S/m.

It is interesting to note that Sakamoto and Dunn (2002) recently observed a similar phenomenon: CNT-cathodes with an electrical resistance of 15.5 kΩ/cm delivered about 30 % more capacity than CB-cathodes with an electrical resistance of 3.4 kΩ/cm at the same current level. Clearly, CNTs must have an impact on electrode performance that extends beyond enhancement of the electronic conductivity.

5.3 IONIC TRANSPORT—POROSITY AND PORE STRUCTURE

At very high discharge rates, lithium ion transport in the electrolyte is one of the limiting processes in the electrode (Patel et al. 2003). Doyle and Newman et al. (1996) demonstrated that at high rates, the solution-phase potential drop is a major contributor to the total overpotential, and that most of the potential drop in the cells occurs in the composite electrode instead of in the separator. They also stated that increasing the volume fraction of the liquid phase (porosity) in the porous electrode led to a substantial decrease in ohmic drop. It was expected that electrode tortuosity may also affect ionic transport similar to electrode porosity; if the electrode tortuosity was decreased while the electrode porosity was not changed, the ion movement through the electrode would be facilitated leading to improved ionic transport.

As both CB and CNT are carbon with different morphologies, the two types of cathodes differ in microstructure, as depicted in the SEM images in Fig. 4.5. The clusters formed by carbon black and the bundles formed by the SWNTs would most likely have different tortuosities and blocking effects of the transport of lithium ions. Such factors were expected to affect the value of effective diffusivity, D_{eff}. For example, D_{eff} was correlated with electrode porosity ε as shown in Eq. 5.1. The Bruggeman exponent b has a value of 1.4-1.5 for a suspension containing mono-dispersed spherical particles. For the spinel particles used in $LiMn_2O_4$-electrodes contained CB

additives, *b* had values of 3.3-4.5 to fit the experimental discharge curves (Doyle et al. 1993; Doyle and Newman et al., 1996). As the SWNT bundles would facilitate the ionic transport better than CB clusters, it was expected that a smaller value of b should be used for SWNT-cathodes than the CB-cathodes. However, as no direct measurement was available, the effect of the conductive additive on the ionic transport was examined by a relaxation technique and by numerical simulation.

In a relaxation test, a cell is allowed to rest after charge or discharge to decrease the concentration gradient established when the current passed through the composite electrode. When a cell is relaxed after being discharged at some significant current level, the cell voltage will recover; the redistribution of Li ions in the composite electrode occurs under the impact of the concentration gradient (Fuller et al. 1994) and the relaxation time (the duration of cell voltage recovers) is an indication of the ionic transport rate in the composite electrode. Therefore, by examining the relaxation behavior of the CB- and SWNT-cathodes it is possible to compare the ionic transport in these two types of the composite cathodes.

However, the relaxation is a complex process. Besides the concentration gradient, the solid phase potential (state of charge, SOC) gradient also impacts relaxation (Fuller et al. 1994). For a better understanding, Figure 5.8 illustrates the build-up of Li^+ concentration gradients in the electrolyte (C_{E,Li^+}) and in the solid phase(C_{s,Li^+}) in a composite cathode during the discharge process, in which the ohmic drop in the solid phase is assumed to be small. During this process, lithium ions move from the anode (negative electrode) into the cathode (positive electrode). Under the impact of concentration gradient, the solid phase lithium concentration is higher where the Li^+ concentration in the electrolyte is higher, which corresponds to a higher potential. Therefore, the profile of SOC gradient is similar to that of the concentration gradient. At the end

of discharge, both the established SOC profile and electrolyte concentration gradient will be higher in the separator region and lower in the region near the current collector.

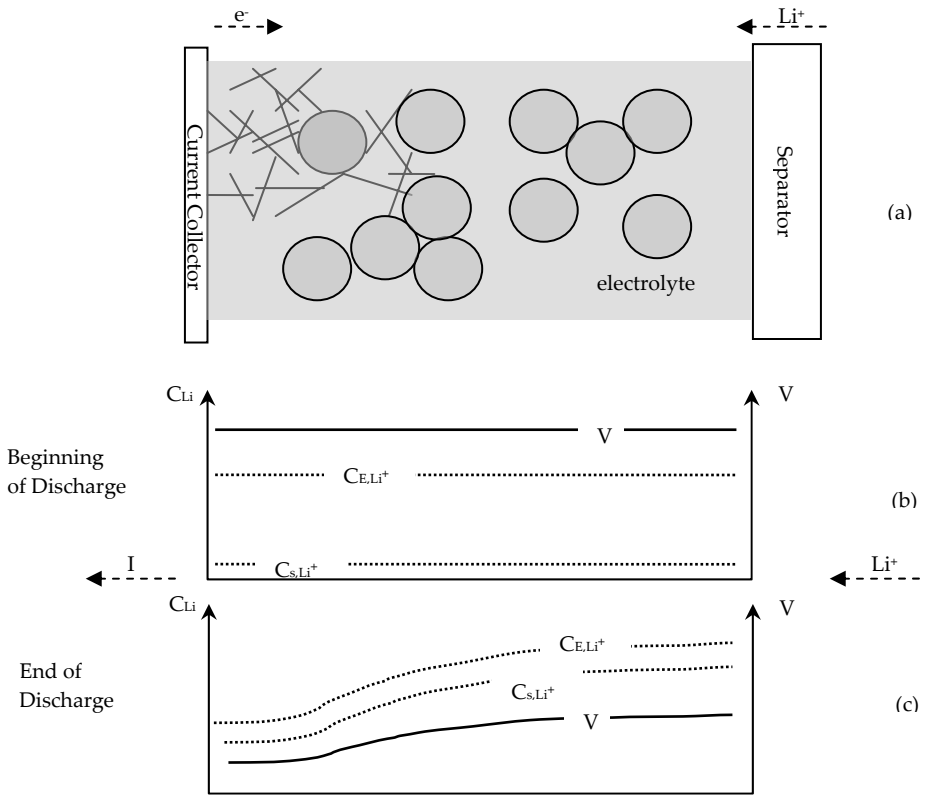

Figure 5.8 Schematic description of changes in voltage (electrical potential in solid phase) profile and Li^+ concentration profiles during discharge process (a) sketch of composite cathode and separator, only some conductive additives are shown (b) profiles before discharge (c) profiles at the end of discharge

When the (discharge) current stops, the Li^+ redistribution is driven by solid phase potential (state of charge, SOC) and electrolyte concentration gradients (Fuller et al. 1994). The potential gradient will cause Li^+ to de-intercalate from the near separator region (higher potential), transfer and intercalate into the near current collector region (lower potential). This lithium transfer process occurs in the same direction (from the separator to the current collector) as that driven by electrolyte concentration gradient in the same direction. Therefore, it is expected that the

relaxation would be a combined result of the SOC gradient and electrolyte phase transport. As the SOC gradient is affected by interparticle electrical connections, it is expected that the electrical connectivity would have an impact on the relaxation of the SOC gradient.

In this study, a pulse discharge and relaxation test was performed in different composite cathodes. Ong and Newman (1999) claimed that double layer capacitance relaxation should be insignificant in this type of pulse discharge and relaxation phenomenon, and the impact of capacitance to the voltage profile is negligible. After the composite cathodes were taper-charged at 4.30 V, they were discharged for 1 second at different current levels. The current was then stopped and the cells were allowed to stand for a prolonged period (in the range of 10 seconds to several minutes), in which the cell voltage was continuously monitored until it reached a steady state. The pulse duration was selected to be 1 second to insure the establishment of concentration gradient of Li^+ without significantly changing the state of charge (SOC) of the electrode. For example, after the cell was pulsed at a current of a 40 C rate for 1 second, SOC changed only 1.1 %. A digital oscilloscope (54620 series, Agilent Technologies) that is capable of sampling at 20 MHz was used to capture the rapid change during the transient stage.

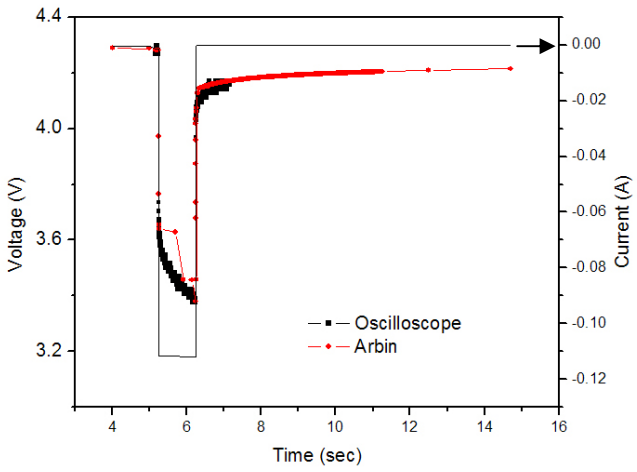

Figure 5.9 1-sec pulse discharge (40 C-rate) and relaxation of a compressed CB-cathode

A typical voltage profile for these tests is shown in Fig. 5.9. Note that the digital oscilloscope gave a more accurate voltage measurement than the Arbin tester following the rapid change of the pulses, as the Arbin tester was only capable of a sample rate up to 100 Hz. Therefore, the voltage profiles recorded with the digital oscilloscope provided insights to study the cells' immediate response to the pulse. As the oscilloscope only recorded $2x10^6$ data points each run, corresponding to only 10 seconds of test time at sample rate of 200 kHz, the data recorded by the Arbin tester was used to study the longer-term response of the cells.

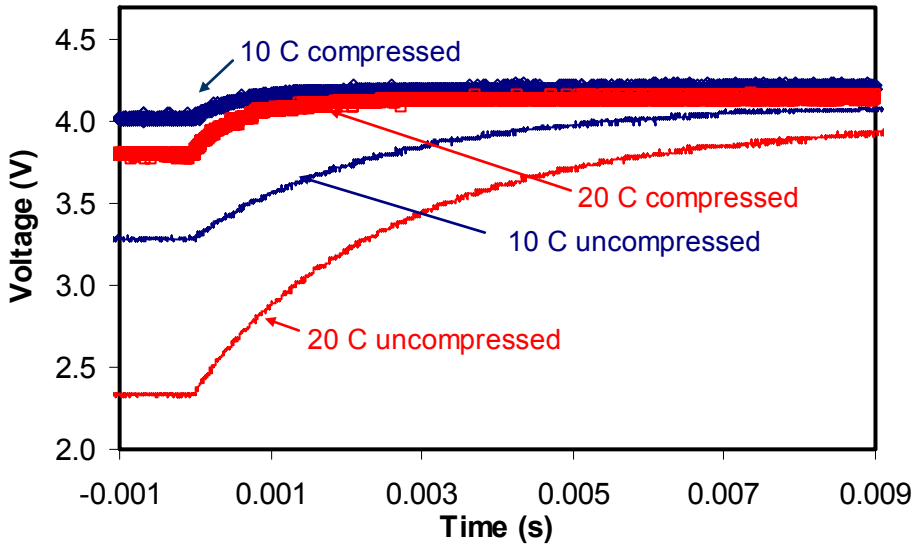

Figure 5.10 Comparison of measured relaxation behaviors between CB-cathodes after pulse discharges

The voltage changes during relaxation for several CB-cathodes are shown in Fig. 5.10. It can be seen that for both compressed and uncompressed CB-cathodes, it took longer for the cell voltage to stabilize when the cell was pulse discharged at a higher C-rate. This was expected as a greater concentration gradient existed in the cathode when the cell was discharged at a higher rate. Comparing the relaxation behavior at the same C-rate, it can be seen that the difference in the relaxation time was marginal; however, the magnitude of cell voltage change was smaller for

the compressed cathodes. Since the compressed CB-cathodes had a lower porosity but a better electronic conductivity than the uncompressed ones, it seemed that the better electronic conductivity led to a more uniform SOC profile across the compressed CB-cathodes than that in the uncompressed ones, causing the major difference depicted by the voltage profiles.

Figure 5.11 compares the transient behavior of voltage relaxation between an uncompressed CNT-cathode and a compressed CB-cathode after pulse discharges. It can be seen that at the same C-rates (10 C or 40 C), the voltage relaxation behavior was very similar for these two cathodes, and the uncompressed CNT-cathode had a slightly smaller voltage change than the compressed CB-cathode. This indicated that the difference in the ionic transport between compressed CB-cathodes and uncompressed CNT-cathodes was minimal or unimportant, and the uncompressed CNT-cathode had a more uniform SOC distribution that the compressed CB-cathode.

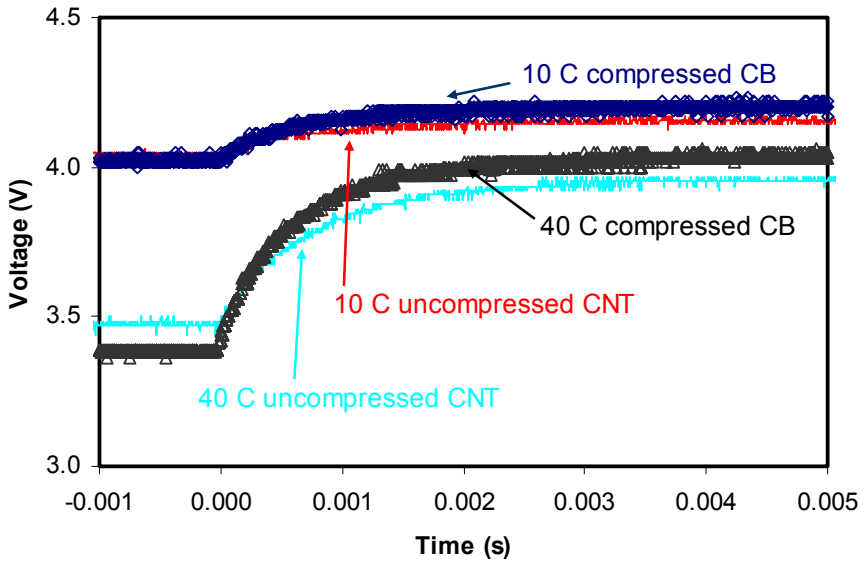

Figure 5.11 Comparison of measured pulse-relaxations between an uncompressed CNT-cathode and a compressed CB-cathode

The above experiments examined the voltage relaxation behavior of cathodes after pulse discharges. The voltage relaxation behavior of cathodes after longer discharges was also investigated. In this test, a set of 12 wt% CNT-cathodes and CB-cathodes were first charged to 4.30 V and taper-charged to ensure a fully charged state; then they were discharged at 0.1 C, 0.5 C, or 10 C-rates to 4.05 V and allowed to rest for 1 hour. The cut-off voltage was selected to be about the center voltage of plateau region of the OCV curve for the cathode material (see Fig. 5.2) to minimize the effect of lithium redistribution caused by the local SOC gradient. These cathodes had theoretical capacity of about 2.8 mAh, with electrode thickness of about 60 μm.

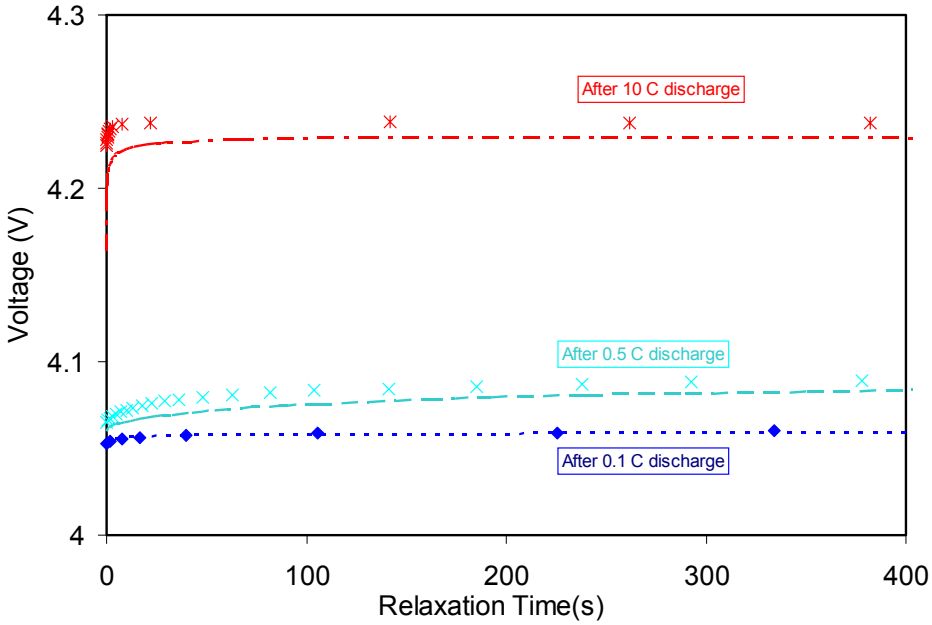

Figure 5.12 Measured relaxation behaviors after constant rate discharges to 4.05 V (symbols: compressed CB-cathode; lines: uncompressed CNT-cathode)

It was found that after the cells stayed in the rest state for a few minutes, their voltages became stabilized. Therefore, the cell voltage changes in only the first 400 seconds in relaxation were shown in Figure 5.12. It can be seen that at C/10 rate, the uncompressed CNT-cathode and compressed CB-cathode had near identical voltage relaxation curves, indicating that the

difference in the ionic transport was not important for these two cathodes. This was explained by the fact that the discharge current is sufficiently low and the material accessibility thru the electrode film was quite uniform; when the discharge current stopped, the concentration gradients were small and comparable in both electrodes. At 0.5 C and 10 C rates, the magnitudes of voltage changes were smaller in the uncompressed CNT-cathode than in the compressed CB-cathode, indicating the SOC gradients were smaller in the uncompressed CNT-cathode than the compressed CB-cathode. The difference in voltage relaxation between these two cathodes was more substantial at the 10 C rate and the 0.5 C rate.

Two conclusions were drawn from the above observations on voltage relaxation after pulse and constant discharges. The first conclusion was that the difference in the ionic transport between the uncompressed CNT-cathodes and compressed CB-cathodes was insignificant; the second was that the uncompressed CNT-cathodes had a more uniform SOC profile thru the composite film than the compressed CB-cathodes. As the ionic transport in these two cathodes was similar, the more uniform SOC distribution in the uncompressed CNT-cathodes would most likely be caused by better interparticle electrical contacts in the solid phase.

The impact of the ionic conductivity on the cathode rate performance was also examined in simulation by changing electrode porosity. The porosity was arbitrarily decreased from 0.765 to 0.305 while the volume fraction of active material was kept constant by adding inert volume to the simulation. From Fig. 5.13 it can be seen that the porosity change had virtually no effects to the delivered capacities, although the voltage profiles were slightly decreased. The more significant difference between the cell voltage profiles of different porosities at 8.65 mA/cm^2 than that at 17.3 mA/cm^2 was due to the fact that the cell voltage was cut off earlier at 17.3 mA/cm^2.

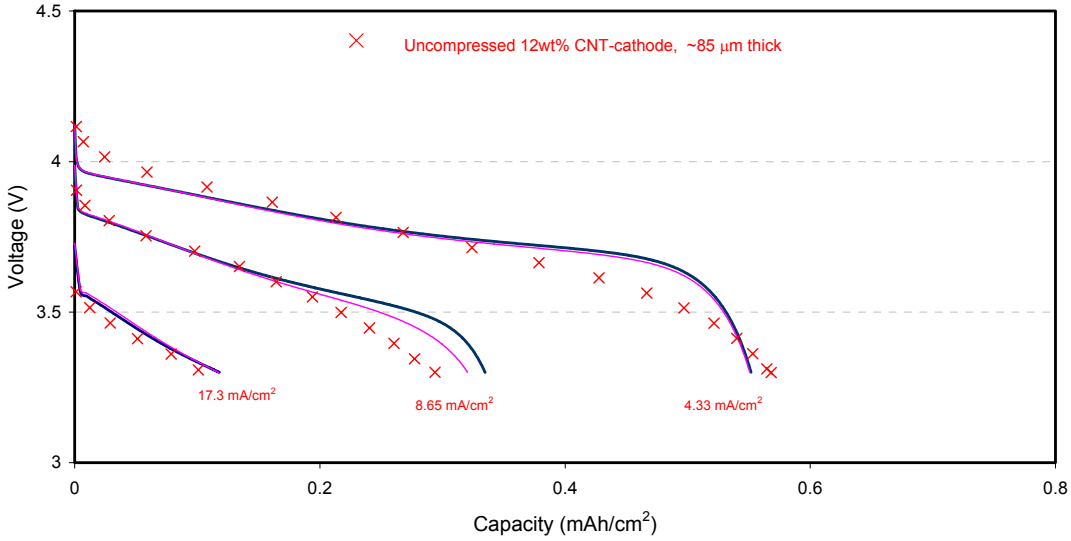

Figure 5.13 Predicted effect of change of porosity of the uncompressed CNT-cathode shown in Fig. 5.5 (Dark blue thick lines: simulation with porosity of 0.765; pink thin lines: simulation with porosity of 0.305)

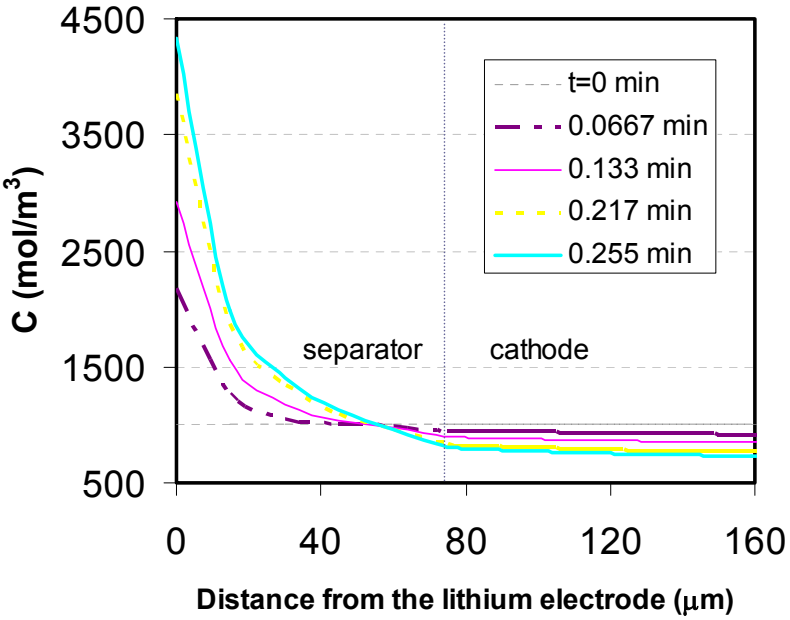

Figure 5.14 Salt concentration profiles in the CNT-cathode(I = 17.3 mA/cm², R_{film} = 400 Ω-cm²)

The profiles of Li^+ concentration in electrolyte can be obtained in the simulations. The profiles shown in Fig. 5.14 are the results corresponding to I = 17.3 mA/cm² and R_{film}= 400 Ω-cm².

It can be clearly seen that the most concentration gradients existed in the separator and the concentration profiles in the cathode were nearly flat. This indicated the ionic transport in the composite cathode was adequately fast and should not be a limiting factor for the rate performance.

In summary, no significant difference between the ionic transport behaviors in uncompressed CNT-cathodes and compressed CB-cathodes was observed, although the electrode structures constructed by the CNTs and CBs would be different in the composite cathodes. It was also theoretically verified that ionic conductivity did not play a significant role in the cathode's rate performance. Therefore, the possibility of the contribution of ionic transport difference to the high-power performance between uncompressed CNT-cathodes and compressed CB-cathodes was ruled out. Since in Section 5.2 the film electrical conductivity proved to not be the cause for the superior power performance of the uncompressed CNT-cathodes, the most probable explanation was that the electrical contacts among the active material particles in the uncompressed CNT-cathodes were better than those of the compressed CB-cathodes.

5.4 CONTACT RESISTANCE AND OTHER ISSUES IN COMPOSITE CATHODES

As discussed in the previous two sections, it is clear that the uncompressed CNT-cathodes do not have better film electrical conductivity or ionic transport than the compressed CB-cathodes. However, the uncompressed CNT-cathodes showed significantly better power performance than the CB-cathodes. The most likely cause was identified to be that the uncompressed CNT-cathodes have better electrical contacts among active material particles than those in the CB-cathodes.

The electron conduction in a composite film is determined not only by the film conductivity, but also by the electrical contacts between the conductive network and the particles. Therefore, low resistances in both the conductive network and the electrical contacts between the network and electrode particles are essential to electrode performance, especially rate capability. Although the electrical film conductivity of the uncompressed CNT-cathodes was lower than that of the compressed CB-cathodes, if the electrical contacts in the uncompressed CNT-cathodes were of lower resistance than those in the compressed CB-cathodes, the total resistance to electron conduction in the CNT-cathodes could be lower than that in the CB-cathodes. As the power performance of the CNT-cathodes is significantly better than that of the CB-cathodes, and the improvement is not due to ionic transport, it is certain that there is significant improvement in electron conductance, which is most likely due to the improvement in electrical contacts.

From the data and analysis in the previous sections, it can be concluded that the CB-cathodes had good film electrical conductivities but the electrical contacts among the particles were highly resistive; as the result, the overall resistance to electron conductance in CB-cathodes was high and the rate performance was poor. The compression enhanced the film electrical conductivity and probably improved electrical contact with active particles to yield significantly better performance. For the CNT-cathodes, the situation appeared to be different: the film conductivity was lower than that of the CB-cathodes but sufficiently high, and the electrical contacts were much better than those in the CB-cathodes; therefore, the overall resistance to electron conductance in CNT-cathodes was significantly lower than that of the CB-cathodes even when the latter were compressed, and the rate performance was much better than that of the CB-cathodes.

Although the interparticle contact is important to the electrode performance (Thomas et al. 2002), no experimental data are available to quantify the contact resistance. Numerical work

offers some insight for this parameter. The "film resistance" defined in the dualfoil model is a parameter to compensate the inadequacy of using film conductivity alone to fit experimental data (Doyle et al. 1996). It was treated as the resistance of the electrode surface, but its possible origin could also be residual or contact resistance between the electrodes and current collectors (Doyle et al. 1996). A value in the range of 1000 to 1700 Ω-cm^2 for R_{film} was found to best fit the discharge voltage curves of the composite $LiMn_2O_4$ cathodes with CB conductive additive (Doyle et al. 1996). Note that the surface area in the film resistance is the particle surface area; therefore, the above R_{film} values correspond to 400-680 Ω-cm^2 per electrode surface area, which is more than 2 orders of magnitudes larger than the film electrical resistance (2.9 Ω-cm^2 per electrode surface, calculation based on film electrical conductivity of $6x10^{-3}$ S/cm and the cathode thickness of 174 μm, Doyle et al. 1996). This comparison qualitatively demonstrated that relative importance of film electrical conductivity and interparticle contact in the performance of these composite electrodes.

In the simulation, R_{film} of 1200 Ω-cm^2 for the compressed CB-cathodes was comparable to the values used in Doyle et al. (1996). The simulation also indicated that the CNT-cathodes had significantly lower "film resistance" than the CB-cathodes. As in this study, the active material and electrolyte were the same in both CNT- and CB-cathodes, the resistance due to the electrode film (SEI) should be about the same; therefore, the difference in "film resistance" between these two types of cathodes should come from the difference in the interparticle contacts. As the difference (400 Ω-cm^2) is significant compared to the "film resistance" of the two types of cathodes (400 and 1200 Ω-cm^2), it can be concluded that a substantial part of this "film resistance" comes from interparticle contact. Therefore, the simulation results support the proposed explanation that the uncompressed CNT-cathodes had a much smaller interparticle electrical contact resistance than the compressed CB-cathodes.

As briefly illustrated in Chapter 4, one advantage that SWNTs have over CB in electrical network in the composite cathodes is the morphology. The average length of SWNTs (2-3 μm) used in this study is comparable to the size of the active material particles (diameter of ~3 μm), which has an important impact on the degree of intermixing of these two materials. From the experimental data it could be deduced that the SWNTs were well dispersed in the composite cathodes, and established good interparticle contacts. The interparticle conductive paths of SWNTs should contain most likely an order of magnitude of fewer carbon-carbon contacts than those with CB particles (average diameter of ~30 nm). Reducing the number of carbon-carbon contacts in these paths would certainly reduce the resistance to electron conductance and hence improve the electrode rate performance.

Another benefit of using SWNTs as conductive additive is that the interparticle conductive paths would be much more stable than those with CB particles. In CB-cathodes carbon displacement has been observed (Kostecki 2004), which resulted in loss of surface electronic conductivity and deteriorated active material accessibilities. This may partially explain the capacity fade in long term cycling of the CB-cathodes, and may also explain the poorer high rate performance of the CB-cathodes if the integrity of the conductive paths degrades as CB particles dislocate especially under the impact of stress caused by passing high currents. In this context, the SWNTs seem to be a better candidate as they tend to be less mobile because of their length and tensile properties. Furthermore, the elasticity of SWNTs may allow them to maintain the electrical contacts to the active material particles without being dislocated when the particles expand or contract during Li ion intercalation and de-intercalation. These assumptions would prove more useful if in-situ observation of electrode microstructure changes could be made.

Therefore, this study proposes following mechanism for the difference in power performance between the uncompressed CNT-cathodes and compressed CB-cathodes: the use of

SWNT in the composite cathodes most likely significantly improved the electrical contacts between the conductive network and the active material particles, and amongst the active material particles. Such improvements in interparticle contacts were due to the morphology of the SWNTs, which reduced the number of contact points in the conducting paths and minimized the electrical resistance. Hence the electrical accessibility of the active material was significantly improved and consequently the rate capability of the composite cathodes was substantially improved.

It is noted that there may be other possible explanations that this study did not address. For example, active material particle clusters could have significant detrimental impacts on the high rate performance, as pointed out by García et al. (2005). The particle clustering may be less severe in the CNT-cathodes than in CB-cathodes, as the active material particles may intermix with SWNTs better than with CB particles. Such a difference in intermixing may be the result of that the size of active material particles is comparable to the length of the nanotubes, but is significantly larger than that of the CB particles. Particle clustering may have detrimental impacts on both ionic and electronic accessibility to the active material particles. Further experimental investigations are needed to verify such a theory.

5.5 SUMMARY

A mechanism was sought to account for the better power performance of uncompressed CNT-cathodes than the CB-cathodes. The film electrical conductivity and ionic transport in CNT- and CB-cathodes were experimentally investigated, and the results showed that the CNT-cathodes did not have better properties in these two parameters. A numerical model was also used to examine the impacts of these two parameters, and the simulation results indicated that

film electrical conductivity and porosity were not limiting CNT-cathodes' performance. The simulation results also indicated that the CNT-cathodes had a significantly lower "film resistance" than the CB-cathodes. Based on these results, a mechanism was proposed: SWNTs in the composite cathodes did not improve the film electrical conductivity and ionic transport, but most likely significantly improved the interparticle electrical contacts that improved the electrical accessibility of the active material and consequently improved the rate capability of the composite cathodes. The morphology of the SWNTs, compared to the CB particles, contribute to electrical contact improvements by building more continuous and robust conductive paths among the active material particles.

CHAPTER 6: COMPOSITE ANODE AND BATTERY ACTIVATION

Chapter 4 described the development and characterization of a thick-film composite cathode with a power capability greater than 50 mW/cm^2. As the objective of this study was to develop a high-power lithium-ion microbattery, a composite anode was needed with a power capability of equal to or greater than that of the cathode when cycled without compression. This chapter describes the development of such an anode and an efficient activation technique that facilitates the fabrication of a lithium-ion microbattery.

6.1 COMPOSITE ANODES

Similar to composite cathodes, composite anodes generally contain active material, conductive additives and a polymer binder. The active material for composite anodes in this study was MCMB, unless otherwise stated. PVDF was used as the polymer binder. The Super P carbon black was used as the conductive additive at the beginning of this study. The typical composition is listed in Table 3.1. Although compression would improve the performance of these composite anodes, it may not be practical in the proposed microbattery. Therefore, these anodes were tested against Li counter electrodes without being compressed.

It should be noted that in the early stages of this study, the composite anodes did not go through an activation procedure (i.e. a forming cycle); they were cycled following the regular testing procedure (listed in Chapter 3) from the beginning of the tests. Cycling data from these tests generally contained some fluctuations or showed a much higher capacity fading rate than

previously reported (Holladay 2000). Later it was found that these phenomena were due to the absence of a stable SEI film in these anodes (which will be discussed in greater detail in Section 6.2).

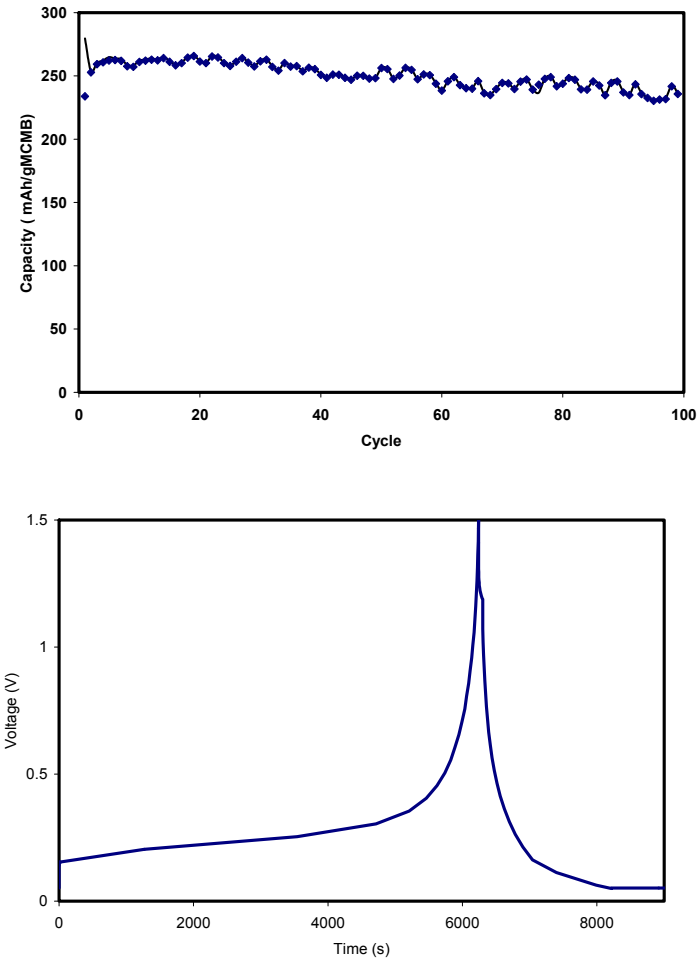

Figure 6.1 0.5 C rate Cycling behavior and voltage profile of a composite anode (90 %MCMB, 5 % super P, 62 μm thick, 5.3 mAh; refer to Fig. 4.1 for legend use)

Figure 6.1 shows the 0.5 C rate cycling performance and voltage profile for a composite anode using Super P as the conductive additive, without being activated. From the graph it can be seen that there was a plateau in the voltage range of 0.05 to 0.5 V when the anode was being charged (delithiated) to 1.5 V (the cut-off voltage was selected in a range that the capacity is not sensitive to voltage change, see Hossain et al. 2003). It was identified that the small magnitude

fluctuations in the cycling curve was related to the unstable SEI in anode. The anode had an irreversible capacity loss of about 30 mAh/(g MCMB) in the first cycle, and the capacity at cycle 8 was about 260 mAh/ (g MCMB), which is about 13 % lower than the value reported by Linden and Reddy (2001) at similar conditions (about 290-305 mAh/g MCMB at cycle 8). The discrepancy was a result of the important role of compression in the performance of these anodes, which was experimentally verified in this study. The anode retained over 240 mAh/(g MCMB) after 100 cycles, which was greater than 90 % of the starting capacity; the average capacity fade rate in the first 100 cycles was about 0.08 %/cycle, which was comparable to that obtained by Holladay (2001). The internal resistance was about 130 ohm-cm^2 at 0.5 C rate.

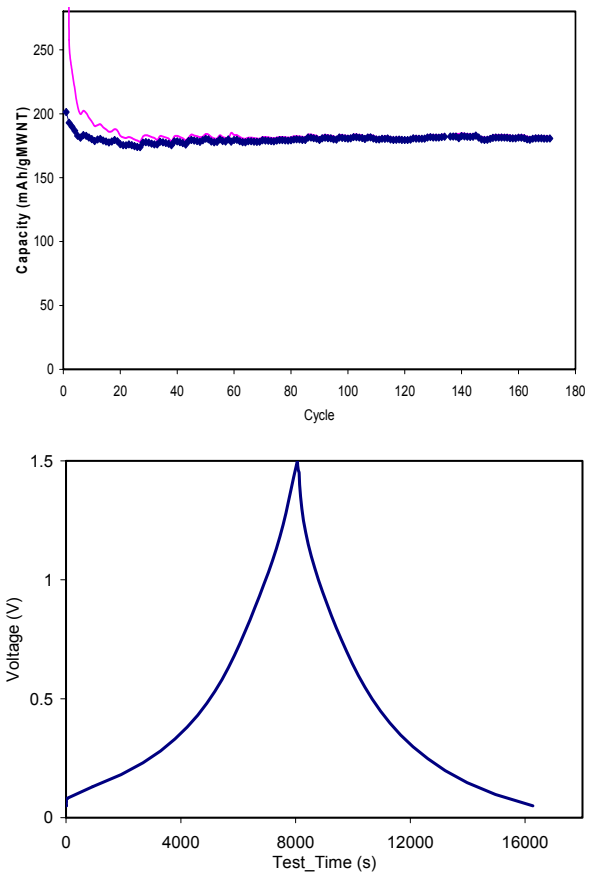

Figure 6.2 0.5 C rate Cycling behavior and voltage profile of a MWNT anode (85 % MWNTs and 15 % PVDF, 63 μm, 0.70 mAh; refer to Fig. 4.1 for legend use)

Multi-walled carbon nanotubes (MWNT) had been tested as the anode material in lithium batteries with promising performance (e.g. Mukhopadhyay et al. 2002). As a sample was readily available (c.a. 10 nm in diameter, length ~30 μm; FLOTU lab, Tsinghua Univ., Beijing, China), MWNTs were tested as the anode material in this study. These anodes contained 85 % MWNTs and 15 % PVDF, without any conductive additive. From Fig. 6.2 it can be seen that there was no obvious plateau in the voltage profile of the MWNT anode and its cycling performance was very stable. The reversible lithium ion intercalation capacity of this MWNT sample at a 0.5 C rate in the voltage range of 0.05-1.5 V was measured to be about 183 mAh/(g MWNT), which was comparable to the value reported in Mukhopadhyay et al. (2002). However, it should be noted that these anodes were very porous and one in Fig. 6.2 only had about 0.70 mAh; the active material loading was about 1/8 of that of the MCMB + super P anode shown in Fig. 6.1. The irreversible capacity in the first cycle was about 860 mAh/(g MWNT), which was significantly higher than its reversible capacity but in the range of reported values (e.g. ~130 mAh/g MWNT in Mukhopadhyay et al. 2002, ~1200 mAh/g SWNT in Claye et al. 2000). The internal resistance at 0.5 C rate was about 80 ohm-cm^2, only about 2/3 that of MCMB + Super P anodes.

From the above observations, especially the high irreversible capacity loss and the low material loading, it was concluded that MWNT was not a good choice for the anode material. However, noting the more stable cycling performance and the lower internal resistance of MWNT anodes relative to the MCMB anodes, a recipe was formulated to combine the advantages of both materials. This recipe used 90 wt% MCMB, 5 wt% MWNT and 5 wt% PVDF, without any Super P carbon black additive. Figure 6.3 shows the performance of a composite anode using this recipe. The voltage profile was similar to that of the first formula (MCMB with Super P carbon black additive, Fig. 6.1); the irreversible capacity loss was about 40 mAh/(g MCMB) in the first cycle, and the capacity at cycle 8 was about 265 mAh/ (g MCMB). The

internal resistance was about 80 ohm-cm² at 0.5 C rate, which was similar to that of the MWNT anode although the electrode thickness was more than twice that of the MWNT anode. These observations indicated that the MCMB dominated the lithium intercalation processes. The MWNT enhanced the electrode conductivity and reduced the internal resistance, which resulted from a similar effect as using SWNT in the cathodes. As the MCMB particles used in this study are about 20-30 μm in diameter, which is comparable to the length of the MWNTs, it was expected that the MCMB particles would intermix well with the MWNTs. Such an intermixing effect was identified to be an important parameter in the performance of cathodes using SWNTs as additive, as reported earlier in Chapter 4.

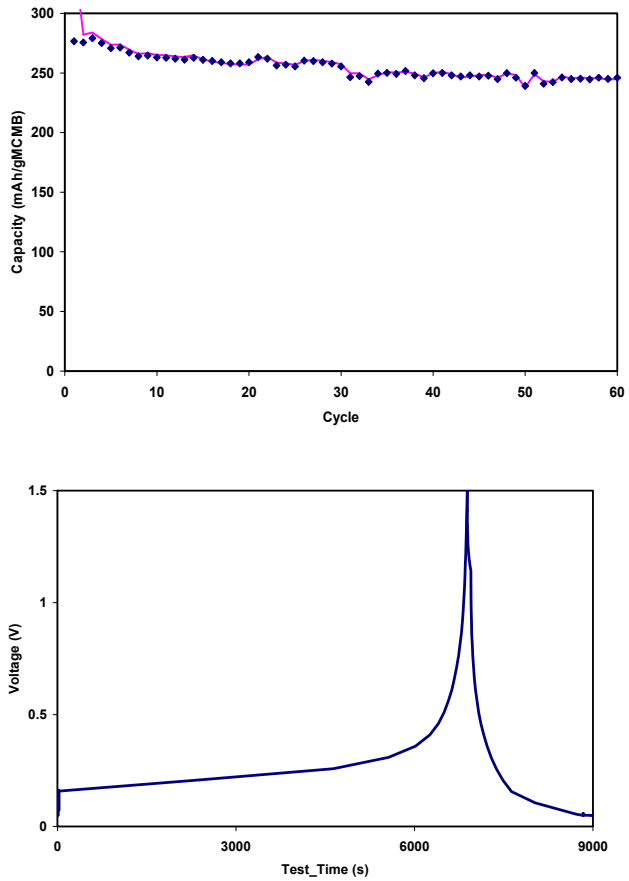

Figure 6.3 0.5 C rate cycling behavior and voltage profile of a MCMB+MWNT anode (90 wt% MCMB, 5 wt% MWNT, 140 μm, 9.0 mAh; refer to Fig. 4.1 for legend use)

The power performance of MCMB + Super P anodes and MCMB + MWNT anodes, without being compressed, are shown in Fig. 6.4. The power performance of the optimized cathode recipe is also shown in the plot for comparison. Note that the capacity of the anodes were matched to about 80 % that of the cathode. It can be seen that the delivered capacities of all the anodes decreased with increasing current densities, similar to that of the CNT-cathodes. The power performance of MCMB + Super P anodes was poor and far less than that of the CNT-cathode; however, the MCMB +MWNT anode delivered significantly higher capacities than the CNT-cathodes at high current densities. This observation showed that the power performance of the MCMB+MWNT anode was superior to that of the CNT-cathodes.

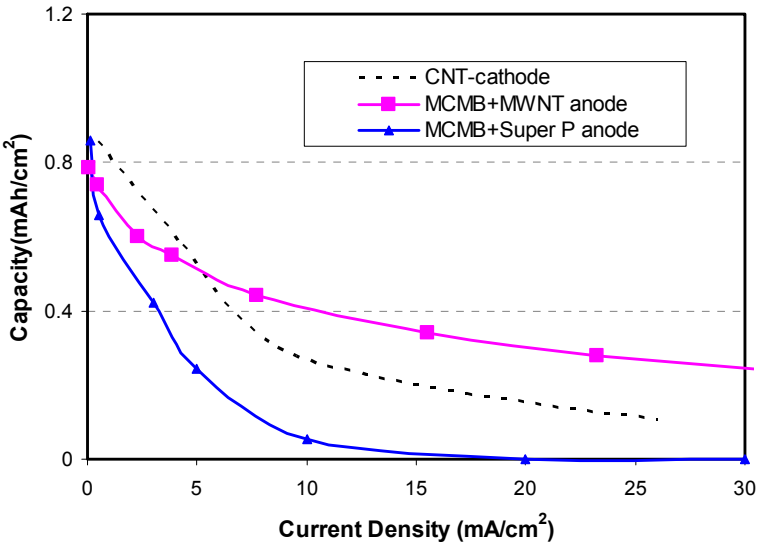

Figure 6.4 Power performance of composite anodes (MCMB + MWNT anode: 90 wt% MCMB, 5 % MWNT, 5 % PVDF, 40 μm thick; MCMB + Super P anode: 90 wt% MCMB, 5 % Super P, 5 % PVDF, 35 μm thick); for comparison, the power performance of a 85 μm CNT-cathode is shown

Based on the comparison of cycling and power performances among different anode formulas, the recipe of 90 wt% MCMB and 5 wt% MWNT was selected as the choice for this study. It was expected that as the power capability of the anode exceeded that of the cathode, the

power performance of the proposed lithium-ion microbattery would be limited by the cathode instead of the anode.

6.2 BATTERY ACTIVATION

The above results show that the MCMB + MWNT composite anodes had adequate power capability for use in lithium-ion batteries for the micropower system. Note that the tests presented in the above section did not include a forming step; as a result, the cycling performance was not stable and fluctuations could be seen on the cycling curves; however, since there was excess amount of Li^+ source from the lithium counter electrodes in these testing cells, even without proper activation, the cycling performance of testing cells for composite anodes was acceptable.

However, the situation is different in a lithium-ion battery, which consists of a composite cathode and a composite anode. As commonly accepted, an activation procedure is necessary to form a stable thin film (solid-electrolyte-interface, SEI) on the active material particles of carbonaceous anodes (Linden and Reddy 2001), which is electronically insulating but lithium-ion conducting. When the SEI is formed, lithium is incorporated into the passivation film causing irreversible capacity loss (ICL). If the activation is properly accomplished, the ICL should occur only in the forming cycle (which is also generally the first cycle); otherwise, the SEI layer will not be sufficiently stable and the ICL may continue with continued cycling (Wang et al. 2001). As the source of lithium in the lithium-ion batteries is generally the lithiated cathodes (in this study the $LiAl_{0.14}Mn_{1.86}O_4$ cathode), which is limited, a continuous lithium consumption will result in performance degradation. Therefore, activation is critical in lithium-ion batteries.

It should be mentioned that the composite anodes were made 20-30 % lower in capacity than that of the cathodes to compensate for the ICL in the SEI forming cycles (Linden and Reddy 2001). This electrode capacity matching is common practice to achieve an optimal material usage and battery performance.

6.3.1 PERFORMANCE OF BATTERIES WITHOUT ACTIVATION

In the early stages of this study, the lithium-ion batteries were tested without activation. A typical result of cycling performance is shown in Fig. 6.5. The capacities of the cathode and anode of this battery were calculated by the mass of electrode material to be 1.6 and 1.3 mAh, respectively; therefore, considering the ICL to form SEI in the first cycle to be about 25 % (the mid value of 20-30 % as stated in Linden and Reddy 2001), the reversible capacity of the battery was estimated to be about 1.1 mAh. The 1st cycle discharge capacity of the battery closely matched this estimation.

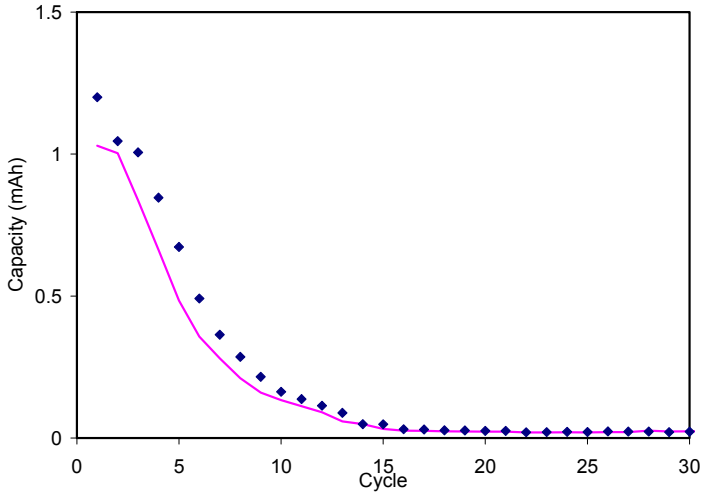

Figure 6.5 0.5C cycling performance of a Li-ion battery without activation (refer to Fig. 4.1 for legend use)

As shown in the figure, this unactivated battery faded quickly to virtually no capacity in 15 cycles. Similar results were observed in the cycling performance of other lithium-ion batteries without activation. Obviously such a cycling performance will not be acceptable in the proposed microbattery. Proper battery activation was necessary to reduce the capacity fade rate and prolong battery life.

6.3.2 ACTIVATION TECHNIQUE

A successful activation should form a stable SEI film on the surface of active material, which will sustain continuous cycling. Activation can be done either with a few forming cycles at a very low current density (e.g. 2 cycles at C/25 rate, see BATT testing protocol at http://isswprod.lbl.gov/battdatasite/), or with a special procedure (Hariharan 2002) to be described below. This study adopted the latter method based on its capability to achieve good anode performance in a shorter time.

The activation procedure described in Hariharan (2002) generally required 18~34 hours to form a stable SEI film. This procedure included:

1) Assembling the lithium-ion battery in the glovebox, filling it with liquid electrolyte, and letting it stand for 12-16 hours without sealing;
2) Charging at 1/4 to 1/3 mA/cm^2 for 1-6 hours, to form a passivation layer on the anode;
3) Letting the cell stand at open circuit for 1~8 hours to allow the electrolyte to distribute through the anode;
4) Charging to 4.1 volts at a current density ~2-100 times larger than the first charge current density;
5) Venting the gas generated;

6) Discharging the battery to about 2.5 V at a current density ~10-100 times larger than the first charge current density (This step is to reduce the energy in the cell but leave a sufficient density of Li ions in the anode to support the graphite structure);
7) Sealing the cell.

Modifications were made to the above activation procedure to make it more suitable for this study. It was unnecessary to vent the gas formed during activation in macro-sized flat cells since the pouches were oversized to the electrodes and the excess volume accommodated the gas without affecting cell performance. For microbatteries, it is desirable to avoid venting as it may increase the complexity of the fabrication procedure. Therefore, the modified activation procedure does not include a gas venting step and the gas generated during activation was minimized by using sufficiently small currents.

The above procedure used absolute current densities, which were suited for batteries with well defined capacities (e.g. commercial batteries); however, in this study, especially when different recipes were tested and the batteries' capacity was not defined, a C-rate based procedure would be more suitable as variations in battery capacities were accommodated. After experimenting with different C rate values, the activation procedure was modified as follows:

1) The battery was filled with liquid electrolyte, sealed and allowed to sit for about 5 hours;
2) The first charge was performed at 0.05 C rate for 2 hours;
3) The battery was allowed to rest for 4 hours;
4) The second charge was performed at 0.1 C rate to 4.1 V;
5) The battery was allowed to sit for about 0.5 hours;
6) The battery was discharged at 0.1 or 0.2 C rates to 2.8 V (note: the lower voltage limit was changed to match the value used in this study).

The activation generally required 26-32 hours. An example of battery voltage and current profiles during activation using the modified procedure is shown in Fig. 6.6. Note that the capacities of the electrodes were properly matched, and the estimated battery capacity was used to determine the values of currents used in the activation.

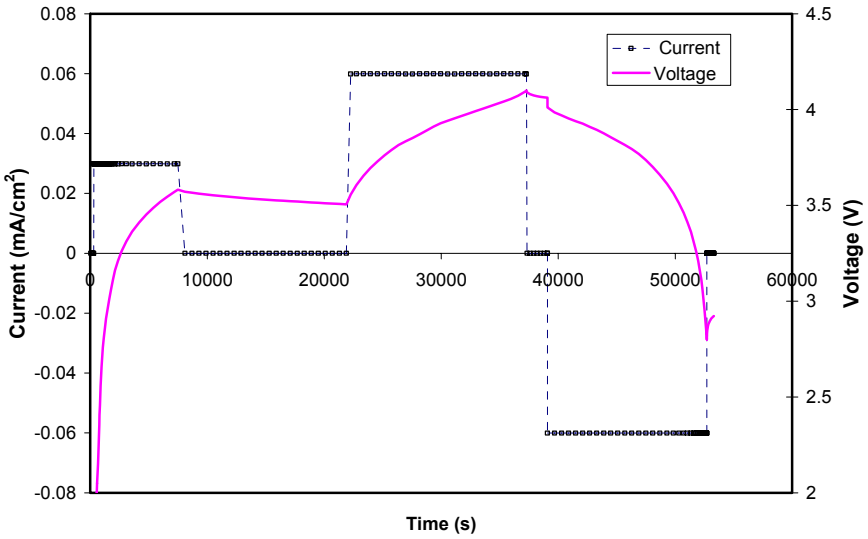

Figure 6.6 Current and voltage profiles of a lithium-ion battery during activation

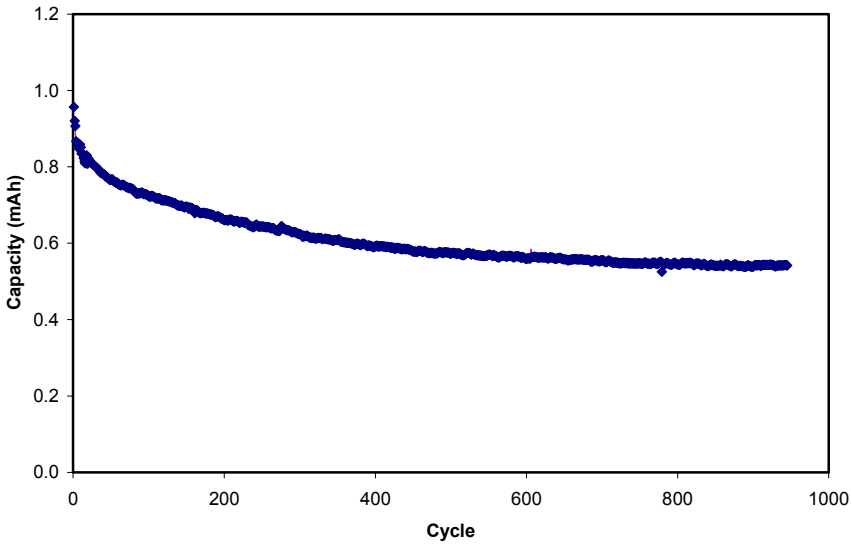

Figure 6.7 0.5 C-rate cycling performance of a Li-ion battery (refer to Fig. 4.1 for legend use)

A lithium-ion battery, consisting of a 1.2 mAh SWNT-cathode and a balanced MCMB + MWNT anode, was activated and then cycled at 0.5 C-rate and full depth of discharge. Its cycling performance is shown in Fig. 6.7. It can be seen that after almost 1000 cycles, the battery retained over 57 % of its first cycle capacity. Compared with the cycling performance of the unactivated battery shown in Fig. 6.5, it is obvious that this battery was successfully activated and cycled well.

The above activation technique provided sufficient cycle life for the microbatteries developed in this study, as the recipe of the microbatteries was similar to the macro batteries tested in this section. This procedure was also proven to work well for microbatteries without gas venting, which will be shown in Chapter 7.

6.3 SUMMARY

In this chapter, different materials for composite anodes were tested. Based on comparisons of the cycling and power performance, it was determined that a composition of 90 wt% MCMB and 5 wt% MWNT would be adequate for the anode of the proposed microbattery. This anode showed significantly better power performance than that of the optimized CNT-cathodes, indicating that the composite anodes would not be a limiting factor for the power performance of the proposed microbattery.

Without proper activation, the composite lithium-ion anodes showed poor cycling performance. A C-rate based activation procedure was developed and was proven to be suitable for the 4 cm^2 lithium-ion batteries of this study. This procedure, which does not include a gas venting step in order to facilitate the microbattery fabrication, should be suitable to the proposed microbatteries to obtain a desirable cycle life.

CHAPTER 7: MICROBATTERY DEVELOPMENT AND CHARACTERIZATION

In this chapter, the development and characterization of a high-power thick-film lithium-ion microbattery are described. Several different substrates were investigated, including a Si wafer, a polypropylene film and a Cyclic Olefin Copolymer (COC) film. The COC film proved to be the most successful for the cells considered in this study. The performance of the microbattery, including cycle life and power capability, was characterized.

7.1 SI WAFER BASED METHOD

Currently, the vast majority of microsensors and other microelectronics are fabricated on Si substrates using well-established integrated circuit processes. It was believed that building microbatteries on the same substrate as the microsensor devices would facilitate their integration. The initial substrate used for microbattery fabrication was a silicon wafer.

A side-by-side Si-based microbattery design was adopted in a previous attempt to fabricate a lithium-ion microbattery (Holladay 2001), as shown in Fig. 7.1. Note that electrical connection to the electrodes was made by patterning the current collectors larger than the sealing material. The microbattery was made by first etching electrode receptacles in a Si wafer, coating metallic current collectors, depositing composite slurries into the receptacles with a syringe, injecting liquid electrolyte, and finally sealing with a glass slide.

Holladay (2001) showed that microbatteries fabricated according to the above design were only capable of very low power. He found a significant ohmic drop above the small separating

wall between the electrodes since all lithium ions had to transfer across the small space. Since this problem is inevitable with a side-by-side electrode layout, his design was not adopted in this study.

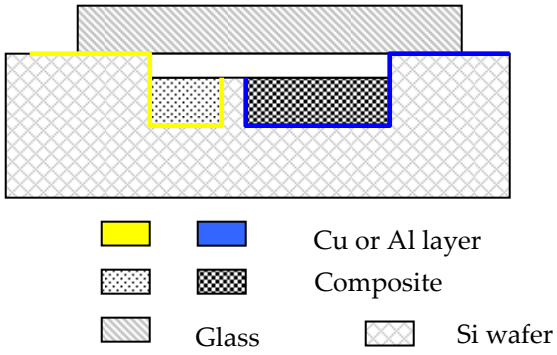

Figure 7.1 A side-by-side microbattery design used in Holladay (2001)

Alternatively, a layer-over-layer electrode design was adopted in order to reduce the transport resistance between the electrodes. The first design was to build the composite electrodes on separate Si wafers and then to bond the wafers to make microbatteries, as shown in Fig. 7.2. As the wafers were to be bonded using the front side surfaces, the electrical connections to the electrodes were made from the backside of substrates by thru-wafer vias. The electrolyte could be inserted into the cells before wafer bonding, or after bonding thru the vias. Efforts were made to implement this design; however, a number of technical challenges were encountered. The most significant problem was the presence of a liquid or gel-polymer electrolyte, which appeared to be incompatible with the wafer bonding process. Temperatures as low as 200-250 °C were reported in wafer bonding (Radu et al. 2005); however, the liquid or gel-polymer electrolyte will not be stable at those temperatures. It was also noticed that Kynar 741 PVDF polymer has a melting point of 168 °C (Kynar PVDF for lithium batteries, Elf Altchem technical brochure), which excluded the possibility of bonding wafers first and then filling with electrolyte as the

PVDF polymer in the composite electrode on the wafers will melt at the high temperature. Therefore, it was decided to not proceed with this design.

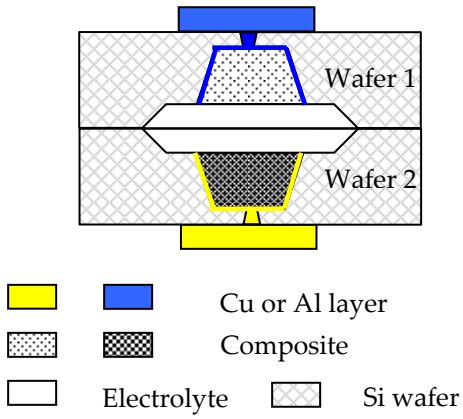

Figure 7.2 A layer-over-layer Si wafer based microbattery design

Since fabricating electrodes on separate wafers was not successful, it appeared that both electrodes had to be built on the same Si wafer. To build microbatteries on a single wafer, both electrodes would need to be fabricated in the same receptacle, separated by a layer of separator. Experiments were performed to test the feasibility of this approach.

The electrode receptacle was fabricated by coating and patterning a layer of photosensitive epoxy (SU-8 25, MicroChem Inc., Newton, MA). A schematic diagram of the fabrication procedure is shown in Fig. 7.3, showing the following steps to fabricate the cathode as the first electrode:

(a) Evaporative coating of Al onto an oxidized wafer;

(b) Spin-coating of the photosensitive epoxy onto the wafer;

(c) Patterning of the epoxy layer to create electrode receptacles;

(d) Screen-printing the composite cathode slurry into the receptacles to make thick-film cathodes, which were dried at elevated temperature under vacuum.

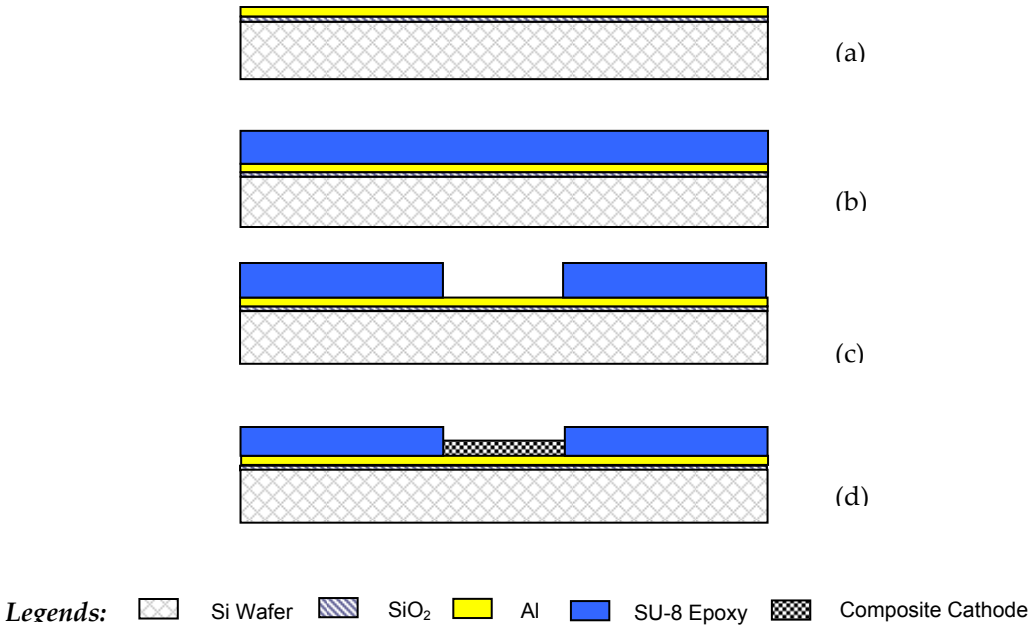

Figure 7.3 A schematic fabrication process of a composite cathode on a Si wafer

In these experiments, these "microcathodes" had an area of c.a. 4.0 x 10.0 mm^2. Following fabrication of the cathodes, they were tested using the following procedure:

i. Two pieces of Celgard 2400 separator film were placed on top of the cathode;

ii. A lithium electrode with Cu foil current collector was placed on the separator film;

iii. A piece of polypropylene (PP) film was used to cover both the lithium anode and separators;

iv. The edges of the PP film were sealed with hot glue, with the tab of Cu current collector uncovered;

v. Liquid electrolyte was injected into the cell with a syringe;

vi. The filling hole on the PP film was sealed with hot glue.

In initial tests it was found that the liquid electrolyte leaked slowly from the cell, and cell performance degraded in a manner strongly associated with the leakage. Therefore, liquid

electrolyte was periodically added into the cell to maintain a sufficient level and minimize the effect of leakage to the testing results.

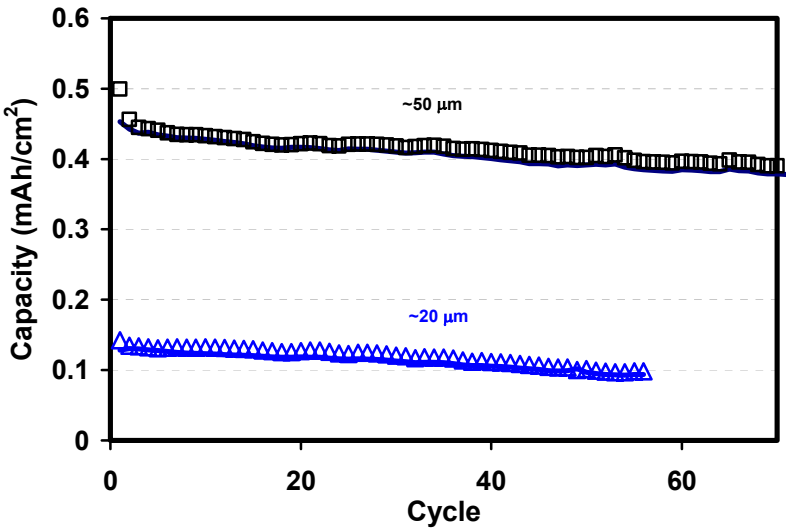

Figure 7.4 0.5 C rate cycling performance of two microcathodes (symbols: charge, lines: discharge)

The voltage profiles observed for these uncompressed CNT cathodes on Si wafer were similar to those of the 4 cm^2 CNT-cathode. Figure 7.4 shows the 0.5 C rate cycling performance of two cathodes with a composite film thickness of ~20 µm and ~50 µm, respectively. These cathodes cycled well at about 90 % of theoretical capacities and a fade rate of 0.2 %/cycle, slightly higher than that observed for these microcathodes. The higher fade rate was concluded to be the result of the continuous electrolyte leakage and solvent evaporation, which led to a higher salt concentration in the electrolyte and a poorer ionic conductivity. Precipitated salt was observed along the edges that the electrolyte leaked from the cell. The internal resistance of these cells was in the range of 30-80 ohm/cm^2, comparable to that of the macro cathodes. These results indicated that these microfabricated cathodes performed similar to the large cathodes.

These microcathodes had limited area specific capacities due to the small film thicknesses (20-50 μm), which was limited by the depth of the wells (about 100-150 μm). As shown in Chapter 4, the cathode should be built with a thickness of 85-100 μm with a capacity of 0.8-1.0 mAh/cm^2. However, attempts to increase cathode film thickness were not successful, since thicker composite films severely cracked and peeled-off from the substrate. The cause was identified to be the smoothness of the Si wafers, which resulted in poor adhesion between the Al layer and the composite film. Without improving the composite film thickness, it was expected that the microcathodes would not be able to provide the power needed by the proposed microbattery.

Nevertheless, it was found that a gel-polymer electrolyte solution could be applied on dried cathodes and gelled under vacuum to remove the solvent in the solution; the resulting cathode and gel-polymer electrolyte assemblies were tested without a separator film because the gel-polymer electrolyte was in place. The 0.5 C rate cycling performance of these cells was comparable to that shown in Fig. 7.4, indicating that the gel-polymer electrolyte performed at about the same level as liquid electrolyte at 0.5 C rate.

However, major technical challenges were encountered when the composite anode was made on the above assembly of cathode and gel-polymer electrolyte. The fabrication process is schematically shown in Fig. 7.5 (continued from Fig. 7.3):

(e) A layer of polymer electrolyte solution was applied on top of dried cathode and then gelled under vacuum;

(f) Composite anode slurry was screen-printed on top of the gel-polymer electrolyte and dried under vacuum;

(g) The anode current collector was applied onto the anode.

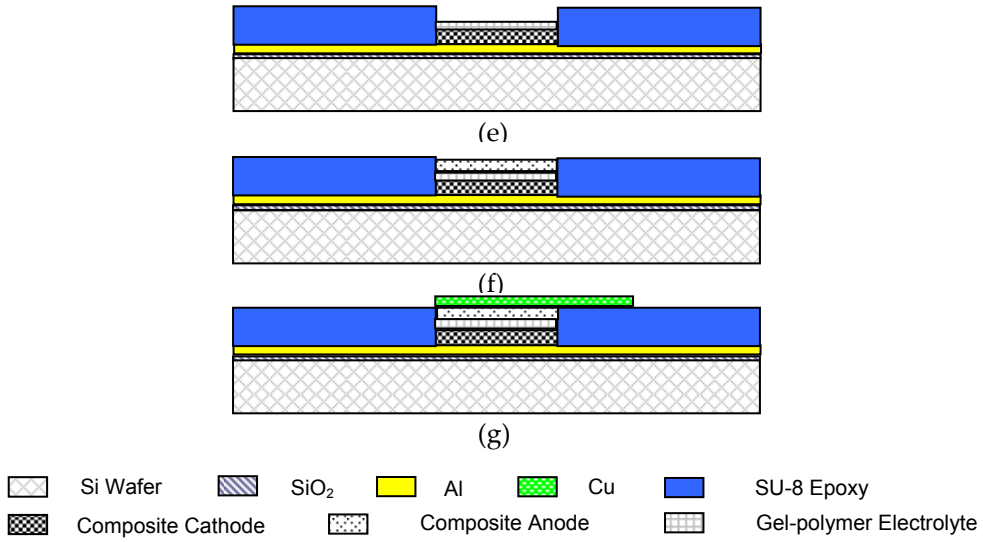

Figure 7.5 A schematic fabrication process of gel-polymer electrolyte and anode for a layer-over-layer microbattery using Si wafers (continued from Fig. 7.3)

The technical difficulty was encountered in Step (g). At first a layer of Cu (about 1 μm thick) was evaporated onto the surface of the anodes as the current collector; however, the Cu film was found to be too thin to provide electrical connection for the porous composite film and the cells showed no capacity. Other conductive materials, e.g. conductive epoxy, were tried to overcome the above problem. However, the conductive epoxy was found to be chemically unstable in lithium-ion batteries and could not be used as a current collector. As a result, there was no success in getting a working lithium-ion cell.

Hence, the microbattery fabrication using silicon wafers was unsuccessful in this study. The side-by-side design was concluded in the previous study to be unable to provide the power required by this project and not investigated in this study; two layer-over-layer designs were investigated in this study, but were unsuccessful. The first layer-over-layer design was hindered by technical challenges with the wafer bonding process, and the second design was limited by the difficulty of coating a sufficiently thick composite cathode and making a current collector for

the composite anodes. The lesson learned from these experiments was that the substrates for the composite microbatteries should have the properties that would facilitate bonding or sealing, and that the current collectors should provide sufficient adhesion for thick composite electrodes to achieve the required cell performance.

7.2 POLYPROPYLENE FILM BASED METHOD

The second substrate investigated in this study was a polypropylene (PP) film. The PP film was considered since it is transparent, which may help in the alignment of electrodes fabricated on separate substrates; it is bondable at temperatures below 100 °C; its surface is rougher than that of Si wafers, which should be beneficial to improve the roughness of the current collector and enhance the adhesion to the composite electrodes. These properties appeared attractive for use of PP films as the substrate to implement a microbattery with a layer-over-layer electrode layout.

The PP films used in this study had a thickness of c.a. 50 μm, with sufficient stability in the liquid electrolyte, acidic and basic solutions. Initial experiments showed that the liquid electrolyte did not leak from pouches of heat bonded bare PP films; however, the evaporation coated thin metal layers on the PP films would lose continuity across the sealing line as the PP films deformed during heat sealing. Therefore, additional Cu foil slices (25 μm thick) were placed on thin-film current collector across the sealing line to ensure good electrical connections and 5-minute epoxy was used to seal the areas around the slices. The battery design is shown in Fig. 7.6.

The cells were fabricated by the following procedure:

a) Al or Cu was coated onto PP films by E-beam evaporation;

b) The metal films were patterned to make current collectors;

c) Composite slurries were screen-printed onto the current collectors;

d) The electrodes were dried under vacuum;

e) The electrodes were stacked with Celgard® 2325 separator;

f) Two slices of Cu foil were placed at the current collectors across the sealing line, liquid electrolyte was injected and the cell was sealed with the pulse heat sealer. In some cases, a heat sealable polymer film (same packaging film used in large cells) was used as a secondary package.

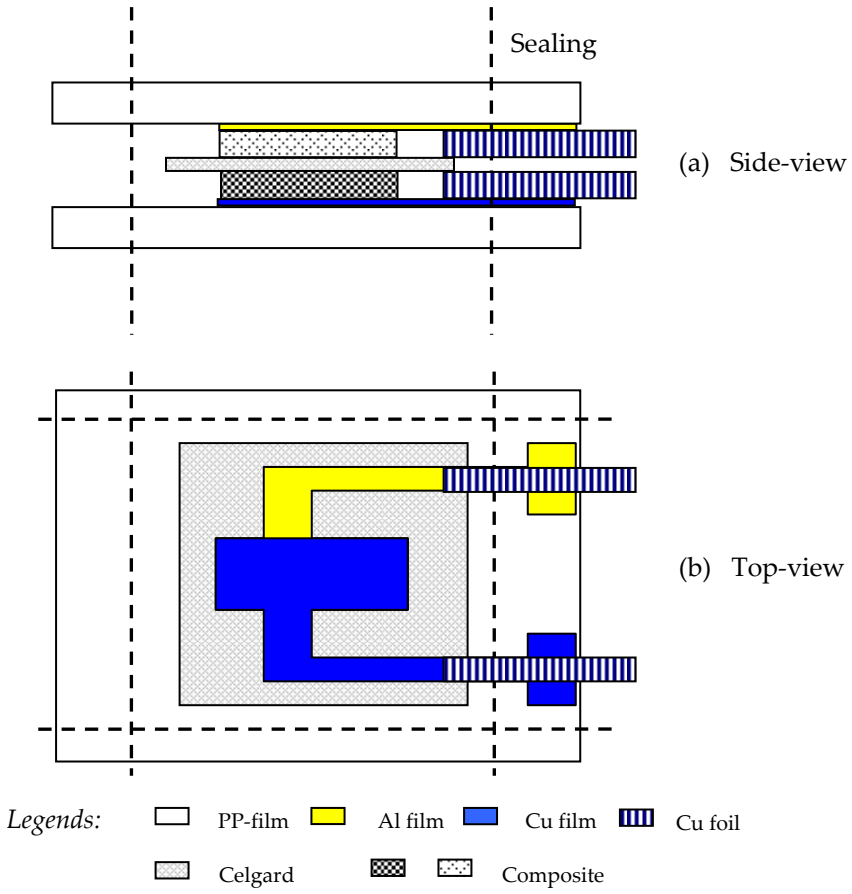

Figure 7.6 PP-film based microbattery design (not to scale)

A cut anode is shown in Figure 7.7. The effective electrode area was 0.4 cm^2, which was on the same order of magnitude as that intended for the next generation (0.1 cm^2, target area of microbattery). The thicknesses of dry cathode and anode films were about 60 and 20 μm, respectively, to balance the electrode capacities (as detailed in Chapter 6). Figure 7.8 shows the half C-rate cycling performance. It can be seen that after about 300 full depth discharge cycles, the microbattery retained above 70 % of its starting capacity, demonstrating a good cycle life expectancy. The starting capacity was 0.63 mAh/cm^2, which was higher than that of the cathodes built on Si wafers (see Fig. 7.4); however, it was much lower than those of the macro cells (see Fig. 6.7) and the macro cathodes (see Fig. 4.16). Efforts to increase the electrode thickness to improve the cell capacity were unsuccessful, as composite cathode thicker than 60 μm would severely crack and peel off.

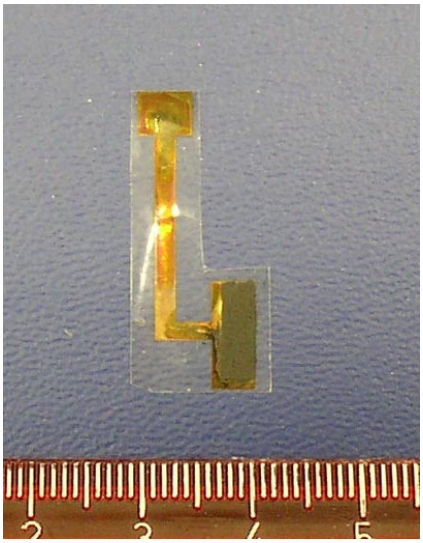

Figure 7.7 Image of a cut anode on PP-film

Figure 7.9 shows the cycling performance at various C-rates of up to 16 C. It can be seen that, for this particular battery, the 8 C discharge performance was acceptable (which delivered about 46 % of the starting capacity); however, at the 16 C rate (which corresponded to 10 mA/cm^2

and 28 mW/cm^2), the cell only delivered 2-3 % of the starting capacity, significantly smaller than the reported value (~30 %) in Neudecker et al. (2000). It is also worth mentioning that in another test, the above cell successfully went through 2000 pulse discharge cycles, with each pulse lasting 0.5 sec at 4 mA (10 mA/cm^2).

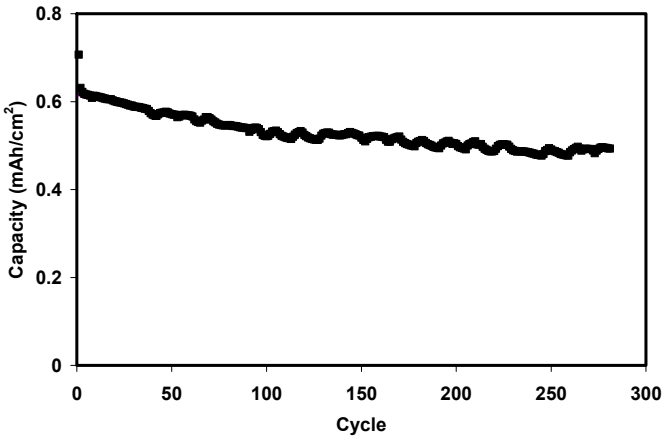

Figure 7.8 0.5 C cycling performance of a microbattery built on PP-films

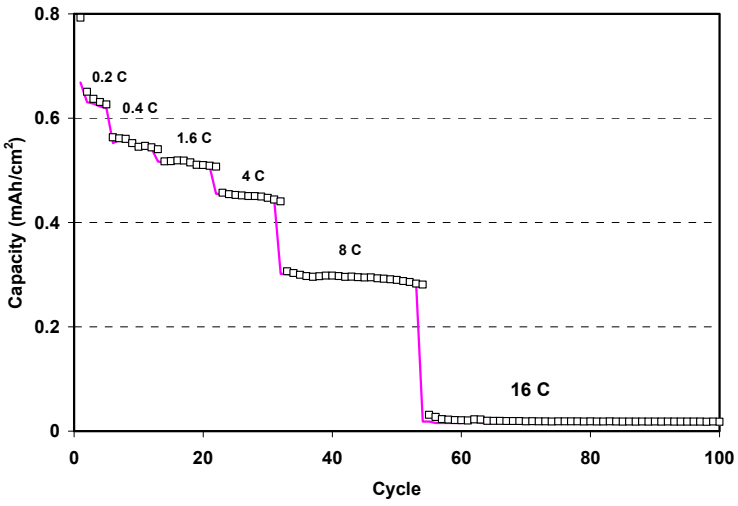

Figure 7.9 Power performance of a PP-film based microbattery (refer to Fig. 4.1 for legend use)

The inferior performance of the PP-film based cell at the 16 C rate was due to a large internal resistance (~1200 Ω-cm^2, compared to about 40 Ω-cm^2 of the testing cells of macro

cathodes). The poor adhesion between the composite cathodes and the current collectors was a major cause of the large cell resistance, as the composite cathodes on PP films were very easily scraped off with a razor blade, while the macro cathodes on Al foils were not. Therefore, contrary to the original hope that the use of PP films would improve the adhesion of composite electrodes (as compared to Si wafers), the improvement was insufficient to achieve the desired electrode thickness and good contact between composite layer and current collector.

Efforts were made to roughen the PP film surface to improve the adhesion; however, no significant success was achieved. When the film was roughened slightly with reactive ion etching (RIE, DEM-451 Anelva Corporation), the roughness gained seemed to be negated by the current collector coating (about 1 μm thick, by E-beam evaporator); when the film was mechanically roughened (with 220-400 grit sand papers), it was not possible to coat a usable current collector on the resultant PP film. Therefore, improvements to the PP-film-based battery did not succeed and no effort was made to shrink the battery size to that of the proposed microbattery.

Although the PP-film-based batteries did not achieve the desired power level, they demonstrated the feasibility of using plastic substrate based methods to implement the proposed microbattery. In particular, electrode fabrication, cell assembly and sealing in presence of liquid electrolyte were greatly facilitated with PP film substrates, and the layer-over-layer design was implemented. The integration of Si-based microsensors and plastic-based microbatteries may require different assembly techniques than those currently adopted in semiconductor industry.

The investigation documented in this section also indicated that at least two aspects of the plastic film based battery needed improvement: the adhesion between the composite layer and current collector, and the heat stability of the plastic substrates. These issues need to be solved before microbatteries using plastic substrates can become a commercially feasible.

7.3 COC-FILM-BASED METHOD

The results in the previous two sections showed that obviously the PP film was more successful than the Si wafer as a microbattery substrate in this study. Therefore, further development focused on finding a plastic film with the proper properties to be used as a battery substrate. It was found that Topas® Cyclic Olefin Copolymer (COC) film has following characteristics (from the Topas COC technical brochure at www.ticona.com), making itself a potentially better candidate than a PP-film for the substrate in this microbattery study:

- Improved film stiffness over polypropylene films;
- High barrier to water vapor and low water absorption;
- High melting point in the range of 240-300 °C ;
- Heat bondable with a glass transition temperature in the range of 80-180 °C;
- Resistant to hydrolysis, polar organics acid and bases;
- Good adhesion for metallization without pretreatment;
- Electrically insulating with a dielectric constant of about 2.35.

COC film samples were obtained from Ticona (Florence, KY), and were highly transparent films with a thickness of c.a. 125 μm. It was experimentally verified that the COC films sealed well against the liquid electrolyte. A heat sealed COC film pouch (c.a. 4 cm^2), which contained a Celgard film between two pieces of COC films, did not show any leakage of the liquid electrolyte it contained for a period of one week. It was also verified that the COC film was stable in the liquid electrolyte as a piece of COC film did not show any visual change and any mass change after one week soaking in the liquid electrolyte.

From the results of this study, it appeared that the composite electrodes built on metal foils had much better adhesion than those built on evaporated metal films; therefore, metal foils were

used in the microbattery design using COC film as a battery substrate. The design is illustrated in Fig. 7.10. The COC films were used both as electrode substrates and as the sealing material. The electrical connections to the current collectors were made by thru vias, so that no metal would extrude from the sealing lines and the possibility of liquid leakage along the sealing lines was minimized.

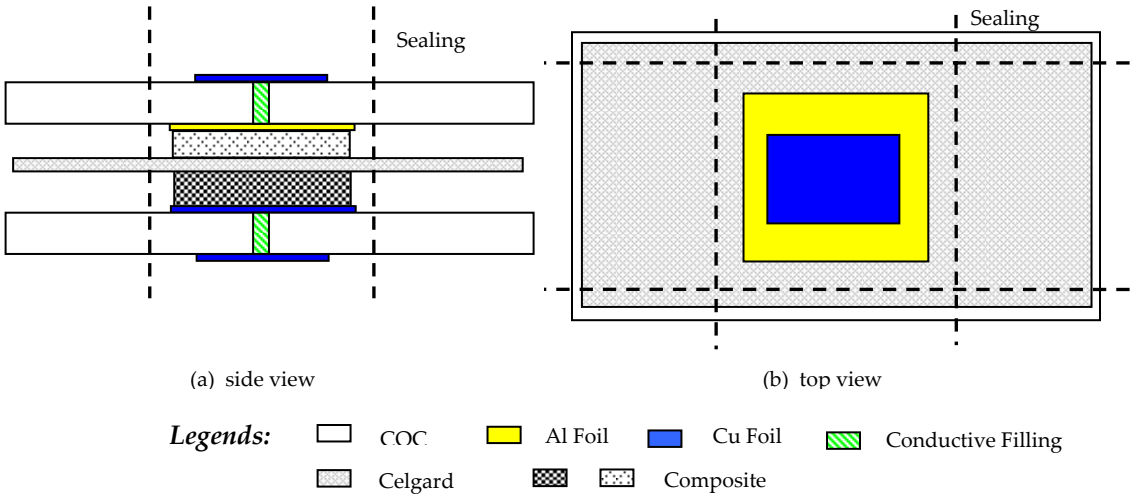

Figure 7.10 COC film based microbattery design

This design was implemented with the following procedure, which is shown schematically in Fig. 7.11:

(a) Thru holes were made on the COC films;

(b) Al or Cu foils were coated and patterned on the front side of the COC films, and conductive epoxy or solder was filled into the thru holes;

(c) Electrical connections on the backside of the films were coated and patterned, connecting to the conductive filling in the thru holes;

(d) Composite cathodes were screen printed onto the current collectors and dried;

(e) An anode film (made separately following step a-d), Celgard separator and a cathode film were aligned and stacked;

(f) The film stack was heat sealed along three lines, leaving the final edge unsealed;

(g) A proper amount of liquid electrolyte was injected into the above film stack;

(h) The film stack was allowed to stand for at least one hour, and then it was hand pressed to force the gas out of the stack and sealed along the final line and between the cells.

Most steps in the above procedure can be carried out with IC compatible processes. Step (a) can be done by anisotropic polymer etching (e.g. Reactive Ion Etcher), although in this study a cheaper and yet effective mechanical punching was adopted (such a technique has been used to make thru-film connections for polymer IC devices in DeJule 1998). In step (b), metal foil coating on COC films was attached by heat laminating (at 120-170 °C), and the patterning could be done by photolithography; it was actually done with a razor blade in this study. In step (c), the holes could be filled with electroplating, but were filled with soldering. In step (f), the sealing could be done with ultrasonic bonding (Devine, 2001), but was done by heat sealing. In step (g) the electrolyte filling could be done after the cell stack had been evacuated; however, evacuation was omitted because such an equipment was unavailable. The fact that manual techniques were used to implement this procedure does not imply that this procedure was limited to these techniques.

Two generations of microbatteries were fabricated in this study. The major difference between these two generations of batteries was the size of current collectors, which were c.a. 4 mm x 10 mm and 3 mm x 3 mm, respectively. The size of the composite electrodes was c.a. 2 mm x 2 mm for both generations. The first and second generations of microelectrodes and microbatteries are shown in the Figure 7.12 and 7.13. The thicknesses of screen masks for the cathodes and anodes were c.a. 200 and 90 μm, and the thicknesses of dried cathode and anode films were around 95 and 40 μm, respectively. Note that the cell volume was significantly larger

than the volume occupied by the current collectors, since the available heat sealer (Impulse Sealer Tish 200, Electronic Heating Equipment Co.) required a clearance of about 3 mm from the edge of the current collectors. Therefore, there was excess amount of liquid electrolyte in each microbattery, which may have been beneficial to the cell performance.

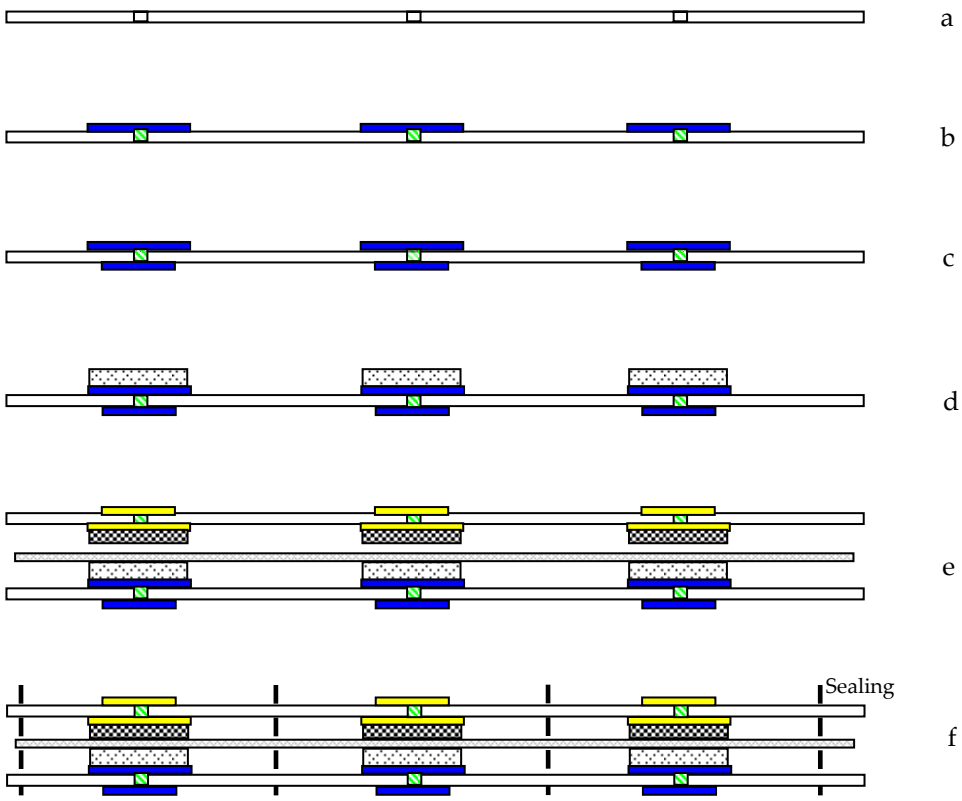

Figure 7.11 Fabrication procedure of the COC film based microbattery (Legends see Fig. 7.10)

The fabrication yield of microbatteries was about 50 %, which would be improved as the process is automated. The probability was greater than 92 % for discharge capacities of different cells to be smaller than 0.024 mAh/cm^2 at various rates (data to be shown in Fig. 7.16). Therefore, there was virtually no difference in the performance between of these two generations of microbatteries. This was interpreted as the result of a minimal effect to the battery performance

due to the different sizes of current collectors. Therefore, no distinction is made on the generation of the microbatteries when their performance is described in the following sections.

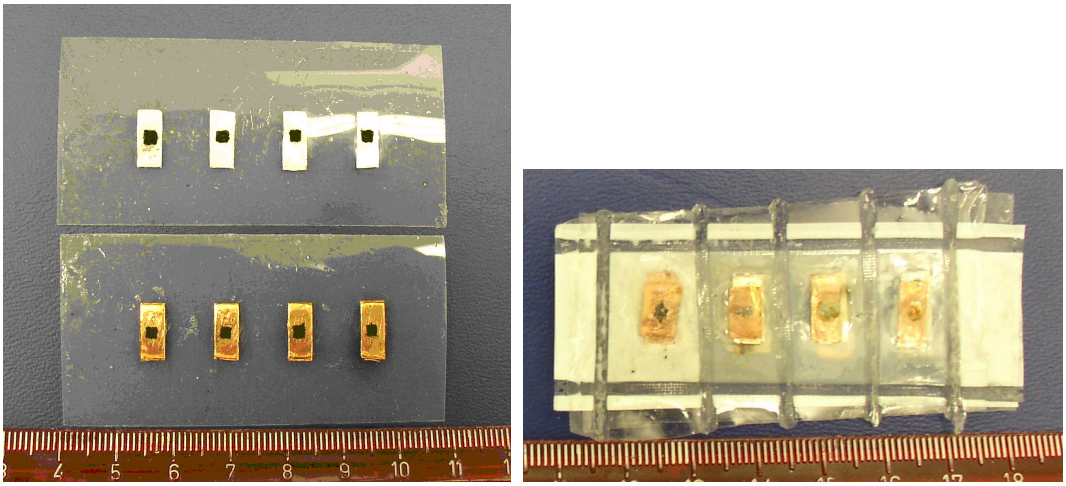

Figure 7.12 The first generation microelectrodes and sealed microbatteries

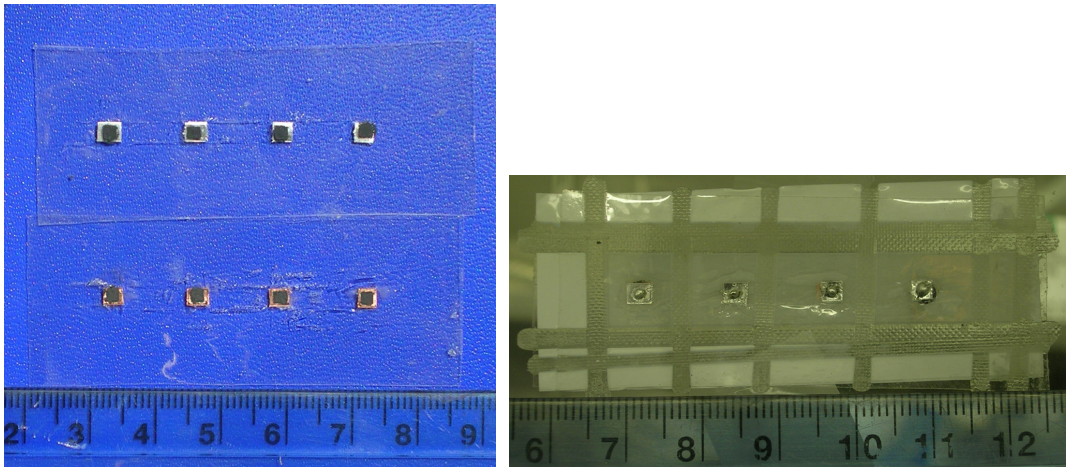

Figure 7.13 The second generation microelectrodes and sealed microbatteries

The microbatteries were successfully activated following the procedure listed in Chapter 6. The activation process did not produce any noticeable amount of gas. The microbattery capacities after activation were in the range of 0.025-0.04 mAh per cell (corresponding to 0.63-1.0 mAh/cm^2, close to that of the macro cathodes shown in Fig. 4.16). 100 % DOD constant rate

cycling tests were performed at discharge rates from 0.5 C to 20 C (with a 0.5 C charge rate). Figure 7.14 shows typical voltage profiles for a microbattery discharged at 0.5 and 10 C rates, which were similar to those of 4 cm^2 batteries except that the voltage of the microbattery was slightly lower. Figure 7.15 shows the cycling performance of a microbattery at 0.5 C 100 % DOD cycling. After more than 160 cycles, the microbattery retained more than 75 % of its starting capacity. As it was expected that the microbatteries would be cycled in the proposed power supply at much shallower depths of discharge, the cycle life expectancy should be much longer.

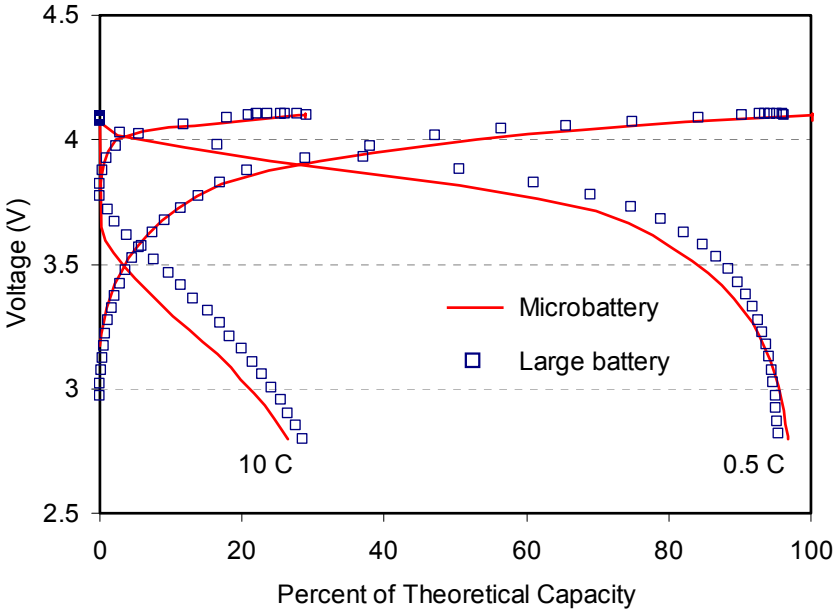

Figure 7.14 Comparison of voltage profiles between a microbattery and a large battery

The rate performance of these microbatteries, at 100 % DOD discharges, is shown in Fig. 7.16. It can be seen that these microbatteries delivered about 0.18 mAh/cm^2 at 10 mA/cm^2 (per electrode area, corresponding to 28 mW/cm^2 based on ending cell voltage), and about 0.04 mAh/cm^2 at 20 mA/cm^2 (56 mW/cm^2). This demonstrated that these microbatteries were capable to deliver the power needed by the autonomous microsensors (50 mW/cm^2, see chapter 1). This

graph also shows that the two generations of microbatteries had very similar power performance, indicating the size of current collectors imposed no effect on the cell performance.

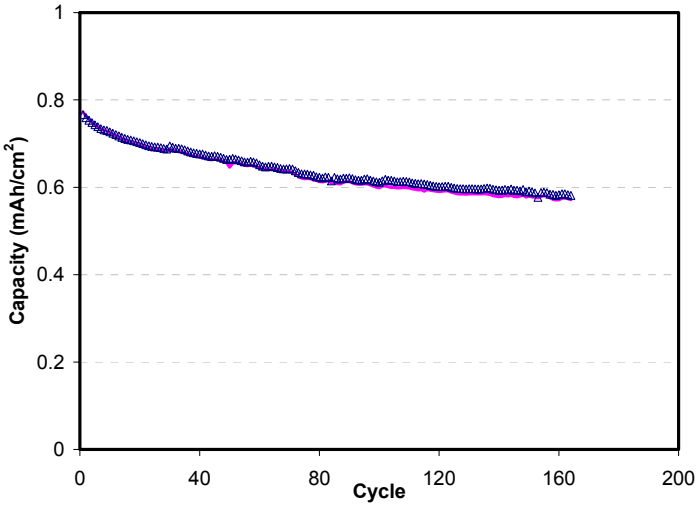

Figure 7.15 0.5 C rate cycling performance of a microbattery (refer to Fig. 4.1 for legend use)

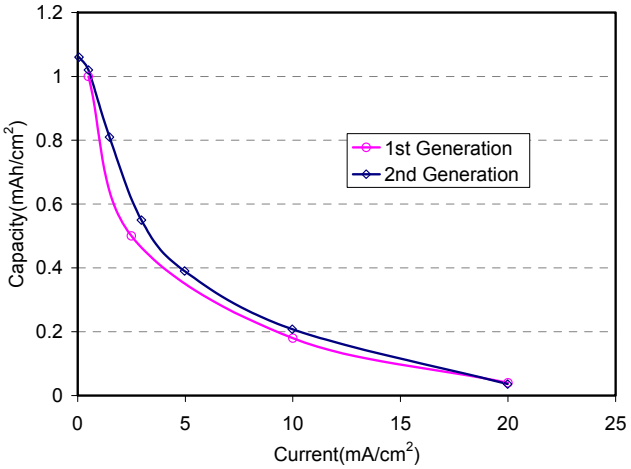

Figure 7.16 Power performance of COC-film based microbatteries at 100 % DOD discharge

A cycling test simulating a microsensor duty cycle was also performed. In this test, a microbattery was first charged to 4.10 V and then pulse discharged; between the pulse discharges, the microbattery was charged at 0.5 C-rate back to 4.10 V. Figure 7.17 shows the voltage and current profiles of duty cycles of 100 ms long 1.2 mA pulses. The depth of discharge

of such a duty cycle was about 0.13 %. Each microbattery provided about 3.5 mW (87 mW/cm^2) power during these pulses. When the battery voltage was allowed to drop to 2.84 V, a current of 1.6 mA (4.5 mW) could be drained from these microbatteries, corresponding to a current density of 40 mA/cm^2 and a power density >110 mW/cm^2. These tests demonstrated that the COC-film based microbatteries had the capability to deliver pulse power significantly higher than the requirement. Over 12,000 such duty cycles were demonstrated, and the change of the average cell voltage during pulses is shown in Figure 7.18. It can be seen that the voltage was stable in the first 6000 cycles and only decreased slightly afterwards, indicating the cell could be continually cycled.

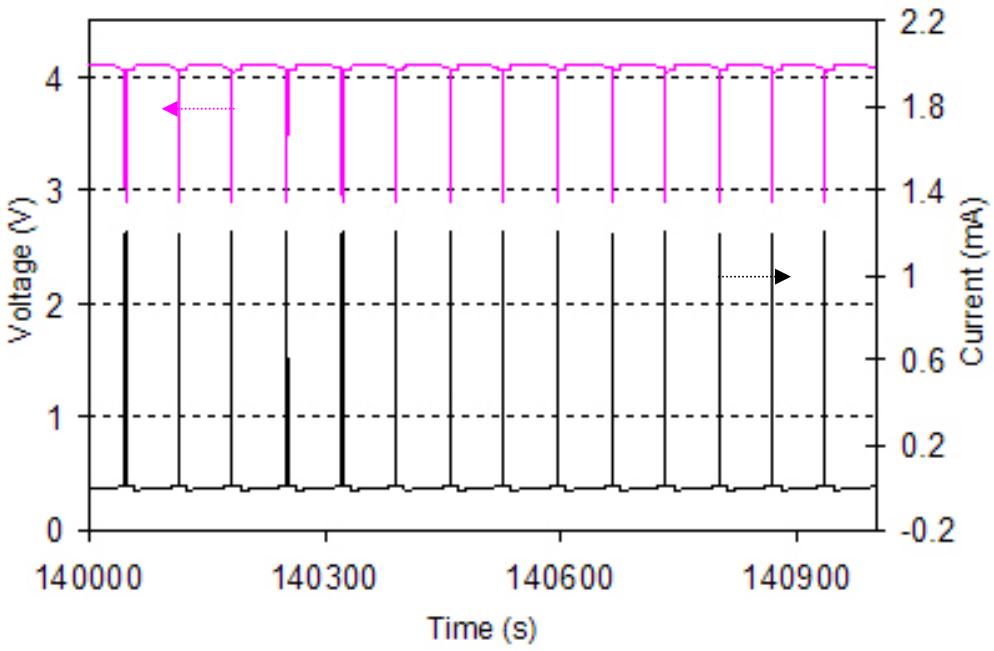

Figure 7.17 Duty cycle testing of a 0.025 mAh microbattery
(upper: voltage profile; bottom: current profile)

A second type of pulse discharge test was also performed on COC-film based microbatteries. In this test, a microbattery was taper-charged to 4.10 V, and then discharged at a 0.5 C rate; during this discharge process, a 100 ms 0.8 mA pulse discharge (corresponding to

power density of 70 mW/cm^2 when the average voltage is 3.5 V) was drained out of the battery every 20 seconds. These pulses simulated the intermitted high power active operations of the autonomous microsensors that would be separated by longer periods of low power operations. In the test shown in Fig. 7.19, the microbattery delivered 297 pulses before reaching the cut-off voltage (2.85 V in this case), showing the capability of the microbattery to deliver a significant number of high power pulses before needing a recharge. The microbattery was then charged at 0.5 C rate to 4.10 V, as shown in Fig. 7.20. About 28 % of the theoretical capacity was utilized during this pulse discharge process. The significant deeper depth of discharge than that of the constant rate discharge (see Fig. 7.16) was concluded to be the effect of the 20-second 0.5 C rate discharge between the pulses, which allowed redistribution of lithium in the cells.

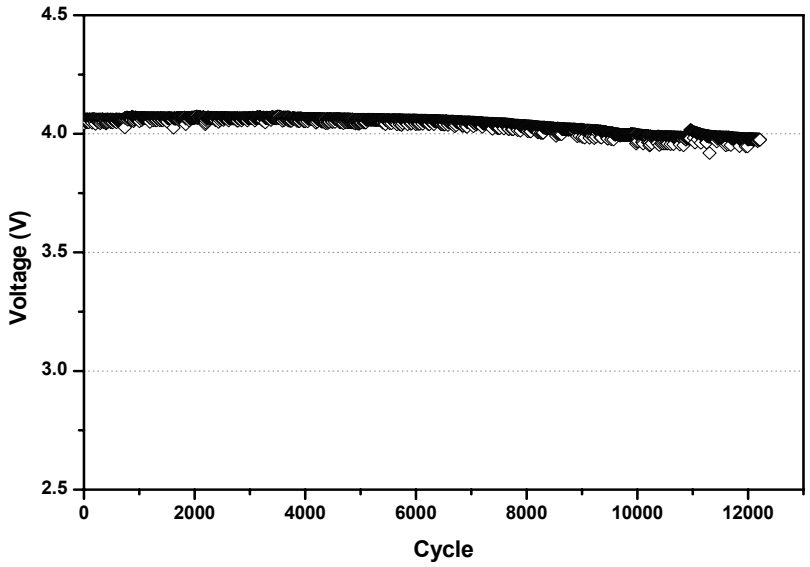

Figure 7.18 Change of average cell voltage during pulse discharges

The COC-film based microbatteries were successfully made and tested; however, due to the limited time and resources these microbatteries are still in early development stages, and some improvements are needed. As mentioned earlier in this section, the fabrication procedure was

largely manual, although the feasibility of the battery was demonstrated. Should an ultrasonic bonding machine or a heat sealer that requires much smaller clearance be available, the microbatteries could be sealed with space about the same size as the current collectors. In addition, the COC film is an excellent water vapor barrier; however, it is still permeable to O_2 and CO_2 (from the Topas COC technical brochure at www.ticona.com). Therefore, the COC films by themselves could not provide a hermetic seal and the microbatteries were tested in the glove box. It was expected that a layer of evaporative-coated aluminum film on the outer side of the COC films would provide a sufficiently hermetic seal for the microbatteries. Such aluminum coating was found in the heat sealable polymer film used in large cell packages, which effectively eliminated the penetration of H_2O, O_2, and CO_2 into the cells.

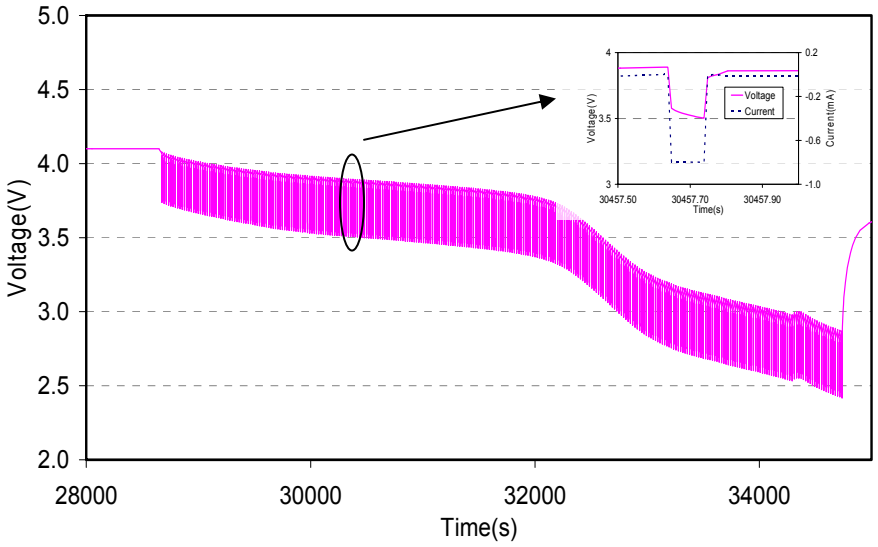

Figure 7.19 Voltage and current profiles of a COC-film based microbattery in a second pulse discharge test

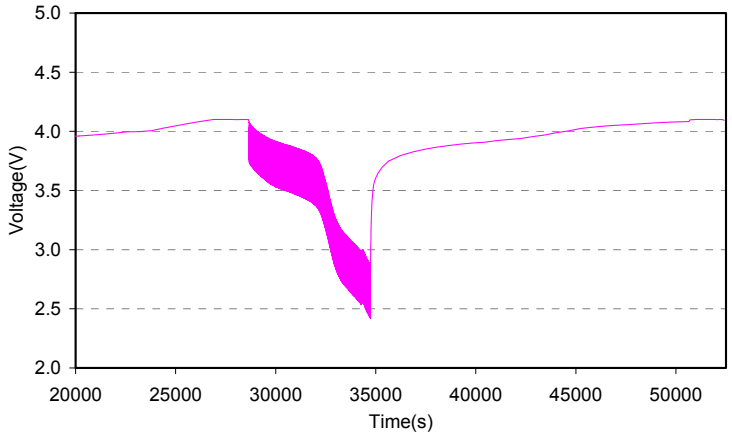

Figure 7.20 Voltage profile of a COC-film based microbattery in a second pulse discharge test

7.4 SUMMARY

In this chapter, three types of substrates were tested in order to fabricate a high power microbattery. The composite cathode and gel-polymer electrolyte were successfully demonstrated with Si wafer substrates; however, no complete cell was successfully made. Microbatteries were demonstrated with the polypropylene film substrates; however, the power performance did not meet requirements due to poor adhesion between the current collector and the composite electrode limited the material loadings, and the thermal stability of the PP-films was not sufficient. Microbatteries built on COC-film substrates were proven to be the most successful ones in this study, demonstrating a good cycle life expectancy and a power capability which met requirements.

The COC-film based microbatteries had electrode area of c.a. 2.0 mm x 2.0 mm, nominal capacities of 0.025-0.04 mAh/cell (0.63-1.0 mAh/cm^2). Constant rate discharge tests were performed at rates up to 20 mA/cm^2 (100 % DOD), and pulse discharges were performed with pulses up to 1.6 mA (40 mA/cm^2, or 110 mW/cm^2), demonstrating power capabilities surpassing that of the thin-film solid state microbatteries reported in Neudecker et al. (2000). Two types of

pulse discharge tests were carried out, in the first test the microbatteries were recharged after every pulse discharge and in the second test the microbatteries were pulse-discharge cycled until the cell voltage dropped to the cut-off voltage. The results showed that the microbatteries had a good pulse cycle life expectancy and could provide a significant number of pulse discharges before needing to be recharged.

CHAPTER 8: CONCLUSIONS AND RECOMMENDATIONS

The objective of this project was to build a high-power lithium-ion microbattery for use in power supplies for autonomous microsensors and similar applications. This was accomplished using a Cyclic Olefin Copolymer (COC)-film based method. The microbatteries used $LiAl_{0.14}Mn_{1.86}O_4$ and MCMB as active materials for the cathode and anode, respectively; liquid state $LiPF_6$ /EC /DEC electrolyte was used with Celgard separator films. A layer-over-layer electrode layout was implemented. The COC-films were used as both the substrate and primary sealing materials, and patterned metal foils were used as the current collectors.

Composite thick-film cathodes used single-walled carbon nanotubes (SWNTs) as the conductive additive, which significantly reduced the internal resistance relative to that observed for cathodes which used a carbon black (CB) additive. Consequently the power performance of the cathodes was substantially improved even though no compression was applied to the electrodes. Therefore, the need for compression was eliminated, which facilitated microbattery fabrication. Optimized uncompressed macro CNT-cathodes (85-100 μm, 12 wt% SWNTs, and 2.6 wt% PVDF) were capable of delivering power at a level greater than 50 mW/cm^2, adequate to meet the peak power needs of the targeted microsystems. The energy density (based on electrode area) also met the desirable value of 8.5 J/cm^2 for a 0.1 cm^2 microbattery, which was estimated on the basis of reserve capacity for a hybrid micropower system (10 μW for 12 hours, Harb et al. 2002).

The composite anodes contained 90 wt% MCMB, 5 wt% multi-walled carbon nanotubes (MWNTs) and 5 wt% PVDF, and had significantly better power performance than the CNT-

cathodes. The MWNTs were used in the anode based their superior performance than super P carbon black that was previously used. The impact of activation on the performance of the composite anodes (and the lithium-ion batteries) was investigated, and a C-rate based activation procedure was developed and proven to be suitable for the 4 cm^2 lithium-ion batteries of this study.

The COC-film based microbatteries had electrode area of c.a. 2 mm x 2 mm, and nominal capacities of 0.025-0.04 mAh/cell (0.63-1.0 mAh/cm^2, corresponding to energy density of ~6.3-10.1 J/cm^2). The variation in cell capacities was a result of the variance in electrode thickness from cell to cell during fabrication. These batteries were able to deliver constant currents up to 20 mA/cm^2 (100 % depth of discharge, corresponding to power density of 56 mW/cm^2), substantially higher than that of the thin-film solid state microbatteries. These microbatteries also delivered pulse currents up to 40 mA/cm^2 (corresponding to power density of 110 mW/cm^2). Two types of pulse discharge tests were carried out. In the first type, the microbatteries were taper-charged to 4.1 V after every pulse discharge (at 1.2 mA for 100 ms) and the microbattery delivered over 12,000 pulses and the average cell voltage during a pulse only decreased slightly. The depth of discharge of each pulse was about 0.13 %. In the second test, the microbatteries were pulse-discharged (at a somewhat lower current level of 0.8 mA for 100 ms) once every 20 seconds superimposed on a constant rate discharge at 0.5 C (1.4 μA, corresponding to ~5.8 μW at 4.1 V) until the cell voltage dropped to the cut-off voltage. The cell delivered nearly 300 pulses, and the depth of discharge for this multi-pulsed discharge process was about 28 %. This depth of discharge was higher than that observed for a constant rate discharge at the same level (0.8 mA), which was due, at least in part, to the relaxation of concentration gradients during the lower rate discharge between pulses.

The mechanism by which the single-walled carbon nanotubes improved the rate performance of composite cathodes was studied both experimentally and theoretically. The measurements showed that the electronic conductivities of the uncompressed CNT-cathodes were lower than those of compressed CB-cathodes, and relaxation experiments indicated no significant difference in the ionic transport between these two types of cathodes. Numerical simulations using Newman's dualfoil model (Doyle et al. 1993, Fuller et al. 1994, Doyle and Newman et al. 1996) also indicated that the electronic conductivity and porosity did not limit the performance of the CNT-cathodes. The simulation results also indicated that the uncompressed CNT-cathodes had a significantly lower "film resistance". As the same active material and electrolyte were used in these two types of electrodes, the difference in the "film resistance" should reflect the difference in electronic contacts to the active material particles in the different cathodes. These better contacts facilitate electron conductance to these particles and improve their accessibility to the electrode reactions. Therefore, it was concluded that the use of SWNT in the composite cathodes improved battery performance by improving the electronic contacts to active material particles. Hence, the active material particles were more accessible to the electrode reactions, which consequently improved the rate capability of the composite cathodes.

This study contributed to lithium battery research in at least two ways. The first contribution was an understanding of the role of various types of resistances in the rate performance of the composite cathode, showing that composite film electronic conductivity and electrolyte ionic conductivity were not limiting, and most likely the electronic access to active material particles was limiting the rate performance of the composite cathode. The importance of electronic contacts to the electrode performance has been recognized (Thomas et al. 2002); however, no effective method has been implemented to characterize and reduce it. By using two types of carbon additives, SWNT and CB, this study offered some insights into the contact

resistance in the composite electrodes. Due to the difference in morphology, the fibrous SWNTs have better capability than the particulate CB to establish electronic accesses to the active material particles.

Although use of SWNTs as the conductive additive was effective in improving cathode performance, the improvement comes at a cost. The use of SWNT in microbatteries can be justified as the material cost is generally a small fraction of the cost of the microdevices. However, the use of SWNT in large cells is impractical due to its cost and it may be desirable to use materials that have similar characteristics in place of SWNT. Ideally, replacement materials should be compatible with lithium battery systems, have good conductivity and high aspect ratios. Results also indicated that it is preferable to use replacement materials with length comparable to the size of the active material.

The second contribution was the development of a plastic-substrate-based method to implement a thick-film composite microbattery that meets both the peak power and energy density requirements of the autonomous microsensors. A truly 0.1 cm^2 (based on electrode area) microbattery can be created for the hybrid power supply proposed in Harb et al. (2002) using the recipe and procedure developed in this study. By using a Cyclic Olefin Copolymer film as the battery substrate, a layer-over-layer electrode layout was implemented in a microbattery that uses a liquid electrolyte. Cu and Al foils were used as current collectors, and the electrode thickness was comparable to that in the 4 cm^2 cells (~100 μm), which is more than an order of magnitude greater than that of the thin-film electrodes, leading to higher material loadings. All these factors, combined with the high-power cathode and anode, contributed to the good performance of the microbattery. The successful implementation of the lithium-ion thick-film microbattery represents a step closer to the realization of a complete wireless microsensing system. Although the power density achieved in this study was somewhat lower than that in a

previous study (Humble et al. 2001, Humble and Harb 2003), the COC-based microbatteries developed in this study had several advantages over the Ni/Zn microbatteries, including a higher working voltage, a higher energy density, a better capacity retention and a longer cycle life. Use of a flexible plastic substrate is also likely to afford some unique integration possibilities for autonomous microsystems.

There are several opportunities for future work that are related to this project:

1. The fabrication procedure implemented in this study proved the feasibility of making COC-film based microbatteries. Demonstration of practical, high-volume assembly based on this work remains to be accomplished;
2. The cycle testing and pulse testing results are very promising. Different types of duty cycle testing remains to be done to investigate the capability of the microbatteries to handle various tasks;
3. The microbatteries need to be integrated with solar cells and controlling circuitry to make a micro power supply. Strategies for integrating plastic batteries with other system components need to be explored;
4. The microbatteries in this study were tested in a glove box because the COC film is oxygen permeable. A comparative test should be carried outside the glove box to verify the impact of oxygen on the cell performance. It was envisioned that coating an Al layer on the external sides of battery could effectively inhibit the oxygen penetration. Such a technique needs to be investigated and integrated into the microbattery fabrication;
5. Methods for fabricating microbatteries in a patternable way should be investigated, which allow connecting batteries into arrays (series or parallel) that may be more useful in some power supplies.

REFERENCES

Ahn, S., High Capacity, High Rate Lithium-Ion Battery Electrodes Utilizing Fibrous Conductive Additives, *Electrochemical and Solid-State Letters*, **1**(3), 111-113 (1998).

Aurbach, D. M. D. Levi, E. Levi, H. Telier, B. Markovsky, G. Salitra, U. Heider and L. Hekier, Common Electroanalytical Behavior of Li Intercalation Processes into Graphite and Transition Metal Oxides, *J. Electrochem. Soc.*, **145**(9), 3024-3034 (1998).

Aurbach, D. Y., Talyosef, B. Markovsky, E. Markevich, E. Zinigrad, L. Asraf, J. S. Gnanaraj, H.-J. Kim, Design of electrolyte solutions for Li and Li-ion batteries: a review, *Electrochim. Acta,* **50**, 247–254 (2004).

Aurbach, D., I. Weissman, A. Zaban, P. Dan, On the role of water contamination in rechargeable Li batteries, *Electrochim. Acta,* **45**, 1135 -1140 (1999).

Aurbach,, D. B., Markovsky, I. Weissman, E. Levi, I. Ein-Eli, *Electrochim. Acta* , **45**, 67 (1999).

Aurbach, D., Levi M. D., et al. Common Electroanalytical Behavior of Li Intercalation Processes into Graphite and Transition Metal Oxide, *J. Electrochem. Soc.*, **145**(9), 3024-3034 (1998).

Baba, M., N. Kumagai, H. Kibayashi, O. Nakano, and K. Nishidate, Fabrication and Electrochemical Characteristics of All-Solid-State Lithium-Ion Batteries Using V_2O_5 Thin-films for Both Electrodes, *Electrochemical and Solid-State Letters*, **2**(7), 320-322 (1999).

Bates, J. B., Microbatteries and Microdevices, *202nd Meeting* - Salt Lake City, Utah, Electrochemical Society (2000).

Bates, J. B., D. Lubben et al., Thin-film Li-$LiMn_2O_4$ Batteries, *10th Annual Battery Conference on Applications and Advances*, Electrochemical Society (1995).

Bates, J. B., G. R. Gruzalski et al., Rechargeable Thin-Film Lithium Microbatteries, *Solid State Technology*, July 1993: 59-64 (1993).

BATT Program lithium-ion battery test protocol.

Brousse, T., D.M. Schleich, SnO_2 Thin-films as Possible Anodes for Li-Ion Batteries, *ECS Meeting Abtracts*, vol. **MA 97-2**, 91 (1997).

Broussely, M., P. Biensan, B. Simon, Lithium insertion into host materials: the key to success for Li ion batteries, *Electrochim. Acta*, **45**: 3 – 22 (1999).

Chen, R., Integration goes plastic, *Spie's oemagazine*, 24-26, November (2002).

Cheng, C. L., C. C. Wan and Y. Y. Wang, Preparation of porous, chemically cross-linked, PVdF-based gel polymer electrolytes for rechargeable lithium batteries, *J. Power Sources,* **134** (2), 202-210 (2004).

Cheng, X., A. M. Sastry, and B. E. Layton, *J. Engineering Materials and Technology*, **123**, 12-19 (2001).

Cheung, J. T., History and fundamentals of pulsed laser deposition, in "*pulsed laser deposition of thin films*", John Wiley and Sons (1994).

Cho, J., G. B. Kim, H. S. Lim, C.-S. Kim and S. I. Yoo, Improvement of Structural Stabilibty of $LiMn_2O_4$ Cathode Material on 55'C cycling by Sol-Gel Coating of $LiCoO_2$, *Electrochemical and Solid-State Letters*, **2**(12), 607-609 (1999).

Claye AS, Fischer JE, Huffman CB, et al., Solid-state electrochemistry of the Li single wall carbon nanotube system, *J. Electrochem. Soc.,* **147** (8): 2845-2852 (2000).

Das, N. C., T. K. Chaki, and D. Khastgir, Conductive rubbers made by adding conductive carbon black to EVA, EPDM, and EVA–EPDM blends, *Plastics, Rubber and Composites*, **30** (4), 162-169 (2001).

Deab, J. A., *Lange's Handbook for Chemistry*, New York, McGraw-Hill Book Company (1979).

DeJule, R., All-Polymer Integrated Circuits-Plastics can mean low-cost processing of low-end devices, *Semiconductor International*, April (1998)

Devine, J., Ultrasonic Plastic Welding Basics, technical article from *SonobondUltrasonic.com* (2001).

Doyle M.., J. Newman, A. S. Gozdz, C. N. Schmutz, and J.-M. Tarascon, Comparison of Modeling Predictions with Experimental Data from Plastic Lithium Ion Cells, *J. Electrochem. Soc.*, **143**, 1890 (1996).

Doyle, M., T. F. Fuller, and J. Newman, *J. Electrochem. Soc.*, **140**, 1526 (1993).

Drury, C. J., C. M. J. Mutsaers, C. M. Hart, M. Matters, and D. M. de Leeuw, Low-cost all-polymer integrated circuits, *Applied Physics Letters*, **73**, 1 (1998).

Dudney, N. J., J. B. Bates, R. A. Zuhr, S. Young, J. D. Robertson, H. P. Jun, and S. A. Hackney, Nanocrystalline $Li_xMn_{2-y}O_4$ Cathodes for Solid-State Thin-Film Rechargeable Lithium Batteries, *J. Electrochem. Soc.*, **146**(7), 2455-2464 (1999).

Fix, W. A. Ullmann, J. Ficker, and W. Clemens, Fast polymer integrated circuits, *Applied Physics Letters*, **81**(9), 1735-1737 (2002).

Fonseca,C., P. S. Neves, the usefulness of a $LiMn_2O_4$ composite as an active cathode material in lithium batteries, *J. Power Sources,* **135,** 249–254 (2004).

Forró, L., and C. Schönenberger, carbon nanotubes, materials for the future, *Europhysics News,* **32** (3), (2001).

Fuhrer, M. S., M. Forero, A. Zettl, P. L. McEuen, Ballistic Transport in Semiconducting Carbon Nanotubes, *Electronic Properties of Molecular Nanostructures,* edited by H. Kuzmany et al., American Institute of Physics (2001).

Fuller, T. F., M. Doyle, and J. Newman, *J. Electrochem. Soc.*, **141**(1), 1 (1994).

Fuller, T. F., M. Doyle, and J. Newman, Relaxation phenomena in Lithium-ion-insertion cells, *J. Electrochem. Soc.*, **141**(4), 982-990 (1994).

Garcia, R. E., Y.-M. Chiang, W. C. Carter, P. Limthongkul, and C. M. Bishop, Microstructural Modeling and Design of Rechargeable Lithium-Ion Batteries, *J. Electrochem. Soc*., **152**(1), A255-A263 (2005).

Gelinck, G. H., T. C. T. Geuns, and D. M. de Leeuw, High-performance all-polymer integrated circuits, *Applied Physics Letters*, **77**, 10 (2000).

Ghiurcan, G. A. , C.-C. Liu, A. Webber, and F. H. Feddrix, Development and Characterization of a Thick-Film Printed Zinc-Alkaline Battery, *J. Electrochem. Soc.*, **150** (7), A922 (2003).

Guohua L., H. Ikuta, T. Uchida, and M. Wakihara, The Spinel Phases $LiM_yMn_{2-y}O_4$ (M = Co, Cr, Ni) as the Cathode for Rechargeable Lithium Batteries, *J.Electrochem. Soc.*, 178-182 (1996).

Gustafson et al., *U. S. Patent* 6,451,480 (2002).

Hamano et al., *U. S. Patent* 6,458,483 (2002).

Harb, J. N., LaFollette, R. M., R. H. Selfridge, L. L. Howell, Microbatteries for Self-Sustained Hybrid Micropower Supplies, *J. Power Sources*, **104,**46-51 (2002).

Hariharan, V., *U. S. Patent* 20020160253 (2002).

Holladay, J., *Li-Ion Microbatteries for MEMS*, master's thesis, Brigham Young Univ., Provo, UT (2000).

Holladay, J., P. Humble, J. Harb, R. LaFollette, L. Salmon, R. Barksdale, B. Anderson, Ni/Zn and Li-Ion Rechargeable Microbatteries for MEMS Applications, *ECS Meeting Abstracts*, vol. **MA 99-1**, 8 (1999).

Hossain, S., Y.-K. Kim, Y. Saleh, R. Loutfy, Comparative Studies of MCMB and C-C Composite as Anodes for Lithium-Ion Battery Systems, *J. Power Sources*, **114,** 264-276 (2003).

Humble, P. H., *The development of Nickel-Zinc Microbatteries for Use in Autonomous Micro Devices*, Ph. D. Dissertation, Brigham Young Univ., Provo, UT (2002).

Humble, P. H., and J. N. Harb, Optimization of Nickel-Zinc Microbatteries for Hybrid Powered Microsensor Systems, *J. Electrochem. Soc.*, **150** (9), A1182-A1187 (2003).

Humble, P.H., J.N. Harb, and LaFollette, R.M., Microscopic Nickel-Zinc Batteries for use in Autonomous Microsystems, *J. Electrochem. Soc.*, **148** (12), A1357-A1361 (2001).

Iijima,S., *Nature,* **354**, 56 (1991).

Jarman, T., *Effect of Particle Size and Preparing Methods on the Performance for Cathode of Li-ion Batteries*, master's thesis, Brigham Young Univ., Provo, UT (2000).

Jones S. D., J. R. Akridge, Development and performance of a rechargeable thin-film solid-state microbattery, *J. Power Sources*, **54** (1): 63-67 (1995).

Julien, C. and G. –A. Nazri, Materials Design and Optimization, *Solid State Batteries*, Boston, Kluwer Academic Publishers (1994).

Julien, C.M., Lithium intercalated compounds Charge transfer and related properties, *Materials Science and Engineering R*, **40**, 47–102 (2003).

Kanamura, K., A. Goto, J.-i. Hamagami, T. Umegaki, Electrophoretic Fabrication of Positive Electrodes for Rechargeable Lithium Batteries, *Electrochemical and Solid-State Letters*, **3**(6), 259-262 (2000).

Kane, C. L., E. J. Mele, R. S. Lee, J. E. Fischer, P. Petit, H. Dai, A. Thess, R. E. Smalley, A. R. M. Verschueren, S. J. Tans and C. Dekker, *Europhysics Letters*, **41**(6), 683-688 (1998).

Kawai, H., M. Nagata, H. Tukamoto and A. R. West, A New Lithium cathode $LiCoMnO_4$: Toward Practical 5 V Lithium Batteries, *Electrochemical and Solid-State Letters*, **1**(5), 212-214 (1998).

Kim, D.-W, Y.-K. Sun, J.-H. Cho and S.-I. Moon, Novel Polymer Electrolytes for Rechargeable Lithium-Ion Polymer batteries, *Electrochemical and Solid-State Letters*, **2**(6), 256-258 (1999).

Kim, J. S., W. Y. Yoon, Improvement in lithium cycling efficiency by using lithium powder anode, *Electrochim. Acta,* **50,** 531–534(2004).

Koeneman, P. B., I. J. Busch-Vishniac et al., Feasibility of Micro Power Supplies for MEMS, *J. Microelectromechanical Systems*, **6**(4), 355-362 (1997).

Kostecki, R., BATT quarter report, *http://berc.lbl.gov/BATT/BATTquarterly5-04.pdf,* May (2004).

Kuwabata, S., S. Masui, H. Yoneyama, Charge-discharge properties of composites of $LiMn_2O_4$ and polypyrrole as positive electrode materials for 4 V class of rechargeable Li batteries, *Electrochim. Acta*, **44**, 4593-4600 (1999).

LaL A. and J. Blanchard, *http://www.spectrum.ieee.org/webonly/publicfeature/sep04/0904nuc.html* (2004).

Lazarraga, M. G., S. Mandal, J. Ibanez, J. M. Amarilla, J. M. Rojo, $LiMn_2O_4$-based composites processed by a chemical-route Microstructural, electrical, electrochemical, and mechanical characterization, *J. Power Sources,* **115**, 315–322 (2003).

Lee, C. Y. , H. M. Tsai, H. J. Chuang, S. Y. Li, P. Lin, and T. Y. Tseng, Characteristics and Electrochemical Performance of Supercapacitors with Manganese Oxide-Carbon Nanotube Nanocomposite Electrodes, *J. Electrochem. Soc.*, **152**, A716 (2005).

Lee, J.-K., S.-J. Lee, H.-K. Baik, H.-Y. Lee, S.-W. Jang, S.-M. Lee, Substrate Effect on the Microstructure and Electrochemical Properties in the Deposition of a Thin-film $LiCoO_2$ Electrode, *Electrochemical and Solid-State Letters*, **2**(10), 512-515 (1999).

Lei, J. , L. Li, R. Kostecki, R. Muller, and F. McLarnon, Characterization of SEI Layers on $LiMn_2O_4$ Cathodes with In Situ Spectroscopic Ellipsometry, *J. Electrochem. Soc.*, **152**, A774 (2005).

Li, Naichao Charles J. Patrissi, Guangli Che,a and Charles R. Martin, Rate Capabilities of Nanostructured $LiMn_2O_4$ Electrodes in Aqueous Electrolyte, *J. Electrochem. Soc.*, **147** (6), 2044-2049 (2000).

Linden, D., T. B. Reddy, *Handbook of batteries*, 3rd ed., McGraw-Hill Handbooks (2001).

Madou, M., *Fundamentals of Microfabriecation*, CRC press (1997).

Mandal, S., J. M. Amarilla, J. Ibanez, and J. M. Rojo, The role of carbon black in $LiMn_2O_4$-based composites as cathodes for rechargeable lithium batteries, *J. Electrochem. Soc.*, **148**(1), A24-29 (2001).

Mao, O., R. L. Turner, I. A. Courtney, B. D. Fredericksen, M. I. Buchett, L. J. Krause and J. R. Dahn, Active/Inactive Nanocomposites as Anodes for Li-Ion Batteries, *Electrochemical and Solid-State Letters*, **2**(1), 3-5 (1999).

Markovsky, B., M.D. Mikhail, D. Aurbach, *Electrochim. Acta*, **16/17**, 2287 (1998).

McGraw, J. M., C. S. Bahn, P. A. Parilla, J. D. Perkins, D. W. Readey, D. S. Ginley, Li ion diffusion measurements in V_2O_5 and $LiCo_{1-x}Al_xO_2$ thin-film battery cathodes, *Electrochim. Acta*, **45**, 187-196 (1999).

Meninger, S., *et al.*, Vibration-to-electric energy conversion, *IEEE Trans. VLSI Systems*, **9**(1), 64-76 (2001).

Mukhopadhyay, N., Hoshino, S. Kawasaki, F. Okino, W. K. Hsu, and H. Touhara, Electrochemical Li Insertion in B-Doped Multiwall Carbon Nanotubes, *J. Electrochem. Soc.*, **149** (1), A39-A44 (2002).

Murata, K., Izuchi, S., Yoshihisa, Y., An overview of the research and development of Solid Polymer Electrolyte Batteries, *Electrochim. Acta*, **45**, 1501-1508 (2000).

Myung, S.-T., S. Komaba, and N. Kumagai, Enhanced Structural Stability and Cyclability of Al-Doped $LiMn_2O_4$ Spinel Synthesized by the Emulsion Drying Method, *J. Electrochem. Soc.*, **148** (5), A482-A489 (2001).

Nagaura,T., K. Tozawa, *Prog. Batt. Solar Cells,* **9,** 209 (1990).

Neudecker, B. J., N. J., Dudney, and J. B. Bates, "Lithium-Free" Thin-Film Battery with In Situ Plated Li Anode, *J. Electrochem. Soc.*, **147**(2), 517-523 (2000).

Neudecker, B.J., R.A. Zuhr, J.B. Bates, Li-Ion Thin-Film Batteries with Nitride and Subnitride Anodes MeN_x (Me = Sn, In), *ECS Meeting Abtracts*, vol. **MA 99-2**, 160 (1999).

Neudecker, B.J., R.A. Zuhr, et al., Lithium Manganese Nickel Oxides, *J. Electrochem. Soc.*, **145**, 4160-4168 (1998).

Noddapaneni, N. and D. Ingersoll, *U. S. Patent* 5,567,401 (1996).

Ong, I. J. and J. Newman, A short pulse and relaxation of a lithium ion battery, Double-Layer Capacitance in a Dual Lithium Ion Insertion Cell, *J. Electrochem. Soc.*, **146** (12), 4360-4365 (1999).

Panero, S., G. Savo and B. Scrosati, Tin Oxide-Based Lithium-Ion Polymer-electrolyte cells, *Electrochemical and Solid-State Letters*, **2**(8), 365-366 (1999).

Park, Y-S., S-H. Lee, B-I. Lee, S-K. Joo, All-Solid-State Lithium Thin-Film Rechargeable Battery with Lithium Manganese Oxide, *Electrochemical and Solid-State Letters*, **2**(2), 58-59 (1999).

Patel, K. K., J. M. Paulsen, J. Desilvestro, Numerical simulation of porous networks in relation to battery electrodes and separators, *J. Power Sources*, **122**, 144-152 (2003).

Patrissi, C. J. and C. R. Martin, Improving the Volumetric Energy Densities of Nanostructured V_2O_5 Electrodes Prepared Using the Template Method, *J. Electrochem. Soc.*, **148** (11), A1247-A1253 (2001).

Patrissi, C. J. and C. R. Martin, Sol-Gel–Based Template Synthesis and Li-Insertion Rate Performance of Nanostructured Vanadium Pentoxide, *J. Electrochem. Soc.*, **146** (9) 3176-3180 (1999).

Perkins, J. D. , C. S. Bahn, J. M. McGraw, P. A. Parilla, and D. S. Ginley, Pulsed Laser Deposition and Characterization of Crystalline Lithium Cobalt Dioxide $LiCoO_2$ Thin Films, *J. Electrochem. Soc.*, **148**, A1302 (2001).

Puers, R., and W. Patrick, Adaptable Interface Circuits for Flexible Monitoring of Temperature and Movement, *Analog Integrated Circuits and Signal Processing*, 193-206 (1997).

Radu, I., M. Reiche, M. Gabriel, and M. Zoberbier, Low-Temperature Wafer Bonding via DBD Surface Activation, Abstract 520, *The electrochemical Society 207th meeting*, Quebec City, Canada, May (2005).

Ruetschi, P., Alkaline electrolyte- Lithium Miniature Primary Batteries, *J. Power Sources*, **7**, 165-180 (1980).

Russ, B. E., J. B. Talbot, An Analysis of the Binder Formation in Electrophoretic Deposition, *J. Electrochem. Soc.*, **145**(4), 1253-1256 (1998).

Ruth, D., all-polymer integrated circuit, Plastics can mean low-cost processing of low-end devices. *Semiconductor International*, April 1 (1998).

Ruzicka, B., L. Degiorgi, R. Gaal, L. Thien-Nga, R. Bacsa, J.-P. Salvetat, and L. Forro, *Physical Review B*, **61**, R2468 (2000).

Sakamoto, J. S. and B. Dunn, *J. Electrochem. Soc.*, **149**, A26-A30 (2002).

Sannier, L., R. Bouchet, S. Grugeon, E. Naudin, E. Vidal and J.-M. Tarascon, Room temperature lithium metal batteries based on a new Gel Polymer Electrolyte membrane, *J. Power Sources, **144**(1), 231-237,* (2005).

Scrosati B., Recent advances in lithium ion battery materials, *Electrochim. Acta*, **45**, 2461-2466 (2000).

Shin, H.-C., S.-I. Pyun, Investigation of Lithium Transport througn Lithium Cobalt Dioxide Thin Film Sputter deposited by Analysis of Cyclic Voltammogram, *Electrochim. Acta*, **46**, 2477-2485 (2001).

Shirahige M., Deyama S., Properties of Graphite and Progress in Graphite-related Technologies, *Hitachi Powdered Metals Technical Report*, No.3, 3-11 (2004).

Song, S.-W. , R. P. Reade, E. J. Cairns, J. T. Vaughey, M. M. Thackeray, and K. A. Striebel, Cu_2Sb Thin-Film Electrodes Prepared by Pulsed Laser Deposition for Lithium Batteries , *J. Electrochem. Soc.*, **151**, A1012 (2004).

Spires, T. and R. Malcolm Brown, "High Resolution TEM Observations of Single-Walled Carbon Nanotubes", *Jr. Department of Botany, The University of Texas at Austin,* Austin, Tx., 78713 (1996).

Strauss, E., D. Golodnitsky and E. Peled, Cathode Modification for Improved Performance of Rechargeable Lithium/Composite Polymer Electrolyte-Pyrite Battery, *Electrochemical and Solid-State Letters*, **2**(3), 115-117 (1999).

Striebel, K. A. , C. Z. Deng, S. J. Wen, and E. J. Cairns, Electrochemical Behavior of $LiMn_2O_4$ and $LiCoO_2$ Thin Films Produced with Pulsed Laser Deposition , *J. Electrochem. Soc.*, **143**, 1821 (1996).

Sukumar, V., M. Alahmad, K. Buck, H. Hess, H. Li, D. Cox, F. N. Zghoul, J. Jackson *et al.,* Switch array system for thin film lithium microbatteries , *J. Power Sources,* **136**, 401–407 (2004).

Tarascon, J. M., and D. Guyomard, The $Li_{1+x}Mn_2O_4$/C Rocking-Chair System: A Review, *Electrochim. Acta*, **38** (9), 1221-1231(1993).

Thess, A., R. Lee, P. Nikolaev, H. Dai, P. Petit, J. Robert, C. Xu, Y. H. Lee, S. G. Kim, A. G. Rinzler, D. T. Colbert, G. Scuseria, D. Tománek, . E. Fischer, R. E. Smalley, "Crystalline Ropes of Metallic Carbon Nanotubes", *Science,* **273**, 483 (1996).

Thomas, K. E., J. Newman, R. M. Darling, Mathematical modeling of lithium batteries, *Advances in Lithium-Ion Batteries*, Edited by W. van Schalkwijk and B. Scrosati, Kluwer Academic/Plenum Publishers (2002).

Tirado, J.L., Inorganic materials for the negative electrode of lithium-ion batteries: state-of-the-art and future prospects ,*Materials Science & Engineering R-Reports,* **40** (3), 103-136 (2003).

Wang, C.-W., K. A. Cook, and A. M. Sastry, *J. Electrochem. Soc.*, **150**, A385-A397 (2003).

Wang, C. S. A. J. Appleby, and F. E. Little, *J. Electroanal. Chem.*, **497**, 33 (2001).

Wang, C., T. Sakai, et al., All solid-state lithium-polymer battery using a self-cross-linking polymer electrolyte, *J. Electrochem. Soc.*, **150**(9), A1166-A1170 (2003).

Wang, C.-W., Y.-B. Yi, A. M. Sastry, J. Shim, and K. A. Striebel, Particle Compression and Conductivity in Li-Ion Anodes with Graphite Additives, *J. Electrochem. Soc.*, **151 (**9), A1489-A1498 (2004).

Wang, Y., J. Wu, F. Wei., *Carbon*, **41**, 2939–2948(2003).

Warneke, B., K.S. J. Pister, Exploring the Limits of System Integration with Smart Dust, *ASME International Mechanical Engineering Congress & Exhibition, Symposium on MEMS*, New Orleans, Nov. 17-22 (2002).

Wartena, R., A. E. Curtright, C. B. Arnold,A. P., K. E. Swider-Lyons,Li-ion microbatteries generated by a laser direct-write method, *J. Power Sources*, **126,** 193–202 (2004).

Warneke, B.A., K.S.J. Pister, An Ultra-Low Energy Microcontroller for Smart Dust Wireless Sensor Networks, *Int'l Solid-State Circuits Conf. 2004, (ISSCC 2004)*, San Francisco, Feb. 16-18 (2004).

West, W.C., J. F. Whitacre, V. White and B. V. Ratnakumar, Fabrication and testing of all solid-state microscale lithium batteries for microspacecraft applications, *J. Micromechanics and Microengineering*, **12**, 58-62 (2002).

Wise, K. D., *Integrated microsystems: merging MEMS, micropower electronics, and wireless communications*: **xxii-xxviii** (2000).

Wolf, S. and R. N Tauber, *Silicon Processing for the VLSI Era*, vol **1** process technology, 2nd edition, Lattice Press (2000).

Wright, R.B., Motloch C.G., Belt J.R., Christophersen J.P., Ho C.D., Richardson R.A., Bloom I., Jones S.A., Battaglia V.S., Henriksen G.L., Unkelhaeuser T., Ingersoll D., Case H.L., Rogers S.A., Sutula R.A., Calendar- and cycle-life studies of advanced technology development program generation 1 lithium-ion batteries , *J. Power Sources*, **110** (2), 445-470 (2002).

Xia, Y. and Whitesides, G. M., *Soft Lithography*, Ed.Angrew. Chem. Int., vol. **37**, 550-575 (1998).

Xing, X., J.M. Smith, Li-ion and/or Li-ion polymer battery with shielded leads, *U. S. Patent* 6,475,674 (2002).

Yang, J., M. Wachtler, M. Winter, and J. O. Besenhard, Sub-Microcrystalline Sn and Sn-Sn/Sb powders as Lithium Storage materials for Lithium-ion Batteries, *Electrochemical and Solid-State Letters*, **2**(4), 161-163 (1999).

Zaghib, K., P. Charest, A. Guerfi, J. Shim, M. Perrier, K. A. Striebel, Safe Li-ion polymer batteries for HEV applications, *J. Power Sources*, **134,** 124–129 (2004).

Zhou L. X., J. M. Kahn, K. S. J. Pister**,** Corner-cube retroreflectors based on structure-assisted assembly for free-space optical communication, *J. MICROELECTROMECHANICAL SYSTEMS*, **12** (3): 233-242 (2003)

APPENDIX A: TEST SCHEDULES

A.1 CATHODE TESTING SCHEDULE

	Step Label	Number Of Limits	Control Type	Control Value	Extra Control Value 1	Extra Control Value 2	Current Range	Extended Definition	Extended Definition 1
	OCP	2	Rest						
	Log Limit	**Step Limit**	**Goto Step**	**Type1**	**Sign1**	**Value1**	**Type2**	**Sign2**	**Value2**
1	☒	☒	Next Step	PV_CHAN_Step_Time	>=	00:01:00			
2	☒	☐		DV_Time	>=	00:00:10			
	charge_half	4	C-Rate	0.5			Low		
	Log Limit	**Step Limit**	**Goto Step**	**Type1**	**Sign1**	**Value1**	**Type2**	**Sign2**	**Value2**
1	☒	☐	Next Step	PV_CHAN_Voltage	>=	4.3			
2	☒	☐		DV_Time	>=	00:10:00			
3	☒	☐		DV_Voltage	>=	0.05			
4	☒	☒	End Test	PV_CHAN_Current	>=	0.5			
	taper	5	Voltage(V)	LL_CHAN_Voltage			Low		
	Log Limit	**Step Limit**	**Goto Step**	**Type1**	**Sign1**	**Value1**	**Type2**	**Sign2**	**Value2**
1	☒	☒	Next Step	PV_CHAN_Current	<=	2e-005			
2	☒	☒	Next Step	PV_CHAN_Voltage	>=	4.35			
3	☒	☐		DV_Time	>=	00:10:00			
4	☒	☐		DV_Current	>=	5e-005			
5	☒	☒	End Test	PV_CHAN_Current	>=	0.5			
	Rest1	3	Rest						
	Log Limit	**Step Limit**	**Goto Step**	**Type1**	**Sign1**	**Value1**	**Type2**	**Sign2**	**Value2**
1	☒	☒	Next Step	PV_CHAN_Step_Time	>=	00:00:05			
2	☒	☐		DV_Time	>=	00:00:02			
3	☒	☐		DV_Voltage	>=	0.001			
	Discharge1	4	C-Rate	-0.1			Low		
	Log Limit	**Step Limit**	**Goto Step**	**Type1**	**Sign1**	**Value1**	**Type2**	**Sign2**	**Value2**
1	☒	☒	Next Step	PV_CHAN_Voltage	<=	3.3			
2	☒	☒	Next Step	PV_CHAN_Step_Time	>=	00:00:20			
3	☒	☐		DV_Time	>=	00:00:05			
4	☒	☐		DV_Voltage	>=	0.05			
	IR	2	Internal Resistance	Amp:-5e-005	ms:2.00	Offset:0	Low		
	Log Limit	**Step Limit**	**Goto Step**	**Type1**	**Sign1**	**Value1**	**Type2**	**Sign2**	**Value2**
1	☒	☒	DischargeHalf	PV_CHAN_Step_Time	>=	00:00:00	PV_CHAN_Cycle_Inde	<=	5
2	☒	☒	Discharge5C	PV_CHAN_Step_Time	>=	00:00:15	PV_CHAN_Cycle_Inde	<=	15
	DischargeHalf	3	C-Rate	-0.5			Low		
	Log Limit	**Step Limit**	**Goto Step**	**Type1**	**Sign1**	**Value1**	**Type2**	**Sign2**	**Value2**
1	☒	☒	relax	PV_CHAN_Voltage	<=	3.3			
2	☒	☐		DV_Time	>=	00:05:00			
3	☒	☐		DV_Voltage	>=	0.05			
	Discharge5C	3	C-Rate	-5			Medium		
	Log Limit	**Step Limit**	**Goto Step**	**Type1**	**Sign1**	**Value1**	**Type2**	**Sign2**	**Value2**
1	☒	☒	relax	PV_CHAN_Voltage	<=	3.3			
2	☒	☐		DV_Time	>=	00:05:00			
3	☒	☐		DV_Voltage	>=	0.05			
	relax	3	Rest						
	Log Limit	**Step Limit**	**Goto Step**	**Type1**	**Sign1**	**Value1**	**Type2**	**Sign2**	**Value2**
1	☒	☒	Next Step	PV_CHAN_Step_Time	>=	00:10:00			
2	☒	☐		DV_Time	>=	00:02:00			
3	☒	☐		DV_Voltage	>=	0.001			
	Increment	2	Set Variable(s)	Reset	Increment	Decrement			
	Log Limit	**Step Limit**	**Goto Step**	**Type1**	**Sign1**	**Value1**	**Type2**	**Sign2**	**Value2**
1	☒	☒	End Test	PV_CHAN_Cycle_Inde	>=	16			
2	☒	☒	charge_half	PV_CHAN_Cycle_Inde	<=	15			
	rest_end	3	Rest						
	Log Limit	**Step Limit**	**Goto Step**	**Type1**	**Sign1**	**Value1**	**Type2**	**Sign2**	**Value2**
1	☒	☒	End Test	PV_CHAN_Step_Time	>=	00:10:00			
2	☒	☐		DV_Time	>=	00:02:00			
3	☒	☐		DV_Voltage	>=	0.05			

A.2 MICROBATTERY ACTIVATION SCHEDULE

	Step Label	Number Of Limits	Control Type	Control Value	Extra Control Value 1	Extra Control Value 2	Current Range	Extended Definition	Extended Definition 1
	OCP	2	Rest						
	Log Limit	**Step Limit**	**Goto Step**	**Type1**	**Sign1**	**Value1**	**Type2**	**Sign2**	**Value2**
1	☒	☒	Next Step	PV_CHAN_Step_Time	>=	05:00:00			
2	☒	☐		DV_Time	>=	00:10:00			
	1stCharge	4	C-Rate	0.05			Low		
	Log Limit	**Step Limit**	**Goto Step**	**Type1**	**Sign1**	**Value1**	**Type2**	**Sign2**	**Value2**
1	☒	☒	Next Step	PV_CHAN_Step_Time	>=	02:00:00			
2	☒	☐		DV_Time	>=	00:05:00			
3	☒	☐		DV_Voltage	>=	0.005			
4	☒	☒	Next Step	PV_CHAN_Voltage	>=	4.1			
	rest1	3	Rest						
	Log Limit	**Step Limit**	**Goto Step**	**Type1**	**Sign1**	**Value1**	**Type2**	**Sign2**	**Value2**
1	☒	☒	Next Step	PV_CHAN_Step_Time	>=	04:00:00			
2	☒	☐		DV_Time	>=	00:10:00			
3	☒	☐		DV_Voltage	>=	0.005			
	2nd_charge	3	C-Rate	0.1			Low		
	Log Limit	**Step Limit**	**Goto Step**	**Type1**	**Sign1**	**Value1**	**Type2**	**Sign2**	**Value2**
1	☒	☒	Next Step	PV_CHAN_Voltage	>=	4.1			
2	☒	☐		DV_Time	>=	00:10:00			
3	☒	☐		DV_Voltage	>=	0.05			
	Rest2	3	Rest						
	Log Limit	**Step Limit**	**Goto Step**	**Type1**	**Sign1**	**Value1**	**Type2**	**Sign2**	**Value2**
1	☒	☒	Next Step	PV_CHAN_Step_Time	>=	00:30:00			
2	☒	☐		DV_Time	>=	00:05:00			
3	☒	☐		DV_Voltage	>=	0.005			
	Discharge	3	C-Rate	-0.1			Low		
	Log Limit	**Step Limit**	**Goto Step**	**Type1**	**Sign1**	**Value1**	**Type2**	**Sign2**	**Value2**
1	☒	☒	Next Step	PV_CHAN_Voltage	<=	2.8			
2	☒	☐		DV_Time	>=	00:05:00			
3	☒	☐		DV_Voltage	>=	0.05			
	rest_end	3	Rest						
	Log Limit	**Step Limit**	**Goto Step**	**Type1**	**Sign1**	**Value1**	**Type2**	**Sign2**	**Value2**
1	☒	☒	End Test	PV_CHAN_Step_Time	>=	02:00:00			
2	☒	☐		DV_Time	>=	00:10:00			
3	☒	☐		DV_Voltage	>=	0.02			

APPENDIX B: INPUT DATA FILE FOR DUAL-FOIL MODEL

An example of the values for input data file for the dual-foil model is tabulated below (Table B.1). Please see the program code, available at J. Newman's website, for further information of the parameters. Note that in this study, a MCMB anode was used in the model. This was due to the observation of an unrealistic voltage jump phenomenon observed in the model result when a lithium anode was used. It was thought that the model contained a numerical bug, which could not be eliminated by adjusting electrode parameters. The parameters of the MCMB anode were adjusted so that the overpotential of the anode was insignificant and the cell performance represented that of the composite cathodes.

Table B.1 Complete list of input parameters for the dual-foil model

Value	Parameter	Meaning
50	lim	limit on number of iterations
50.0d-06	h1	thickness of negative electrode (m)
75.d-06	h2	thickness of separator (m) (3 pcs of celgard 2400)
86.0d-06	h3	thickness of positive electrode (m)
25.d-06	hcn	thickness of negative current collector (m)
25.d-06	hcp	thickness of positive current collector (m)
30	n1	number of nodes in negative electrode(set=0 if in foil mode)
20	n2	number of nodes in separator
150	n3	number of nodes in positive electrode
298.0d0	T	temperature (K)
1000.d0	xi(1,1)	initial salt concentration (mol/m3)
0.99d0	x	initial stoichiometric parameter for neg. electrode (ignored if n1=0)
0.18d0	y	initial stoichiometric parameter for positive electrode
0.5d0	tmmax	maximum time step size (s)
0.0d0	vcut	cutoff potential
3.9d-6	dfs1	(ignored in Foil mode) diffusion coef. in negative solid (m2/s)
0.35d-15	dfs3	diffusion coef. in positive solid (m^2/s)
1.50d-06	Rad1	radius of negative particles (m) (ignored in Foil mode)
1.5d-06	Rad3	radius of positive particles (m) (measurement)

3.3d0	Brugg	Bruggeman exponent for cathode
2.8d0	BruggE	Bruggeman exponent for separator
0.457d0	ep1	volume fraction of electrolyte in negative electrode
0.00d0	epp1	volume fraction of polymer in negative electrode
0.026d0	epf1	volume fraction of inert filler in negative electrode
0.37d0	ep2	volume fraction of electrolyte in separator
0.0d0	epp2	volume fraction of polymer in separator
0.305d0	ep3	volume fraction of electrolyte in positive electrode
0.20d0	epp3	volume fraction of polymer in positive electrode
0.2d0	epf3	volume fraction of inert filler in positive electrode
100.d0	sig1	conductivity of negative matrix (S/m) (ignored in Foil mode)
0.345d0	sig3	conductivity of positive matrix (S/m)
1.30d-4	rka1	rate constant for negative reaction (mol/m^2s)
6.29d-11	rka3	rate constant for positive
0.00d0	ranode	anode film resistance (ohm-m^2)
0.04d0	rcathde	cathode film resistance (ohm-m^2)
3862.00d0	cot1	coulombic capacity of negative material (mAh/g)
120.0d0	cot3	coulombic capacity of positive material (mAh/g)
1324.0d0	re	density of electrolyte (kg/m^3)
2260.0d0	rs1	density of negative insertion material (kg/m^3)
4140.0d0	rs3	density of positive insertion material (kg/m^3)
1400.d0	rf	density of inert filler (kg/m^3)
1780.d0	rpl	(not used here) density of polymer material (kg/m^3)
0.0d0	rc	density of inert separator material (kg/m^3)
8954.0d0	rcn	density of negative current collector (kg/m^3)
2707.0d0	rcp	density of positive current collector (kg/m^3)
0.0d0	htc	heat-transfer coefficient at ends of cell stack (W/m^2K)
0.0d0	dUdT	temperature coefficient of open-circuit potential (V/K)
2000.0d0	Cp	heat capacity of system (J/kg-K)
298.d0	Tam	ambient air temperature (K)
1	ncell	number of cells in a cell stack
2	lht	0 uses htc, 1 calcs htc, 2 isothermal
1	il1	1 for long print-out 0 for short print-out
4	il2	prints every il2 th node in long print-out
4	il3	prints every il3 th time step in long print-out
1	lflag	0 for electrolyte in separator only,1 for uniform
0	imp	0 for no impedance, 1 for impedance
1.0d-01	capp1	capacitance of negative material (F/m^2)
1.0d02	capp3	capacitance of positive material (F/m^2)
0	lpow	0 for no power peaks, 1 for power peaks
0	jsol	calculate solid profiles if 1 < jsol < nj
3	nneg	using MCMB to simulate lithium foil
11	nprop	$LiPF_6$ in EC:DMC liquid
11	npos	$LiAl_{0.2}Mn_{1.8}O_4F_{0.2}$ with OCP fitted to our material $LiAl_{0.14}Mn_{1.86}O_4$
1	lcurs	number of current changes
86.5d0	3.3d0	2

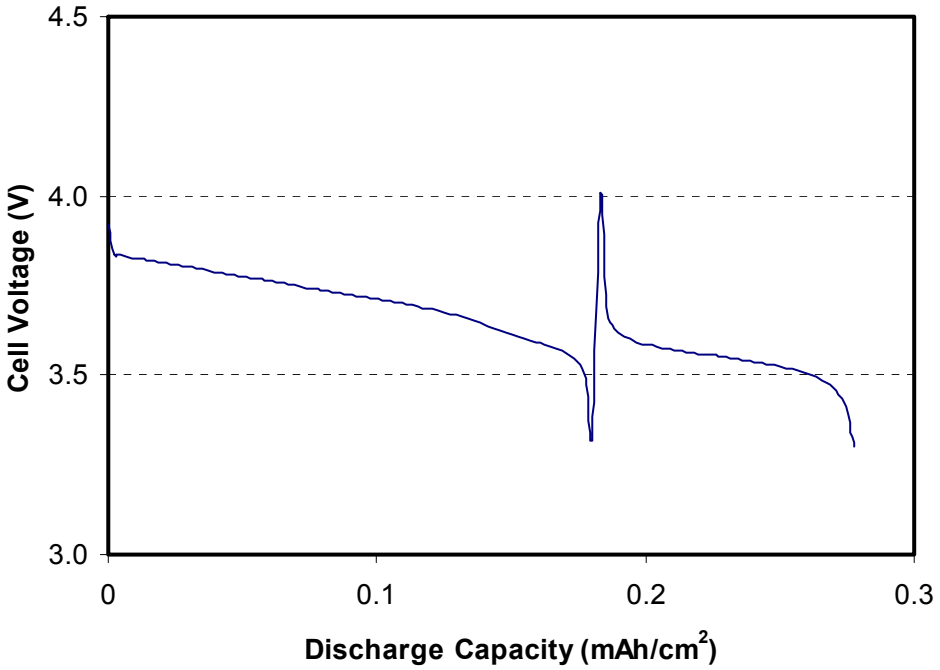

Figure B.1 Unrealistic voltage jump in the dual foil model using a lithium metal anode

APPENDIX C: VOLUME FRACTION ESTIMATION OF CATHODES

In this study, a method similar to the one in Mandal et al. (2001) was used to estimate the volume fraction of the components in the composite cathodes. In short, volume of component *i* is calculated by Eq. C.1, and then the volume fraction V_i is calculated by Eq. C.2.

$$V_i = \frac{m_i}{\rho_i} \tag{C.1}$$

$$\varepsilon_i = \frac{V_i}{\sum_i V_i} \tag{C.2}$$

Where V_i is volume of component *i*, m is mass, ρ is density, ε is volume fraction.

The density data is listed Table C.1. The data is quoted from Mandal et al. (2001) unless otherwise stated.

Table C.1 Densities of electrode materials

Material	Bulk Density (g/cm^3) *1	True Density (g/cm^3)	Component vol% *3	Pore Vol % *4
$LiAl_{0.14}Mn_{1.86}O_4$	1.03	4.28	24	76
PVDF	0.30	1.80	17	83
CB	0.096	1.4	7	93
SWNT	0.17	1.4 *2	12	88

Note:
*1: Measured values;
*2: Data from Carbolex Inc.;
*3: Component volume fraction is calculated by (bulk density)/(true density);
*4: Air volume fraction =1.0- component vol. fraction.

In this study, the volume of the composite electrode is calculated based on the measured data of film area and thickness. The volume of each component in an electrode can be easily

calculated using the mass and corresponding density data. Examples of calculation are listed in Table C.2.

A comparison of the volume fraction data with that in Lazarraga et al. (2003) is provided in Table C.3. Note that the estimated porosities in this study were significantly larger those in Lazarraga et al. (2003). This was explained as the result of the difference in the pressures: the cathode pellets in Lazarraga et al. (2003) were compressed at 170 MPa and the composite cathodes in this study were compressed at 20 inch-lb (which was estimated to be about 1 MPa). Therefore, it seems reasonable that the porosities in this study were about 50% larger than those in Lazarraga et al. (2003).

Table C.2 Examples of volume fraction calculation in uncompressed composite cathodes

	Mass fraction (%)			total volume	Estimated component volume (cm^3)			volume fraction (%)			
	PVDF	AM*	Carbon	(cm^3)	PVDF	AM	Carbon	PVDF	AM	Carbon	pore
12% CB	2.6	85.4	12	105.0	1.44	19.9	6.06	1.4	19.0	5.8	73.8
12% CNT	2.6	85.4	12	127.3	1.44	19.9	8.57	1.1	15.7	6.7	76.5

Note *: "AM" is short for active material.

Table C.3 Estimated volume fraction data compared with Lazarraga et al. (2003)

Label	PVDF		$LiMn_2O_4$		CB		Pore
	wt%	vol%	wt%	vol%	wt%	vol%	vol%
1 wt% CB*	9.5	13.3	89.4	53	1.1	1.4	32.8
7 wt% CB*	10	12.7	82.7	44.4	7.3	8.6	34.3
11 wt%	11	12.4	78.0	36.9	11	11.2	39.4
1wt%CB**	2.6	2.9	96.4	45.7	1.0	1.0	50.3
7wt%CB**	2.6	2.5	89.9	37.0	7.5	6.7	53.7
12wt%CB**	2.6	1.7	85.4	23.1	12	7.0	68.2

Note *: data for composite pellets compressed at 170 MPa in Lazarraga et al. (2003);
Note **: estimated data for CB-cathodes compressed at 20 in-lb in this study.